Correlating Structural and Interfacial Effects of Ceramic Solid Electrolytes with Cycling Stability of Li metal in Solid-State Batteries

by

María Regina García Méndez

A dissertation submitted in partial fulfillment
of the requirements for the degree of
Doctor of Philosophy
(Materials Science and Engineering)
in the University of Michigan
2020

Doctoral Committee:

Associate Professor Jeff S. Sakamoto, Chair
Assistant Professor Neil P. Dasgupta
Assistant Professor John Thomas Heron
Professor Katsuyo S. Thornton

Regina Garcia-Mendez

reginagm@umich.edu

ORCID iD: 0000-0002-0980-3673

Dedication

This dissertation is dedicated to my family; both my parents Aury and Arturo, and my brother Pablo, who have supported me unconditionally and believed in me without measure.

Acknowledgements

First and foremost, I would like to express my sincere gratitude and appreciation to professor Jeff Sakamoto, who has been more than just my research advisor, but my academic parent. He has nurtured my growth as a scientist since I joined his group as a master's student, by engaging with me in numerous discussions, challenging me to push myself, encouraging me to pursue my goals (academic and non-academic), and providing constant support. His excitement and passion for science along with a sense of caring about his students made me choose him in the first place, and I can say that I feel grateful that it worked out.

I would also like thank my committee members for providing helpful feedback and serving in my committee. In particular, professor Neil P. Dasgupta, whom I have interacted numerous times, and have learned a lot from as part of collaborations we have had over the years that resulted in two publications with his students; Dr. Eric Kazyak and Andrew Davis. I would like to thank professor Donald J. Siegel and his group members; Dr. Jeffrey G. Smith and Dr. Seungho Yu who were an integral part of two publications presented here.

I would also like to thank the people that were there for me; not only in the good and exciting times, but also in the hard ones. I could not have gone through it without your friendship and invaluable support. In particular, Arushi and Mike, who have been wonderful to me, I cannot express in words how lucky I feel to have you guys as part of my life. Also, Ge-Ah, Fatema, Linh, Estefanía, Maya and Adrian for being a source of constant support, advice and encouragement throughout my time here in Michigan. Last but not least, my friends from Guatemala that have not failed to walk with me in this journey, in particular, Cristina, Clara, Alicia and Vivian.

I would like to express my gratitude to Dr. Fuminori Mizuno, Tim Chambers and Bobby Kerns who have also been mentors to me regarding research, teaching and electron microscopy at the Michigan Center for Materials Characterization. Including valuable discussions from Timothy S. Arthur at Toyota Research Institute of North America.

Finally, I would like to acknowledge the financial support I have received over the years. First, Toyota Research Institute of North America for funding the work presented in Chapter 4, and partially Chapter 5. Additionally, the work in Chapter 5 was partially conducted at the Spallation Neutron Source at Oak Ridge National Laboratory (ORNL). Chapter 6 was financially supported by the U.S Department of Energy Advanced Battery Materials (BRM) program within the office of energy efficiency and renewable energy (EERE), Grant no. DE-EE0991-1663, including support from the institutional program of the Korea Institute of Science and Technology, project No. 2E30202.

Table of Contents

List of Tables

List of Figures

Abstract

The significant increase in anthropogenic CO_2 emissions has emphasized the need to transition to a more sustainable energy future. Transportation-related emissions comprise the highest contribution of greenhouse gases, thus creating the great need for higher-efficiency, zero-emissions electric vehicles (EVs). However, to meet energy/power density demands, advanced batteries superior to Li-ion are required. Li metal-solid-state batteries (LMSSBs) have the potential to enable Li metal anodes, but also improve safety by replacing the flammable liquid electrolyte with a non-flammable solid. Li metal anodes are of particular interest because they could enable ~50% higher energy densities compared to conventional Li-ion batteries. Despite the discovery of a variety of promising solid-state electrolytes (SSEs), stable cycling of Li metal remains a challenge. Even though it has been observed that Li metal penetrates polymer, glass, single crystal and polycrystalline inorganic solid electrolytes upon charging, the phenomenon is not thoroughly understood. Currently, the metric used to quantify the resistance of a SSE to Li metal propagation, or the current density at which a Li filament propagates across a SSE is known as the critical current density (CCD). The magnitude of the CCD of a SSE is important because it determines the maximum current density at which a LMSSB can be charged without Li metal propagation that results in short-circuit.

This thesis aims to gain a better understanding of the role that structural and interfacial effects play in elucidating the poorly understood Li penetration phenomenon. Two of the most promising inorganic solid electrolyte systems were used as platforms; oxide-based garnet

$Li_{6.25}Al_{0.25}La_3Zr_2O_{12}$ (LLZO) as a model system for crystalline materials and sulfide-based $75Li_2S$-$25P_2S_5$ mol% (LPS) as a model system for glass-ceramic and amorphous materials.

First, LPS was used to gain a deeper understanding of the interplay between microstructure-processing and electrochemical behavior when paired with a Li metal electrode. The effect of pressure and temperature on structural changes during densification were studied. Consequently, the differences observed in electrochemical performance were correlated to their respective atomic and micro structures. It was demonstrated that the CCD of LPS can be increased by controlling the crystalline structure that precipitates from the mother glass, not only enhancing its ionic transport, but also by improving the particle-particle adhesion during processing. In addition, a dense microstructure with low porosity (< a few percent) is desirable for higher rate capabilities. Thus, higher pressures during densification that can result in dense (~98% relative density) microstructures motivated the subsequent study on LPS. To achieve a dense glassy microstructure, the role that pressure has on densification at the glass transition temperature was investigated. Moreover, correlations between macro and atomic structure with elastic properties and ionic transport was pursued. A five-fold increase in ionic conductivity and a two-fold increase in elastic constants were measured compared to conventional room temperature molding conditions. We believe these results were attained due to favorable coordination environments for Li ion transport and molecular rearrangements. The latter was elucidated via neutron diffraction high-resolution pair distribution functions and *ab initio* molecular dynamics calculations. Lastly, the DC electrochemical stability of the optimized microstructure was characterized achieving an increase in CCD compared to the conventional cold-pressed sample, but highlighting the importance of external variables such as pressure and/or temperature as practical challenges that sulfide-based and other SSEs must overcome to improve cycling of Li metal.

Finally, a mechanistic understanding of the coupled interfacial and quantum mechanical effects have on the Li-LLZO interface stability at low potentials was studied. Integration of a Li reference electrode in a solid-state cell and precise experimental control allowed to confirm empirically, for the first time, that LLZO is stable at Li cathodic potentials below 0 V vs Li/Li$^+$. A new atomistic perspective by which Li penetrates LLZO SSE at the interface is proposed and validated via first-principles theoretical calculations.

The findings in this work provide fundamental understanding towards overcoming the challenge of Li penetration in SSEs, which can translate into higher-rate-capability LMSSBs for high-energy demand applications.

CHAPTER 1 Introduction

1.1 Motivation

Global energy reserves are depleting at an alarming rate, creating worldwide economic, environmental, industrial, and societal concern.[1] In 2018, CO_2 emissions increased in all U.S. end-use sectors, where transportation-related CO_2 emissions were the highest contributor among all sectors, followed by the industrial sector.

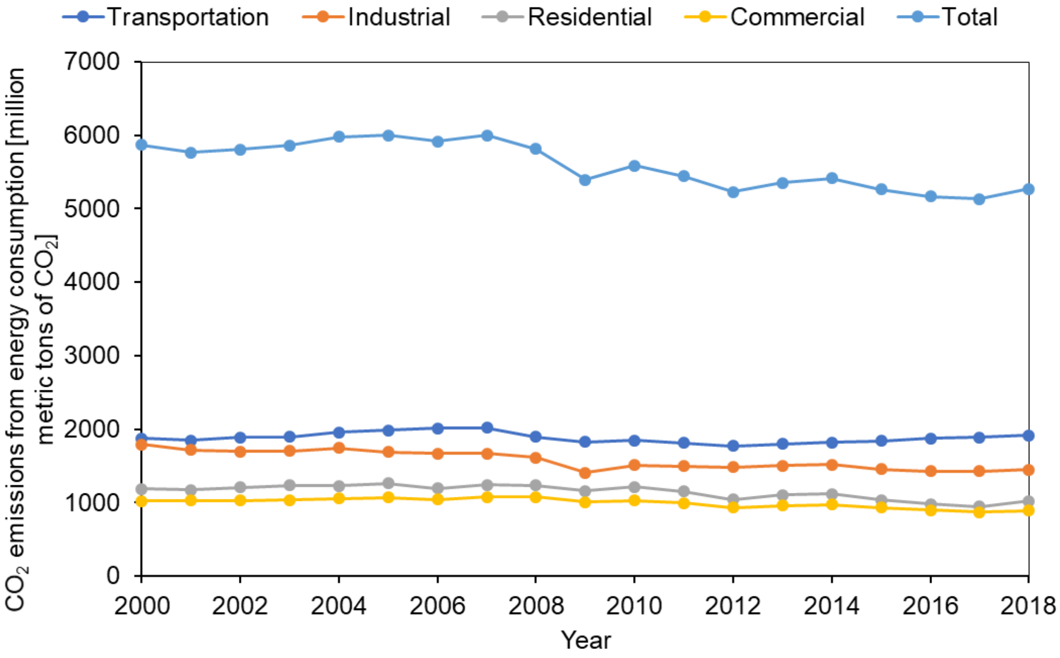

Figure 1.1 *Carbon dioxide emissions based on end-use sector* [2]

While the efficiency and emissions of new conventional vehicles have improved significantly in recent years, the U.S. passenger vehicle fleet still accounts for more than 70% of U.S. oil demand[3] as seen in Figure 1.2. Consequently, electric vehicles (EVs) are considered as one solution for the challenge of providing affordable, clean, secure transportation. Unlike conventional vehicles, which are powered primarily by petroleum-based fuels, EVs are powered at least in part by electricity that is generated from domestic, diverse, and secure energy sources. Even though electric vehicle deployment has been growing rapidly over the past ten years, passing 5 million in 2018,[4] an increase of 63% from the previous year, widespread adoption has not yet been achieved.

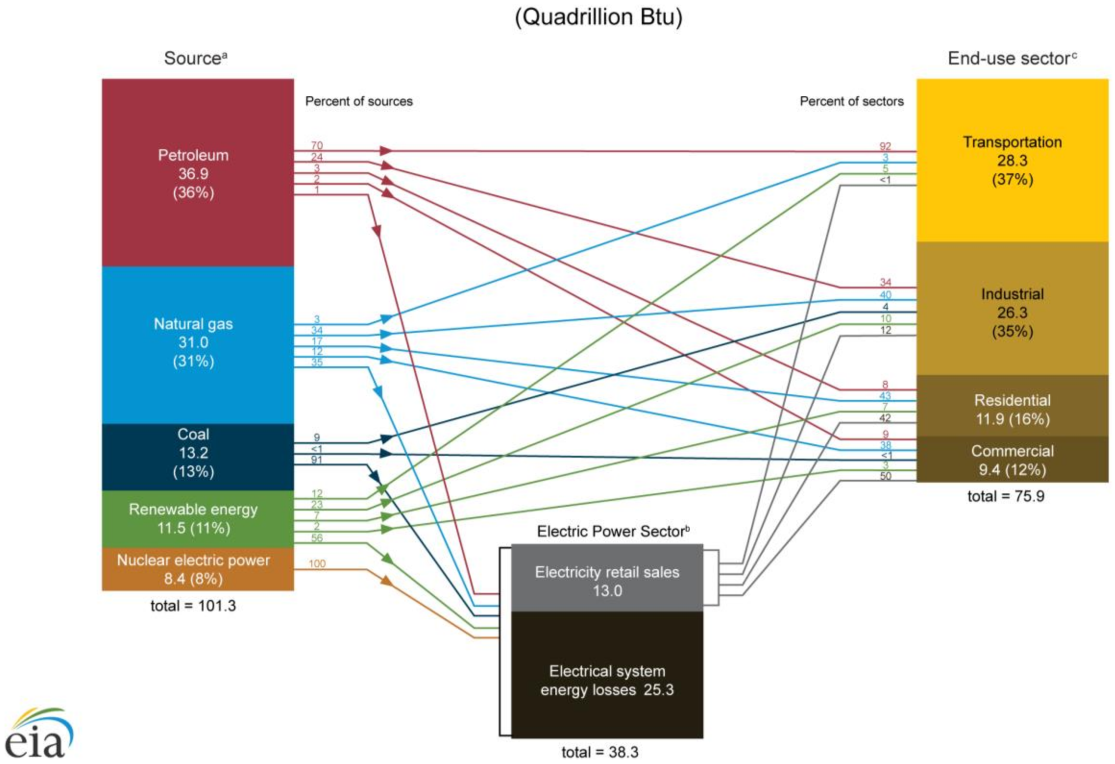

Figure 1.2 *U.S. Energy consumption by source and sector in 2018*[3]

The three main factors influencing the lack of consumer adoption of electric vehicles include: cost, driving range, and an under-developed charging infrastructure.[5] Overcoming the cost of EVs will be achieved through increased production volume as well as in advancements in technology. However, cost and production volume are directly correlated to consumer awareness and having a charging infrastructure that matches consumer demand. [5] Driving range is also of extreme importance in the widespread adoption of electric vehicles. Mass market consumers will require vehicles that offer the same range as an internal combustion engine powertrain. Thus, in order to attain comparable driving ranges (~300 miles), advanced batteries are needed that can fulfill the energy requirements set by the USABC (United States Advanced Battery Consortium LLC); 235 $\mathrm{Wh \cdot kg^{-1}}$, 500 $\mathrm{Wh \cdot L^{-1}}$ at the system level.[6]

Li metal-solid-state batteries (LMSSBs) have been proposed to enable high capacity anodes that translates into ~50% higher energy densities than conventional Li-ion batteries by the replacement of the conventional graphite anode with Li metal.[7,8] Additionally, LMSSBs can improve safety with the replacement of an inherently flammable liquid electrolyte with a solid that is thermally stable at high temperatures. Despite the accelerated discovery of a variety of promising SSEs with high ionic conductivity between 10^{-4} and 10^{-2} $\mathrm{S \cdot cm^{-1}}$ at room temperature, [9–11], and achieving low Li-SSE interface resistances ($\leq 10\ \Omega \cdot \mathrm{cm}^2$),[12] stable cycling of Li metal at relevant charging rates (C/3)[6] still remains a challenge. An ohmic response or stable Li cycling at relevant charging rates ($\geq 3\ \mathrm{mA \cdot cm^{-2}}$) remains elusive. Upon galvanostatic testing, three distinctive potential responses have been correlated to the transition from stable to unstable cycling in SSEs. First, at low current densities ($\leq 0.1\ \mathrm{mA \cdot cm^{-2}}$), an ohmic behavior or linear potential response is interpreted as stable electrodeposition/dissolution of Li. Next, at intermediate current densities ($\geq 0.5\ \mathrm{mA \cdot cm^{-2}}$), deviation from Ohm's law is observed, which corresponds to unstable cycling in which nucleation/initiation of Li penetration occurs at the Li-SSE interface. Finally, at high current densities ($\geq 1.0\ \mathrm{mA \cdot cm^{-2}}$), a drop in polarization is observed near 0 V vs $\mathrm{Li/Li^+}$, interpreted as Li propagation throughout the thickness of the electrolyte causing a short-circuit of the cell. The current density at which negligible potential response is obtained coupled with inductive behavior from alternate current (AC) measurements is the CCD of a SSE. In other words, CCD is the maximum tolerable current density a SSE can withstand without short-circuit. This value is important given that it determines the rate capability of a LMSSB. Even though Li metal penetration has been observed in a myriad of SSEs including polymers, glasses, single crystals and polycrystalline inorganic solid electrolytes, [13–17] the origin of the phenomenon is not thoroughly understood. Hence, this thesis focuses on the last two distinctive stages observed during CCD measurements in two of the most promising inorganic solid electrolytes; $Li_{6.25}Al_{0.25}La_3Zr_2O_{12}$ (LLZO) and $75Li_2S$-$25P_2S_5$ mol% (LPS). The initiation/nucleation stage where Li metal penetrates SSEs has not been studied given that chemical stability against Li metal is not inherent to most systems making it difficult to isolate and analyze such phenomenon in detail. Herein, oxide-based LLZO was used as a model system, as its chemical stability against Li allows the analysis of the Li-LLZO interfacial stability upon charging/plating. Toward this goal, a reference electrode was incorporated into a solid-state cell that allowed to control the potential of the Li-LLZO interface. The onset at which initiation/nucleation of Li penetration occurs is identified and described using a combination of direct current (DC) and AC measurements. Finally, macroscopic Li propagation is identified and described by the electrochemical signatures observed via DC and AC measurements along with optical microscopy characterization. The experimental results and their corresponding interpretation are validated via first-principles calculations. Lastly, structural effects on the low potential stability of the Li-LLZO interface are discussed.

Several recent studies have suggested that pre-existing microstructural defects such as pores and grain/particle boundaries can act as stress concentrators at the Li-SSE interface upon plating.[15–18] Also, it has been suggested that Li propagation can be driven by local electric-field concentrators at the edges of the electrodes.[17] This current focusing leads to preferential Li deposition which results in enhanced mechanical stresses at these locations resulting in mechanical failure or fracture of the SSE. To understand the coupling between microstructural defects and Li penetration at a macroscopic level, sulfide-based LPS SSE was selected as a model system. Given that its structural evolution with temperature and ionic transport properties is well documented, processing conditions such as temperature and pressure were changed to attain glassy (dense amorphous), amorphous and glass-ceramic microstructures. More importantly, processing was used as a means to minimize critical defect densities in LPS. Furthermore, the resistance to Li macroscopic propagation of each microstructure is characterized as a function of current density. Insight into the coupling between porosity, adhesion between particles or particle/grain boundaries and Li penetration was gained.

In summary, this thesis aims to gain a better understanding of the role structural and interfacial effects have in Li penetration in two of the most promising inorganic SSEs; LPS and LLZO, respectively. The hypotheses proposed and approaches taken to validate them are briefly described in the following section for each material. In addition, advantages and challenges associated with each solid electrolyte will be described in further detail in chapter 2.

1.2 Goals and outline

With the primary goal of providing guidelines for the design of bulk SSEs/interfaces to enable LMSSBs, this thesis investigates the role structural and interfacial effects have on Li penetration on LPS and LLZO SSEs, respectively. More specifically, LPS will be used as a model system to gain a deeper understanding on the interplay between microstructure-processing and electrochemical behavior against Li metal, and LLZO will be used to propose an atomistic model to explain the onset of Li metal penetration at the Li-LLZO interface. A brief outline of this thesis is given below:

Chapter 2 will present an overview of LLZO and LPS to include the challenges identified as the main roadblocks for each to achieve stable cycling of Li. Subsequently, an overview of basic concepts in ceramics processing is presented upon which strategies were constructed to control the LPS microstructure in Chapters 4 and 5.

Chapter 3 describes the methodology used for synthesis and processing of both SSEs, including the most relevant electrochemical characterization techniques/tools used throughout this thesis to investigate changes in ionic transport and decouple transitions between stable and unstable Li cycling.

The work presented in Chapter 4 pursues to validate the following hypothesis: *processing conditions affect microstructural defects in LPS that play a role in controlling Li penetration.* Validation of the hypothesis was pursued by changing the processing temperature to achieve different microstructural ordering; amorphous and glass-ceramics with different crystalline phases. The resistance to Li penetration was evaluated as a function of current density to determine the CCD of each microstructure. It was determined that the hot-pressed glass-ceramic LPS doubled the CCD that an annealed sample could withstand by the presence of high conductivity phases along with improved adhesion between particles. ~~.~~Challenges associated with achieving almost theoretical densities are also discussed.

The work presented in Chapter 5 addresses the lack of full densification of LPS SSE in Chapter 4 by coupling a custom-designed hot-pressing apparatus that advanced the powder compaction capabilities to enable higher molding pressures at the glass transition temperature. The hypothesis proposed in this Chapter is that *simultaneous application of pressure at the glass transition temperature will reduce LPS elastic modulus, thereby increasing compliance to facilitate densification.* Optimization of the densification conditions allowed an unprecedented reduction in porosity and particle boundaries while preserving the amorphous structure. A five-fold increase in ionic conductivity and a two-fold increase in elastic moduli were measured compared to conventional room temperature molding conditions. In addition, , the DC electrochemical stability of the optimized microstructure was characterized yielding an increase in CCD compared to the conventional room temperature molding conditions. Nevertheless, emphasis on the importance of external variables such as stack pressure and/or temperature for achieving stable Li cycling is also discussed.

The work in Chapter 6 pursues to validate the following hypothesis: *polarization of the Li-LLZO interface can shift the Fermi level of the solid electrolyte into the conduction band minimum allowing free electrons to recombine with lithium ions resulting in Li metal precipitation/nucleation at the interface*. First, the low voltage stability of the Li-LLZO interface was studied by integration of a Li reference electrode in a custom-designed solid-state cell that isolated and measured the current response of the interface at an below zero volts. An initiation/nucleation mechanism by which Li penetrates LLZO at the atomic level is proposed based on the Li-LLZO interface behavior ≤ 0 V validated by first-principles theoretical calculations. Superimposition of Electrochemical Impedance Spectroscopy (EIS) measurements onto the DC measurements enabled the *in*-operando evolution of transport phenomena. The electrochemical traces collected in DC and AC measurements allowed to distinguish between the initiation/nucleation and propagation stages. Furthermore, structural and interfacial effects on the low potential stability of the Li-LLZO interface are discussed. The proposed initiation/nucleation mechanism can not only provide insight into the fundamental nature of the variables that control the stability of the alkali metal-SSE interfaces, but also serve as a guideline towards higher charge rates in LMSSB applications.

Chapter 7 concludes by summarizing the outcomes and discusses questions that remain that, if answered, could generate a broader understanding of how to achieve stable cycling of Li metal.

The studies described in this thesis have been, or are currently in review, in the following peer-review publications:

1. Garcia-Mendez, R., Mizuno, F., Zhang, R., Arthur, T. S., & Sakamoto, J. (2017). Effect of processing conditions of 75Li2S-25P2S5 solid electrolyte on its DC electrochemical behavior. *Electrochimica Acta*, *237*, 144-151. DOI: 10.1016/j.electacta.2017.03.200
2. Garcia-Mendez, R., Smith, J. G., Neuefeind, J. C., Siegel, D. J. and Sakamoto, J. Correlating macro and atomic structure with elastic properties and ionic transport of glassy Li_2S-P_2S_5 (LPS) solid electrolyte for solid-state Li metal batteries. *Advanced Energy Materials*, 2020. DOI: 10.1002/aenm.202000335
3. Garcia-Mendez, R., Yu, S., Siegel, D. J. and Sakamoto, J. Quantum Mechanical and Electrochemical Stability of the solid-state $Li_{6.25}Al_{0.25}La_3Zr_2O_{12}$ (LLZO)-Li interface [*In preparation*]

The contributions of each co-author in the aforementioned publications, and consequently in the work presented in this thesis, are briefly summarized below. Chapter 4 was adapted from Garcia-Mendez, R. et al. 2017.[19] Regina Garcia-Mendez performed all of the synthesis and processing of the LPS solid electrolyte samples. The materials and electrochemical characterization were conducted by Regina Garcia-Mendez except X-Ray Diffraction measurements and Raman mapping, which were acquired by Ruigang Zhang and Fuminori Mizuno, respectively. Fuminori Mizuno and Jeff Sakamoto provided guidance and support.

Chapter 5 was adapted from Garcia-Mendez, R. et al. 2020.[20] Regina Garcia-Mendez developed a more reproducible synthesis method for LPS solid electrolyte compared to the synthesis method used in Chapter 4. Additionally, designed and built a custom-made hot-press setup to precisely control heating/cooling rates along with holding temperature and pressure during densification. All materials and electrochemical characterization were performed by Regina Garcia-Mendez except for the Raman spectra collected by Timothy S. Arthur. Jeffrey G. Smith and Donald J. Siegel designed and carried out the computational modeling. Regina Garcia-Mendez wrote the proposal and prepared all the samples for neutron diffraction experiments. Also, R. G-M. performed the neutron diffraction high-resolution pair distribution function measurements at beamline 1B at the Spallation Neutron Source under the guidance of the beamline scientist Dr. Joerg Neuefeind. Jeffrey G. Smith attended the neutron experiments. Donald J. Siegel and Jeff Sakamoto provided insights, guidance and support.

In Chapter 6, Regina Garcia-Mendez designed, optimized and validated the geometrical requirements for the three-electrode solid-state cell used for data acquisition. Also, R. G-M. carried out all the synthesis, processing and materials/electrochemical characterization in the study. Dr. Seungho Yu and Donald J. Siegel designed and carried out the theoretical calculations regarding electronic states in LLZO. Donald J. Siegel and Jeff Sakamoto provided guidance and support.

CHAPTER 2 Background

2.1 Electrochemical cells

An electrochemical cell or battery is a device that stores electrical energy in the form of chemical energy, and converts that energy into electricity. The main components of a battery are the positively charged and negatively charged electrodes (cathode and anode, respectively), separated by an electrolyte, which could be a liquid or a solid. The electrolyte conducts the ionic current of the chemical reaction between the anode and the cathode. Simultaneously, an electronic current flows through an external circuit to do work (Figure 2.1).

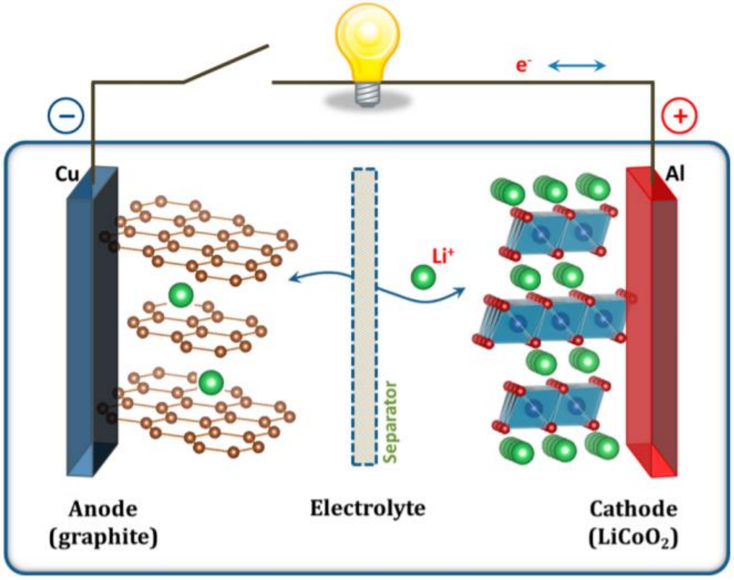

Figure 2.1 *Schematic diagram of a Li-ion battery. Reprinted (adapted) with permission from Goodenough J. B and Park, K-Y. Copyright 2013 American Chemical Society*[21]

Depending on the cell design and chemistry, batteries are classified in the following two groups:

1. *Primary cells* are non-rechargeable, in which the electrochemical reaction is irreversible. They contain only a fixed amount of the reacting compounds and are discharged only once. [22]
2. *Secondary cells* can be repeatedly charged and discharged. Only reversible electrochemical reactions offer such a possibility. After the cell is discharged, externally applied electrical energy forces a reversal of the electrochemical process; as a consequence, the reactants are returned to their original form and the stored electrochemical energy can be used again. The process should be reversible hundreds or even thousands of times.[22]

Secondary Li batteries involve a reversible insertion/extraction of Li ions (guest species) into/from a host matrix (electrode material) during the discharge/charge process. The Li insertion/extraction process involves the flow of ions through the electrolyte, which is accompanied by a reduction/oxidation (redox) reaction of the host matrix. To balance the flow of ions, a parallel flow of electrons travels simultaneously through an external circuit. [23] To illustrate the principle of the charge and discharge processes, a Li-ion battery is used as an example of a secondary cell. Typically, a transition metal oxide with a layered structure such as $LiCoO_2$ is used as the cathode, and graphite is used as the anode. During the charging process, Li ions deintercalate from the positive electrode while releasing an electron. Simultaneously, oxidation of the cathode metal cation occurs, e.g. Co^{3+} is oxidized into Co^{4+}in LCO. Upon discharge, intercalation/insertion of Li^+, Co^{4+} is reduced to Co^{3+}, gaining one electron. On the anode side, the intercalation/insertion of Li^+ into graphite, one electron will be obtained from the lattice at the same time to turn into atomic state Li. During the discharge process, Li loses one electron to become a Li ion and deintercalates/extracts from the graphene layers. Since Li moves back and forth between the positive and negative electrodes, it is called a rocking chair battery. Sony Corporation was the first to call it a Li-ion battery, which the name generally used. [24]

The chemical driving force across the cell is due to the difference in the chemical potentials of its two electrodes. It can be expressed as the *standard Gibbs free energy change per mol of reaction*, $\Delta G_r°$. This is determined by the difference between the standard Gibbs free energies of formation of products and reactants in the virtual chemical reaction that would occur if the electrically neutral materials in the two electrodes were to react chemically. It makes no difference that the reaction actually happens by the transport of ions and electrons across the electrochemical cell from one electrode to the other. [25]

The electrostatic energy per mol of an electrically charged species is $-zFE$, where E is the voltage between the electrodes, and z the charge number of the mobile ionic species involved in the virtual reaction. The charge number is the number of elementary charges that they transport. F is the Faraday constant. An equivalent is Avogadro's number (one mol) of electronic charges. The balance between the chemical and electrical forces upon the ions under open circuit conditions can hence be simply expressed as an energy balance:

$$\Delta G_r^{\circ} = -zFE \tag{2.1}$$

The value of $\Delta G_r°$ is in Joules per mol of reaction; 1 Joule is the product of one Coulomb and one Volt. [25]

The basic driving force in an electrochemical cell is thus a chemical reaction of neutral species forming an electrically neutral product. This is why standard chemical thermodynamic data can be used to understand the equilibrium (no current, or open circuit) potentials and voltages in electrochemical cells. [25]

2.2 Solid-State Electrochemistry

The field of solid-state electrochemistry is not new. It has its origins, as does so much of electrochemistry, with Michael Faraday who discovered that PbF_2 and Ag_2S were good conductors back in 1838. He therefore established both the first solid electrolyte and the first intercalation electrode. Faraday appreciated the benefits of unifying science rather than compartmentalizing it. Regrettably, in the years after Faraday's pioneering work on electrochemistry was largely lost. The subjects of solid and liquid electrochemistry grew apart and developed separately until recent times. The dominance of the latter was probably due to the ease with which a wide range of liquid electrolytes could be prepared and purified. Solid-state electrochemistry developed steadily up to the late 1960s, and may be divided into two broad topics: [26]

- Solid electrolytes (SEs), which conduct electricity by the motion of ions, and exhibit negligible electronic transport. Included in this group are crystalline and amorphous inorganic solids as well as ionically conducting polymers.
- Intercalation electrodes, which conduct both ions and electrons. Also, with numerous examples based mainly on inorganic solids and polymers.
- Conducting polymers were, in that period, unknown; the subject dealt exclusively with inorganic solids and glasses. [26] The latter half of the 1960s and the early years of the 1970s saw an explosion of interest in solid-state electrochemistry with the sodium ß-Al_2O_3 with the oil crisis. In the 1990s environmental concerns have, to some extent, replaced the oil crisis as a technological driving force in the field or solid-state ionics, both from the point of view of batteries, adoption of electric vehicles and compact low power batteries for portable electronic equipment. Furthermore, solid and liquid electrochemistry are, after 150 years, growing together. Mixed electronic and ionic conducting and electronically

conducting polymer electrodes provide the most obvious link. More importantly, solid-state systems can expand fundamental aspects of electrochemistry, such as the electrochemical evolution of electrode materials and interfaces along with mechanical degradation due to the all-solid nature of these systems. [27]

2.2.1 Solid-State Electrolytes (SSEs)

During the past 200 years, most battery research has focused on systems with liquid electrolytes.[28] Although liquid electrolytes offer the benefits of high conductivity and excellent wetting of electrode surfaces, they often suffer from inadequate electrochemical and thermal stabilities, low ion selectivity and poor safety.[29] Replacement of liquid electrolytes with a solid electrolyte have the potential to overcome the challenges of liquid electrolytes, but also offer possibilities for developing new battery chemistries, allowing consideration of liquid and gaseous reactants that could result in high power and energy densities.[21,30] In addition to reducing the need of thermal management, and potentially enabling longer cycle life. [28]

An LMSSB would, in principle, use an inorganic solid or a polymer electrolyte that would ideally comply with all the following criteria for practical application: [21,29,31]

1. High ionic conductivity: 3×10^{-3} to 2×10^{-2} $S \cdot cm^{-1}$ at room temperature to reduce the resistance polarization effects in a solid-state battery.
2. Transference number for ionic conduction should be as close as possible to unity (0.99999). Any electronic contribution to the electrical conductivity of the electrolyte leads to self-discharge. [32]
3. Thermodynamically stable and should perform well in a wide temperature range (-30 to +52 °C)[6]

4. Chemically and electrochemically stable against cathode and anode with and without bias. In other words, the absolute position of the band edges of the SSE (valence band maximum and conduction band minimum) would ideally lie ≥ 1 V more positive (lower energy) than the electrochemical potential of the cathode and > 1 V more negative (higher energy) than the anode electrochemical potential, respectively. [33,34]
5. Low ionic interfacial resistance (≤ 10 Ω·cm^2) against electrodes[12]
6. Ability to suppress alkali metal penetration upon charging
7. Easily fabricated into a mechanically robust, flexible thin membrane ($< 25 \pm 1$ µm)[6]
8. Low cost ($100 and $125 kWh at the cell and system level, respectively)[6]
9. Environmentally benign

Considering the above-mentioned requirements for a SSE, earlier work focused on the development of SSEs that satisfied criteria one through three. Although, several ionic conductors have met such requirements,[9,10,35–37] the stabilization of interfaces between LMSSB components (criteria 4 – 6) still remain a main roadblock towards their commercialization. Some improvement on reducing interfacial resistances has been achieved in some systems by surface treatments, co-sintering or interfacial layers reaching values between 2 – 90 Ω·cm^2.[12,38–40] However, the ability to suppress alkali metal penetration upon charging has not been fully understood and remains the focus of current studies including this thesis given its importance towards practical feasibility. As this work will center on LLZO and LPS SSEs and their resistance to Li metal penetration, only these two classes of materials will be discussed in more detail in the subsequent sections.

2.2.1.1 Li Ion Conductors

The main inorganic solid electrolytes that are being explored for solid-state batteries are perovskite-type, LI/NASICON-type, oxide-based garnet-type and sulfide-based materials.

2.2.1.1.1 Oxide-based Solid Electrolytes

Oxide-based SEs include garnets, perovskites, antiperovskites and NASICONs. They exhibit higher oxidation stability and improved chemical stability with oxide cathodes compared with sulfide SSEs. [34,41,42] However, the room-temperature bulk ionic conductivity of oxide SSEs is generally lower than that of sulfides, and their large grain-boundary resistance further restricts the total ionic conductivity.[37,43–46] Because of the mechanical rigidity of oxides, high-temperature sintering is usually required to a produce dense SSE, which translates in higher costs. [36,45,47,48]

2.4.1.1 Garnet Solid Electrolytes

Among oxides, garnet-type materials have the general formula $A_3B_2Si_3O_{12}$, in which the A and B cations have eight-fold and six-fold coordination, respectively. Since it was first discovered in 1969 ($Li_3M_2Ln_3O_{12}$, M = W or Te),[49] a series of garnet-type materials has been developed, the representative systems being $Li_5La_3M_2O_{12}$ (M = Nb or Ta), $Li_{5.5}La_3M_{1.75}B_{0.25}O_{12}$ (M = Nb or Ta; B = In or Zr), $Li_7La_3Zr_2O_{12}$ (LLZO) and $Li_{7.06}M_3Y_{0.06}Zr_{1.94}O_{12}$ (M = La, Nb or Ta).[9,36,50–52]

LLZO garnet is a promising electrolyte that exists in a tetragonal and cubic polymorph, where the cubic phase exhibits ~2 orders of magnitude higher Li-ion conduction. Thus, the stabilized *cubic*-LLZO polymorph is preferred. It has been reported that a critical Li vacancy concentration (0.4 – 0.5 atoms per formula unit) is required to stabilize the cubic polymorph of LLZO via density functional and molecular dynamics calculations.[53] In agreement, several experimental studies have stabilized the cubic phase through the substitution of super valent cations such as Al^{3+},[54] Ga^{3+} [55] on the Li^+ site and/or Nb^{5+},[52] Ta^{5+} [56] on the Zr^{4+} site. This results in the formation of Li vacancies to balance extra positive charge of the super valent cation, exhibiting ionic conductivities at room-temperature of 10^{-4} – 10^{-3} S·cm^{-1}. [9,51]

Aside from an adequate ionic conductivity at room temperature (10^{-4} S·cm^{-1} to 1 mS·cm^{-1}),[54] garnet LLZO meets several of the criteria listed for an ideal SSE, e.g. low interfacial resistance against metallic Li (2 Ω·cm^2) without the need for interlayer coatings [12], wide electrochemical window (0.05 to 5 V) [7] and chemically stable against metallic Li [34]. However, Li metal penetration is still observed under a plating current density > 1 mA·cm^2,[57] and processing cost for large-scale production is a concern.

2.2.1.1.2 Sulfide-based Solid Electrolytes

Sulfides, especially thio-phosphates based on the Li-P-S system, have emerged as leading SSE candidates due to their high ionic conductivities. S^{2-} with a larger ionic radii and more polarizable character than O^{2-} improve the mobility of the conducting species evidenced by a reduction of the activation energy for ionic conduction by replacing an oxide with a sulfide anion matrix.[58,59] In addition, their solution processability and ability to deform under cold pressing provide sulfides with an advantage for cell manufacturing compared with oxides. [60] Examples of sulfide SSEs with high ionic conductivity include $Li_7P_3S_{11}$ glass-ceramic (17 mS·cm^{-1})[35] , $Li_{10}GeP_2S_{12}$ (12 mS·cm^{-1}),[10] the thio-LISICON conductor $Li_{3.25}Ge_{0.25}P_{0.75}S_4$ (2.2 mS·cm^{-1}),[59] and amorphous Li_3PS_4 (0.2 mS·cm^{-1}).[19]

Even though sulfide-based materials have exhibited high conductivity, a compliant nature that could accommodate cyclic expansions of an adjacent electrode, low interfacial ionic resistance against metallic Li and ease of consolidation (low temperature densification) compared to oxides, low oxidation stability and sensitivity to moisture are considered as their main drawbacks.[31]

2.2.1.1.2.1 LPS

Glassy solid electrolytes in the system Li_2S-P_2S_5 (LPS) have shown Li ion conductivities of 10^{-4} S cm^{-1} at room temperature.[11] However, precipitation of superionic metastable crystals by careful heat treatment of the pristine glasses enhances the ionic conductivity.[61–63] The conductivities of the LPS glasses increase with an increase in the Li_2S content as a Li source, and attains a maximum at the composition of 80 mol % Li_2S with 2.1 x10^{-4} S cm^{-1}. Further increase in the Li_2S content leads to a decrease in conductivity. On the other hand, the conductivities of the glass-ceramics depend on the compositions due to precipitation of different crystalline phases from the pristine glasses.[11] The $70Li_2S$-$30P_2S_5$ (mol %) or LPS 70-30 glass-ceramic exhibits the highest conductivity of 3.2 x 10^{-3} S cm^{-1} at room temperature and the lowest activation energy of 12 kJ mol^{-1} for conduction.[11] Nevertheless, this composition is not the most chemically stable in air. Muramatsu *et al.* showed that the composition of LPS 75-25 (glass and glass-ceramic) generated the least amount of H_2S after exposure to air for one minute without a significant change after longer storage. Additionally, the sulfide electrolyte at this composition undergoes little structural change in air, which was confirmed by Raman spectroscopy before and after one day of exposure to air.[64]

Highly conductive crystalline thio-LISICON analogs are formed by the crystallization of the mechanically milled LPS glasses. The names were coined due to the similarity between crystal structures. Nonetheless, the glass-ceramics obtained by heating the LPS glasses have no germanium as the thio-LISICON. Analysis of the thio-LISICON ($Li_{4-x}Ge_{1-x}P_xS_4$) diffraction patterns indicated that the system is divided into three composition regions depending on the appearance of superlattice reflections. The patterns in region I ($0 < x \leq 0.6$) were indexed assuming a monoclinic superlattice cell of a × 3b × 2c. However, the superlattice reflections in region II (0.6

$< x < 0.8$) were indexed by a different monoclinic cell with a × 3b × 3c, and region III ($0.8 \leq x < 1.0$) showed a monoclinic a × 3b × 2c cell.[59] A presumable explanation for the similarities on X-Ray Diffraction (XRD) patterns is to assume that the Li-richer $Li_{3+5y}P_{1-y}S_4$ phases with a lack of phosphorus are formed in the glass ceramics. Thus, the crystal structures of $Li_{3.25}P_{0.95}S_4$ and $Li_{3.2}P_{0.96}S_4$ would be similar to those of thio-LISICON II ($Li_{3.25}Ge_{0.25}P_{0.75}S_4$) and thio-LISICON III ($Li_{3.2}Ge_{0.2}P_{0.8}S_4$), respectively.[61]

In the case of the LPS 75-25 glass, the thio-LISICON III analog is formed as the first precipitated crystal and remains up to 300ºC. The crystals of Li_3PS_4 and $Li_4P_2S_6$ are finally present at 550 ºC[4]. Hayashi *et al.* reported that the thio-LISICON II analog with higher Li content and higher ionic conductivity than the thio-LISICON III analog was not formed in the LPS 75-25 glass, but formed in the Li-richer LPS 80-20 glass.[61] The thio-LISICON II and III analogs have not been reported as thermodynamically stable crystals in the LPS system. Hence, these phases probably precipitated as a metastable phase from the mechanically milled LPS glasses, and they are changed to a stable crystal such as Li_3PS_4 with an increase in temperature[4]. Crystals such as Li_3PS_4 and $Li_4P_2S_6$ have been reported to show a low conductivity below of 10^{-7} S cm^{-1} at room temperature.[65] However, amorphous and glass-ceramic LPS 75-25 have exhibited an adequate ionic conductivity for LMSSBs applications, on the 10^{-4} to 10^{-3} S cm^{-1} range. [11]

2.3 Ceramic Powder Compaction

Powder densification can be achieved through one of three methods: i) powder compaction by application of pressure without heat resulting in a green body, ii) powder compaction followed by sintering (heating to form chemical bonds between particles without pressure), or iii) simultaneously press and heat a green body, or hot-pressing.

A schematic of powder compaction is shown in *Figure 2.2*. It provides a basis for defining the stages of compaction. At the beginning of a compaction cycle, the powder has a density approximately equal to the green density. Voids exist between the particles, and the highest obtainable density is only the tap density. As pressure is applied, the first response is rearrangement of the particles with filling of large pores, giving a higher coordination number (number of touching neighbor particles). [66]

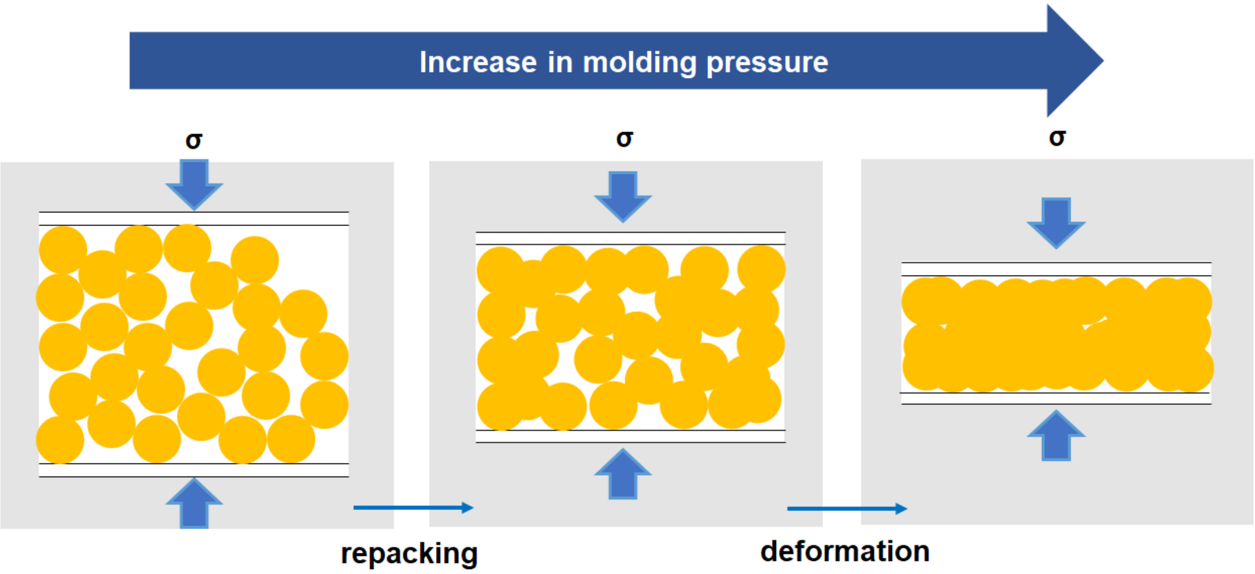

Figure 2.2 *Simplified view of the stages of powder compaction. Initially, repacking occurs with elimination of particle boundaries. With higher compaction pressures, particle deformation is the dominant mode of densification. Adapted from German R. M.*[66]

Increasing pressure provides better packing and leads to decreasing porosity with the formation of new particle contacts. The point contacts undergo elastic deformation, and at all points in the compaction cycle a residual elastic energy is stored in the compact. High pressures increase density by contact enlargement through plastic deformation. As the pressure increases, the large pores are eliminated first and the particle coordination number increases to further distribute the load. At very high compaction pressures, extensive deformation occurs, leaving only small pores. Continual pressurization beyond that level is of little benefit. The material response is similar to that of a dense solid. [66]

2.3.1 Hot-pressing

The application of a compressive pressure while heating; simultaneous application of heat and uniaxial pressure is also referred as hot-pressing or pressure sintering. Typical temperatures used in this method are between 70 to 85% of the melting temperature to achieve near theoretical densities. The major advantage of hot-pressing is that densification occurs quite readily and rapidly, minimizing the time for grain growth, which results in a finer and more uniform microstructure compared to sintering. This is because other densification mechanisms, like aggregate fragmentation, particle rearrangement, plastic flow and diffusional creep, are important in hot-pressing.[67] The major disadvantages, however, are the costs associated with tooling and dies and the process does not allow a continuous production since it usually occurs in an inert atmosphere. [68] Dies of graphite, carbide, boride, and molybdenum are often used, but they are expensive and subject to excessive wear and oxidation at temperatures greater than 1200 – 1500 °C. [67]

This method has the particular advantage that material preparation is much less critical than for any of the processes which require a sintering operation. Samples of relatively large grain size can be attained, although they require higher forming pressures and higher temperatures for satisfactory densification. In addition, materials that cannot be formed at all by sintering can be densified to moderately high densities with the hot-pressing technique. Samples can be readily prepared with most ceramic materials achieving 2 to 5% porosity. [69] It is also quite common to have grain orientation resulting from slip planes in the ceramic body which are parallel to the die walls. Other variants of pressure sintering are hot isostatic pressing (HIP) and pseudo-isostatic pressing. [67]

In HIP, an electric furnace is placed inside a pressure vessel. The pressurizing fluid is a gas like argon or helium. To achieve densification of a ceramic green body, the body must be evacuated and sealed in a gas-impermeable vessel. If there are any leaks in the seal, the ceramic body cannot be pressure sintered. Glass encapsulation or metal powder have been used as gas-impermeable vessels. The encapsulation layer is first sintered into a gas-impermeable layer before HIP. With glass encapsulation, a glass preform is used as a receptacle for the ceramic. The glass vessel is evacuated and sealed. It then deforms to the ceramic body's shape during HIP. In the pressure vessel, evacuation takes place and the temperature is raised to soften the glass until it forms a continuous layer on the ceramic body. The temperature and pressure are then increased to densify the ceramic body. HIP resolves the problems of density variation inside the ceramic, which is prevalent in hot-pressed ceramics. When sintering is performed before HIP, the combined process is called *sinter*-HIP or *post*-HIP.[67]In pseudo-isostatic pressing, an inert powder like hexagonal boron nitride or graphite is used as the "pressurizing fluid" because these powders are self-lubricating. The ceramic green body is placed in the inert powder within the die of the hot press. The temperature and pressure are increased, and densification takes place because the pressure is transmitted through the inert powder to the ceramic body. A true isostatic pressure distribution is not achieved, however, but densification takes place albeit with some degree of distortion.[67]

Three mechanisms are important to pore elimination; particle rearrangement, plastic flow and diffusional creep. The particle-particle rearrangement and deformation is important to the quality of the particle bonds [66], and plastic flow occurs when the effective stress exceeds the flow stress at the densification temperature. Nevertheless, diffusional creep controls final pore elimination during hot-pressing or HIP by migration of vacancies between grain boundaries.[70]

CHAPTER 3 Methodology

3.1 $Li_{6.25}Al_{0.25}La_3Zr_2O_{12}$ (Al-LLZO) Garnet Solid Electrolyte

In this dissertation, garnet with the composition of $Li_{6.25}Al_{0.25}La_3Zr_2O_{12}$ (hereinafter, LLZO) was studied based on its favorable attributes to enable membrane technology for solid-state batteries. A brief overview of the experimental procedures involved in synthesizing *cubic*-LLZO powder, processing and characterization will be discussed.

3.1.1 Synthesis and powder processing

LLZO powder was prepared through solid-state synthesis. Li_2CO_3, Al_2O_3, La_2O_3 and ZrO_2 were weighed in stoichiometric values and mixed for 24 h using a roller mill with ethanol as the solvent and 95 g of 2 mm in diameter zirconia balls as the media. 0.25 moles of Al was used to form 0.5 Li vacancies per formula unit to stabilize the cubic phase. 5 wt. % excess Li was added to compensate for Li loss during calcination and avoid formation of pyrochlore, $La_2Zr_2O_7$. The mixed powder was dried for 7.5 h under IR lamps, ground, and passed through a 400 µm sieve. The sieved powder was cold-pressed into 10 g pellets of 25.4 mm diameter at 19.61 kN for 2 min and then calcined on a MgO boat at 1000°C for 4 h in 1.75 $L \cdot min^{-1}$ flowing dry air (Heating rate of 1.7 $°C \cdot min^{-1}$, cooling rate of 4 $°C \cdot min^{-1}$). After calcination, the pellet was manually ground in an agate mortar and pestle and passed through a 75 µm sieve followed by X-Ray Diffraction measurements and Rietveld refinement for phase purity analysis.

3.1.1.1 Powder densification

3.1.1.2 Cold-pressing

The calcined LLZO powder was compacted in a 12.7 mm stainless steel die under 200 MPa for ten minutes to obtain a 63 % relative density (RD) green body. Die-wall friction effects were minimized using Li stearate as lubricant.

3.1.1.3 Hot-pressing

Rapid Induction Hot-Pressing (RIHP) was used to densify Al-LLZO green bodies into ≥ 97% RD disks. RIHP relies on the unique characteristics of induction heating through radio frequency coupling. A radio frequency power supply sends an AC current through an inductor, which is often a copper coil, to heat a susceptor (graphite or metal die) that resides in the inductor. In this process, there is no direct contact between the inductor and the susceptor/die. For this thesis, ~5 g of powder was hot-pressed in a 12.7 mm diameter graphite die with alumina plungers under Ar flow. All samples in this work were hot-pressed at 1225 °C for 40 min at 47.24 MPa with a heating rate of 120.5 $°C \cdot min^{-1}$ and cooling rates of 42.5 $°C \cdot min^{-1}$ to 800 °C and 22.5 $°C \cdot min^{-1}$ to 350 °C. The hot-pressed pellets were cut into 1.5 to 1.7 mm nominal thicknesses using a diamond saw using mineral oil as the cutting fluid. The LLZO hot-pressed disks were ground with a lapping fixture and 400 grit silicon carbide sandpaper onto a glass plate to achieve parallel faces. Further grinding was conducted with 600 and 1200 grit sandpaper.

3.1.1.4 Surface preparation

It has been demonstrated experimentally and corroborated via first-principles calculations that LLZO readily reacts with moisture and CO_2 present in the atmosphere forming a LiOH and a Li_2CO_3 interfacial layer [71]. The presence of these surface contaminants results in poor wettability by Li and high interfacial resistance [12]. Therefore, for all electrochemical characterizations in this dissertation, a surface treatment procedure was followed to remove these surface layers and facilitate charge transfer kinetics at the Li-LLZO interface [12]. LLZO samples that undergo this procedure exhibit ~ 2 $\Omega{\cdot}cm^2$ for interfacial resistance against Li and dramatic increase in Li wettability (contact angle ~ 95° as opposed to 125° or 142° when LiOH and Li_2CO_3 was present, respectively).

After grinding the LLZO disks, the samples were polished using consecutive decreasing diamond polishing abrasives of 15, 6, 1, 0.5 and 0.1 µm and a glycol-based diamond paste extender as the polishing fluid. Between polishing steps, the samples were wiped with cotton balls saturated with acetone and then ethanol to remove the residual polishing fluid from the surfaces. The samples were transferred into a dry (< 0.5 ppm H_2O) Ar-filled glovebox, placed on a MgO boat and heated in a muffle furnace at 400 °C for 3 h using 4 $°C{\cdot}min^{-1}$ as heating and cooling rates.

3.1.2 Reference Electrodes for three-electrode measurements

In electrochemical testing, the electrode under study is known by convention as the working electrode (WE) and the other electrode is termed the counter electrode (CE). When an electrode provides a constant, stable reference potential against which the potential of the WE can be measured~~.~~, it is defined as the reference electrode (RE). In a two-electrode cell configuration, the CE also acts as a RE. However, this configuration provides reliable results only if the passage of current does not significantly affect the potential of the CE. For this reason, a three-electrode cell configuration, where the CE and RE are physically different electrodes, is usually preferred. In this case, the current is passed between the WE and CE, and as a result the RE is not polarized by the flow of current so long as it is located outside the main current path. [72] However, the selection and design of REs for Li-ion batteries LIBs are very sensitive to experimental conditions, including chemical composition of the electrolyte and cell geometry.

A RE plays an important role in the study of many aspects of electrochemical systems since it can be used as an *in situ* diagnostic tool for practical LIBs or LMSSBs. This electrode carries no net current to avoid the effects of polarization and is selected based on its ability to provide a stable reference potential. A schematic of such a conventional arrangement is shown in *Figure 3.1* where the RE is a silver wire inserted into Ag_4RbI_5, which is, in turn, placed between two silver sheets that comprise the WE and CE. The reference electrode is placed as close as possible to the working electrode so as to minimize the part of the response due to the ohmic drop from the cell [26]

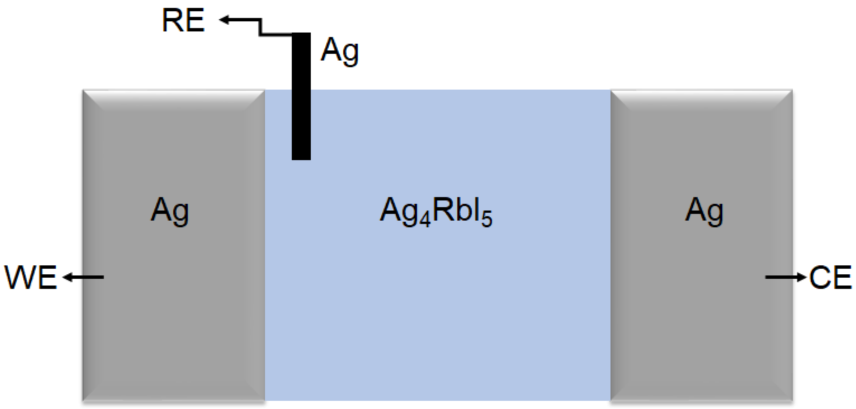

Figure 3.1 *Schematic representation of a conventional three-electrode cell. WE, CE and RE correspond to the working, counter and reference electrodes, respectively.*

The overpotential is directly determined by measuring the potential difference between the WE and RE in an arrangement such as that *Figure 3.1*. (In a four-electrode cell the potential difference must be measured between the two reference electrodes).

Various electrochemical techniques are routinely applied to investigate the behavior of LIBs/LMSSBs. Controlled-potential (e.g., cyclic voltammetry) and controlled-current (e.g., galvanostatic cycling) techniques enable the study of reactions at battery electrodes and measurement of battery capacity by applying large perturbations that drive the electrodes far from equilibrium. In the former technique, by making use of a potentiostat, the current between the WE and the CE is adjusted in order to achieve the desired potential difference between WE and CE. Then, the resulting current flowing between the WE and CE is recorded as a function of time or potential (Figure 3.2a). In the latter technique, by making use of a galvanostat, a constant current is applied between WE and CE and the resulting potential difference between WE and RE is recorded as a function of time or current (Figure 3.2b). [72]

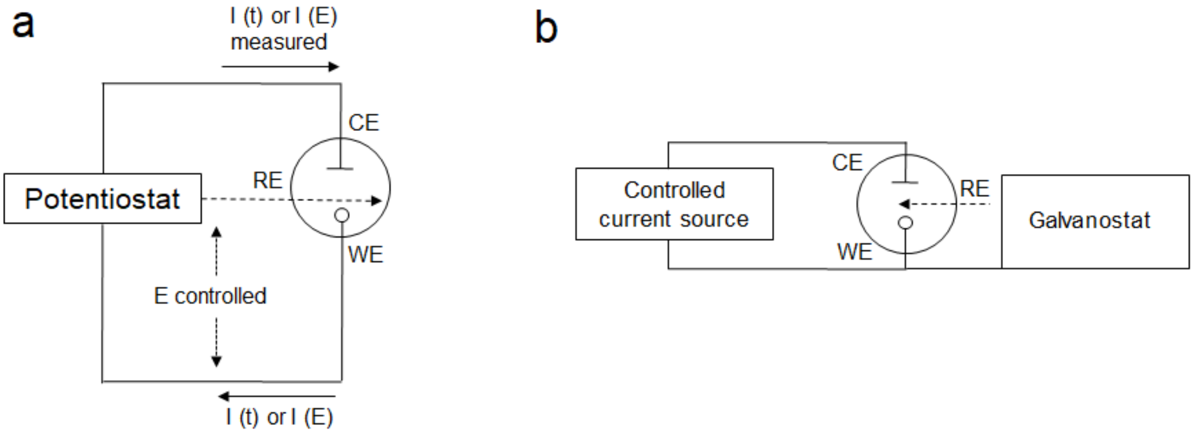

Figure 3.2. *Schematic representation of a) potentiostatic and b) galvanostatic experiments*

Controlled-potential experiments can be an extremely useful and versatile tool for fundamental electrochemical studies, e.g., reaction kinetics at single electrodes or electrolyte electrochemical stability.[72] In galvanostatic cycling, the use of a RE enables the simultaneous acquisition of potential profiles of both positively and negatively charged electrodes, in addition to that of the full cell, which is not possible in a two-electrode cell configuration. [73–75]

Much of the current interest in batteries involves Li-based systems with non-aqueous electrolytes including this thesis. Thus, the use of pure Li as a reference electrode will be the focus here.

3.1.2.1 Li Reference Electrodes.

In three-electrode measurements on solid electrolytes using pellets or thin films, the reference electrode is placed either on the same side as the WE or CE. The RE is often made of the same material as the working electrode, and therefore, it does not have a fixed potential. The potential of the reference electrode is determined by the thermodynamic equilibria established between the solid electrolyte, the electrode and the gaseous environment for a given temperature. [76]Although Li metal has been the most commonly employed material, some important considerations need to be taken into account when using it as a RE, such as chemical reactivity against the electrolyte and cell geometry. In this work, Li metal was used as a RE against LLZO SSE, as its chemical stability against metallic Li[34] simplifies the analysis. Furthermore, the transport properties of LLZO have been well documented elsewhere[12,33,77,78] allowing a thorough analysis of the Li-LLZO interface stability presented in Chapter 6.

3.1.2.2 Geometric Requirements of Solid Electrolyte Cells with a Reference Electrode

In general, practical constraints to the placement of the reference electrode are much greater for solid electrolytes where the reference electrode must be located on an exposed electrolyte surface. This is a direct consequence of the inability of solids to make intimate contact with each other, translating into higher interfacial resistances as it would be observed when using a liquid electrolyte Thus, Winkler et al.[79] investigated the effect of geometry of various three-electrode, solid-electrolyte based cells on the reliability of measuring polarization resistances and elucidated the sources of error. Even though the analysis was performed for solid oxide fuel cells, the conclusions are in principle valid also for other three-electrode electrochemical cells. [79]

In order to avoid the occurrence of electrochemically driven reactions over the reference electrode that would perturb the potential of the reference electrode, Winkler et al. [79] developed a criterion that imposes constraints on the positioning and size of the reference electrode. The normalized potential difference, Δ_{Ref}^{*}, along the reference electrode should be less than 10^{-3}. Δ_{Ref}^{*} is defined as follows:

$$\Delta_{Ref}^{*} = \left[\frac{\Delta V_{Ref}}{\Delta V_{j}}\right] \qquad (3.1)$$

Where ΔV_{Ref} is the potential difference along the reference electrode and ΔV_{Rj} is:

$$\Delta V_{Rj} = R_{j} I \qquad (3.2)$$

Where I is the total current and R_j is the total internal resistance of the cell. An alternative method to determine if the normalized potential satisfies the criterion is to confirm that the cell geometry lies to the right of the solid line in the following figure ($\Delta_{Ref}^{*} < 10^{-3}$).

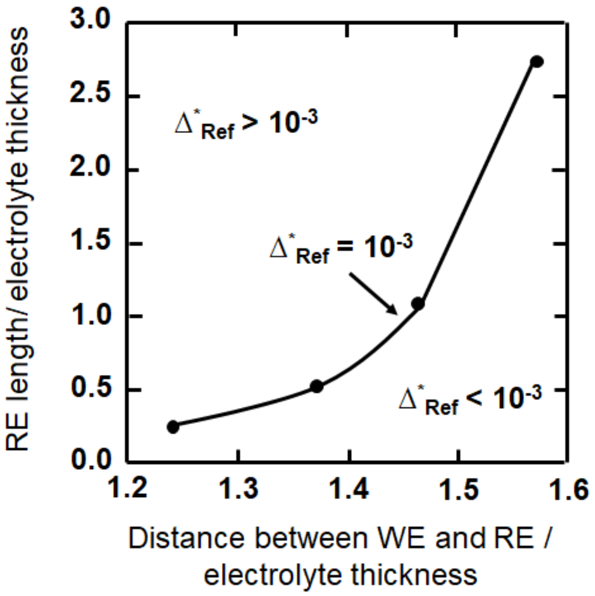

Figure 3.3 *Geometrical requirements in a three-electrode cell to avoid occurrence of electrochemically driven reactions over the reference electrode (RE). WE correspond to the working electrode. Adapted from Winkler et al.*[79]

If the electrolyte is relatively thick or resistive (pellet-like), it is possible to place the reference electrode "far" from the current-carrying electrodes as long as it complies with the aforementioned criteria. [79]

Taking into account the Winkler *et al*. geometrical requirements in a three-electrode cell, a custom-made solid-state cell was designed and tested to validate its response as shown in Chapter 6, section 6.2.1 (p.98)

3.1.3 Characterization

3.1.3.1 Phase purity analysis

The crystal structure and phase purity of the as-synthesized LLZO powder and hot-pressed pellets was determined via X-Ray Diffraction (XRD) measurements with CuK_α X-Ray radiation operating at 40 kV and 20 mA between 15 to 65 ° 2θ with a step size of 0.02°. The analysis was carried out using Bragg's law, which calculates the angle where constructive interference from Xrays scattered by parallel planes of atoms produce a diffraction peak. The wavelength was fixed to 1.54 Ȧ, consequently, a family of planes produces a diffraction peak only at a specific angle 2θ [80].

$$\lambda = 2 \cdot d_{hkl} \cdot sin\theta \tag{3.3}$$

Where d_{hkl}, the vector magnitude is the distance between parallel planes of atoms in the family (hkl) [80].This equation is used to create an XRD pattern that plots the intensity as a function of 2 θ. Rietveld structural refinements of the XRD patterns were performed to determine the weight fraction of secondary phases.

3.1.3.2 Electrochemical Impedance Spectroscopy (EIS)

In order to characterize the microstructures and properties of electroceramics, techniques are required that can probe or distinguish between the different regions of a ceramic such as impedance spectroscopy.[81] This AC impedance measurements are made over a wide range of frequencies and the different regions of the material are characterized according to their electrical relaxation times or time constants. [82]

Using polycrystalline LLZO as an example (*Figure 3.3a*), the physical transport processes are measured using EIS and the following equivalent circuit (*Figure 3.3b*).

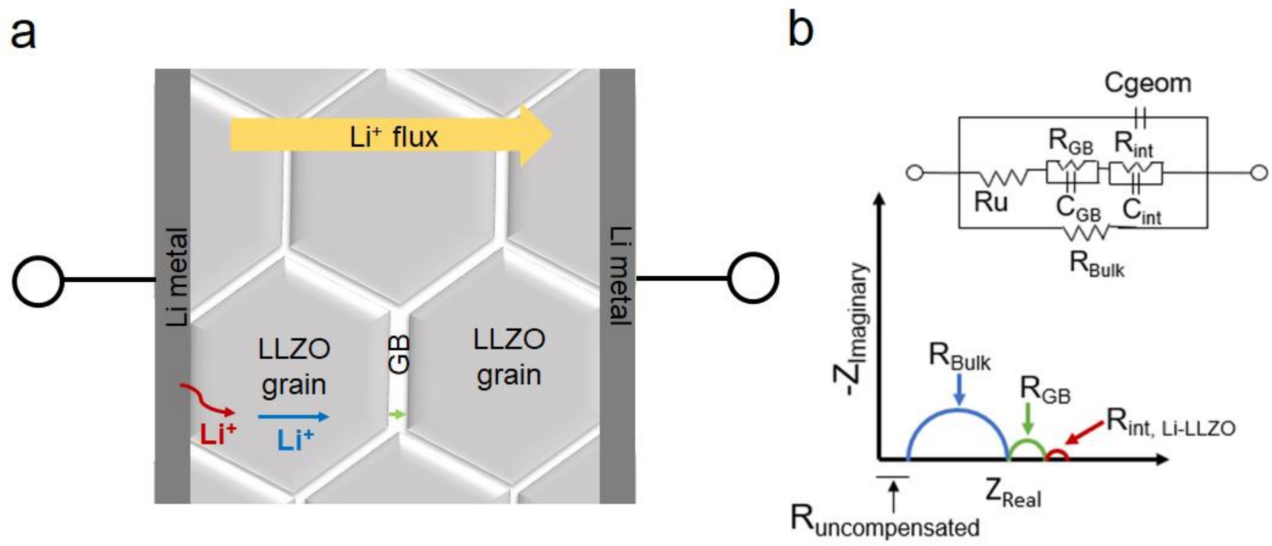

Figure 3.4 *Hypothetical Electrochemical Impedance Spectroscopy (EIS) spectrum of a Li-LLZO-Li symmetric cell. (a) Schematic of the cell configuration highlighting the direction of the ionic current (b) Equivalent circuit model representing the physical processes in the cell and its corresponding spectrum*

Different regions of a ceramic sample are characterized by a resistance and a capacitance, usually placed in parallel. The characteristic relaxation time or time constant, τ, of each ‘parallel RC (resistive/capacitive) element’ is given by the product of R and C:

$$\tau = \mathrm{R} \cdot \mathrm{C} \tag{3.4}$$

In the frequency domain, RC elements are separable due to the relation shown in equation

$$w_{max} \cdot R \cdot C = 1 \tag{3.5}$$

which holds at the frequency of maximum loss, w_{max}, in the impedance spectrum. From the impedance spectrum, it is therefore usually possible to identify different RC elements and assign them to appropriate regions of the sample. The values of the individual R and C components may then be quantified. The capacitance values expected for different phenomena such as bulk, grain boundary and electrode-electrolyte interface, among others for ideal electroceramics can be found in Irvine *et al*.[83]

3.2 LPS 75-25 Solid Electrolyte

3.2.1 Synthesis: Mechano-chemical

Glass electrolytes are commonly prepared by melt quenching. The Li_2S-P_2S_5 (LPS) family of glasses can be prepared by the quenching method; however, the melting reaction has to be carried out in sealed quartz tubes because of high vapor pressure of P_2S_5 at high temperatures. These glasses are preferably synthesized by mechanical milling or mechano-chemical synthesis that takes place at room temperature and normal pressure[58] The mechanical milling technique was originally developed as a method to synthesize alloys.[84] However, recently, it has also been used as an amorphization method. [85] Amorphization by mechanical milling consists of reacting crystalline solid precursors through the severe cyclic deformation that ball-milling provides. [85]

Even though mechano-chemical synthesis procedures allow bulk processing of amorphous materials, the end-product has inevitably particle boundaries. Such microstructural features have been reported in literature as preferential locations where metallic Li propagates under galvanostatic testing. [15,16,86] Thus, elimination of particle boundaries and pores to attain a microstructure that resembles a melt-processed glass is the focus in Chapter 5.

In Chapters 4 and 5, LPS 75-25 glass solid electrolyte was prepared through mechanochemical synthesis. Starting with crystalline powders of Li_2S (99.98%, Aldrich) and P_2S_5 (99%, Sigma Aldrich), the precursors were mixed in an agate mortar and pestle and placed in a 45-cc zirconia pot with 10 zirconia balls of 10 mm in diameter and 10 zirconia balls of 5 mm in diameter.

For Chapter 4, the pots were spun at 370 RPM for 20 h in a Planetary Micro Mill (Pulverisette 7, Fritsch GmbH), with 2-hour intervals of milling followed by 5-minute rest intervals at room temperature. The zirconia pots were sealed in a dry Ar-filled glove box (water concentration below 0.5 ppm), placed inside stainless steel vessels and transported in an inert atmosphere. The amorphization of the material was validated by characterization of the crystallization temperature via DSC at a heating rate of 5 °C·min^{-1}, typically observed at 225 ± 5 °C. However, such crystallization temperature was not consistently achieved under those synthesis conditions. Thus, further optimization of the synthesis procedure was conducted, which resulted in a higher energy mechanical milling procedure to ensure complete amorphization and assure consistency between batches. In addition, the synthesis time was reduced by half. This procedure was followed in Chapter 5; the pots were spun at 510 RPM for 10 h in a Planetary Micro Mill (Pulverisette 7, Fritsch GmbH), with 2-hour intervals of milling followed by 10-minute rest intervals at room temperature. As before, amorphization was validated by characterization of the crystallization temperature via DSC at a heating rate of 5 °C·min^{-1}, typically observed at 225 ± 5 °C. The powder processing procedure followed for both LPS studies is explained in detail in their respective chapter.

CHAPTER 4 Effect of Processing Conditions on the Electrochemical Behavior of LPS 75-25 Solid Electrolyte

4.1 Introduction

Improving the performance and safety of batteries can be achieved through the development and integration of solid-state ceramic electrolytes enabling novel cell configurations and chemistries.[32,87] While numerous SSEs exhibit high conductivity, few examples of viable bulk-scale LMSSBs have been reported. Recently, researchers have developed SSEs based on crystalline ceramics, glass, and glass-ceramics. However, due to the myriad material property and processing criteria that must be considered, the development of viable LMSSB has been challenging. Sulfide-based ion conductive glasses are appealing due to the inherently more polarizable nature of the sulfide anion compared to oxide anions. Glassy solid electrolytes in the LPS system have demonstrated Li-ion conductivities of 10^{-4} $S \cdot cm^{-1}$ at room temperature.[11] Furthermore, glass SSEs being amorphous are isotropic conductors, thus ionic transport is not affected by orientation or the presence of grain boundaries, respectively. Moreover, the inherently low elastic modulus of LPS enables densification of powders at room temperature.[88,89] There are numerous aspects that make sulfide glasses a promising class of ionic conductors; however, transitioning SSE such as LPS into high performance LMSSB requires an understanding of the DC cycling electrochemical stability of the solid electrolyte against metallic Li. Specifically, to achieve relevance to vehicle electrification, demonstrating current densities approaching the 1 mA·cm^{-2} range is required. It was hypothesized that increasing the densification temperature, above room temperature at fixed pressure, should increase the LPS relative density and enhance particle-particle adhesion. In turn, the increased density and adhesion between particles should affect the rate at which current can be passed through the cell without short-circuiting.

Differential Scanning Calorimetry (DSC), X-Ray Diffraction (XRD), Scanning Electron Microscopy (SEM) and geometrical density measurements were conducted to correlate the LPS 75-25 processing conditions with crystallinity, morphology, and relative density. DC galvanostatic measurements were conducted to measure the critical current density (CCD, current at which short circuit is observed) to correlate it with the processing conditions. The overarching goal of this work was to gain a better understanding of the DC cycling electrochemical stability of the Li-LPS interface to facilitate the development of SSB using metallic Li electrode.

4.2 Results and Discussion

4.2.1 Materials Characterization

4.2.1.1 LPS Thermal Behavior

Figure 4.1 shows the DSC spectra of the LPS amorphous powder at different heating rates. As the heating rate increases, the crystallization temperature of the glass electrolyte increases, which is consistent to previous results reported by Eom et al.[90] on differential thermal analysis (DTA) measurements for the LPS 78-22 system. Since the heating rate used in this work was 0.7 ± 0.1 °C·min^{-1}, crystallization of LPS glass was not expected below 190 °C (onset temperature) for hot pressing and heat treatment (170 °C). DSC spectra of the LPS amorphous powder obtained by mechanical milling for 20 h and further pelletized under different processing conditions was collected at a fixed heating rate of 5 °C·min^{-1}. All powders showed one exothermic peak due to crystallization at 225 ± 4 °C suggesting that all powders had similar thermal behavior. The glass transition phenomenon was not clearly observed before the crystallization peak, but the crystallization behavior with the following X-ray diffraction pattern indicated that the as-milled material was amorphous.

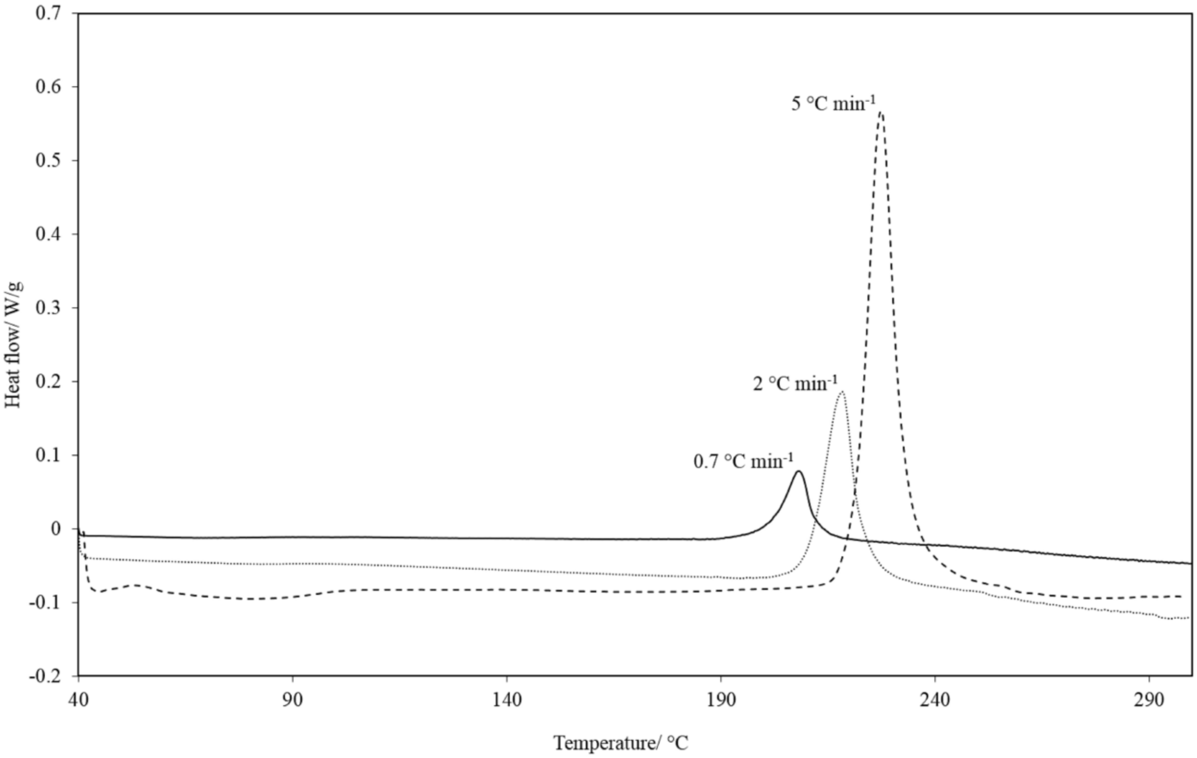

Figure 4.1 *Effect of heating rate on the crystallization temperature of LPS via Differential Scanning Calorimetry (DSC)*

4.2.1.2 LPS long-range order analysis

XRD measurements were carried out for the LPS pellets prepared (Figure 4.2). No obvious diffraction peaks were observed in the cold-pressed (25 °C) and hot-pressed samples at 130 °C and 150 °C patterns, confirming their lack of long-range order. From 170 °C, observable diffraction peaks were identified as the highly conductive metastable crystalline phase thio-

LISICON III analog. The patterns are consistent with XRD measurements reported by Kanno et al.[59] for $Li_{4-x}Ge_{1-x}P_xS_4$ (LGPS, when x = 0.8), being $Li_{3.2}P_{0.96}S_4$ the stoichiometry for the thio-LISICON III analog. Despite the absence of Germanium in the metastable crystalline phase, a presumable explanation for the crystallographic similarities is to assume that the Li-rich and phosphorous-poor $Li_{3+5x}P_{1-x}S_4$ phases are formed in this type of glass ceramic by aliovalent substitution, P^{5+} ←→ $5Li^+$.[91] Between 170 °C and 250 °C, the preferred higher conductivity crystalline thio-LISICON III analog phase was present, however when hot pressing above 250 °C, the lower conductivity Li_3PS_4 phase formed as the minority phase. Likewise, hot pressing at 300 °C should result in decreased conductivity owing to the presence of the lower conducting Li_3PS_4.

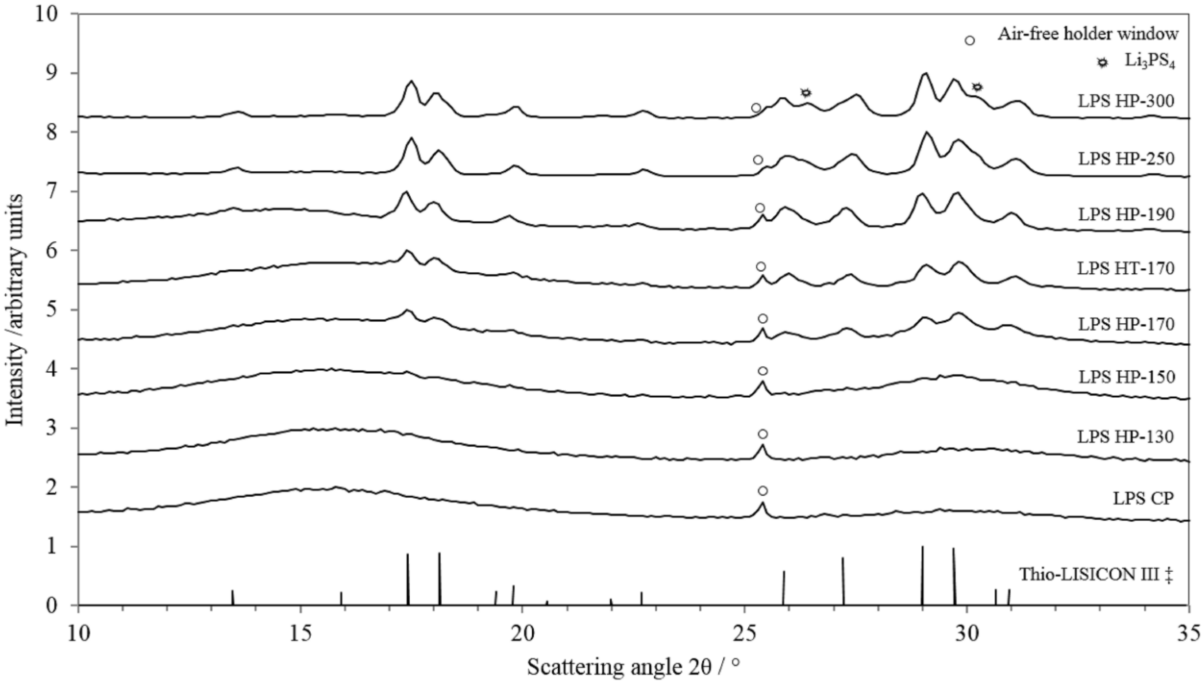

‡ Adapted from Kanno, R. and Murayama, M. *J. Electrochem Soc.* **148** (7) A742-A746 (2001) figure 1

Figure 4.2 *Effect of hot-pressing temperature on LPS crystallinity via X-Ray Diffraction (XRD)*

The metastable thio-LISICON III analog phase was identified in both hot-pressed and heat-treated pellets at 170 °C, indicating that the precipitation of the crystalline phase from the mother glass was determined by temperature and is pressure independent given that the duration of the soak segments were the same on both samples. The presence of a crystalline phase below the onset temperature (190 °C with a heating rate of 0.7 $°C \cdot min^{-1}$) determined by DSC measurements is likely attributed to nucleation and crystal growth phenomenon previously reported in glasses [92] including the LPS binary system.[90] Eom et al.[90] showed that in LPS 78-22 nucleation and crystal growth occur simultaneously between 160 to 220 °C with a maximum nucleation rate and crystal growth rate at 170 °C and 230 °C, respectively. These results are in agreement with the observable diffraction peaks for the pellets processed (hot-pressed or heat-treated) at 170 °C and 190 °C (below the observed crystallization temperature, 207 °C) suggesting that both nucleation and grain growth occurred during hot pressing and heat treatment.

4.2.1.3 LPS Microstructural Analysis

Micrographs of the fractured surfaces of the LPS cold-pressed (25 °C), hot-pressed at 170 °C, heat-treated at 170 °C and hot- pressed at 300 °C are shown in Figure 4.3 (a, b, c, and d, respectively). The SEM images show a cross section with particles in the micron- scale range and a few pores. The volume fraction of porosity was consistent among samples regardless of the hot pressing or heat treatment conditions.

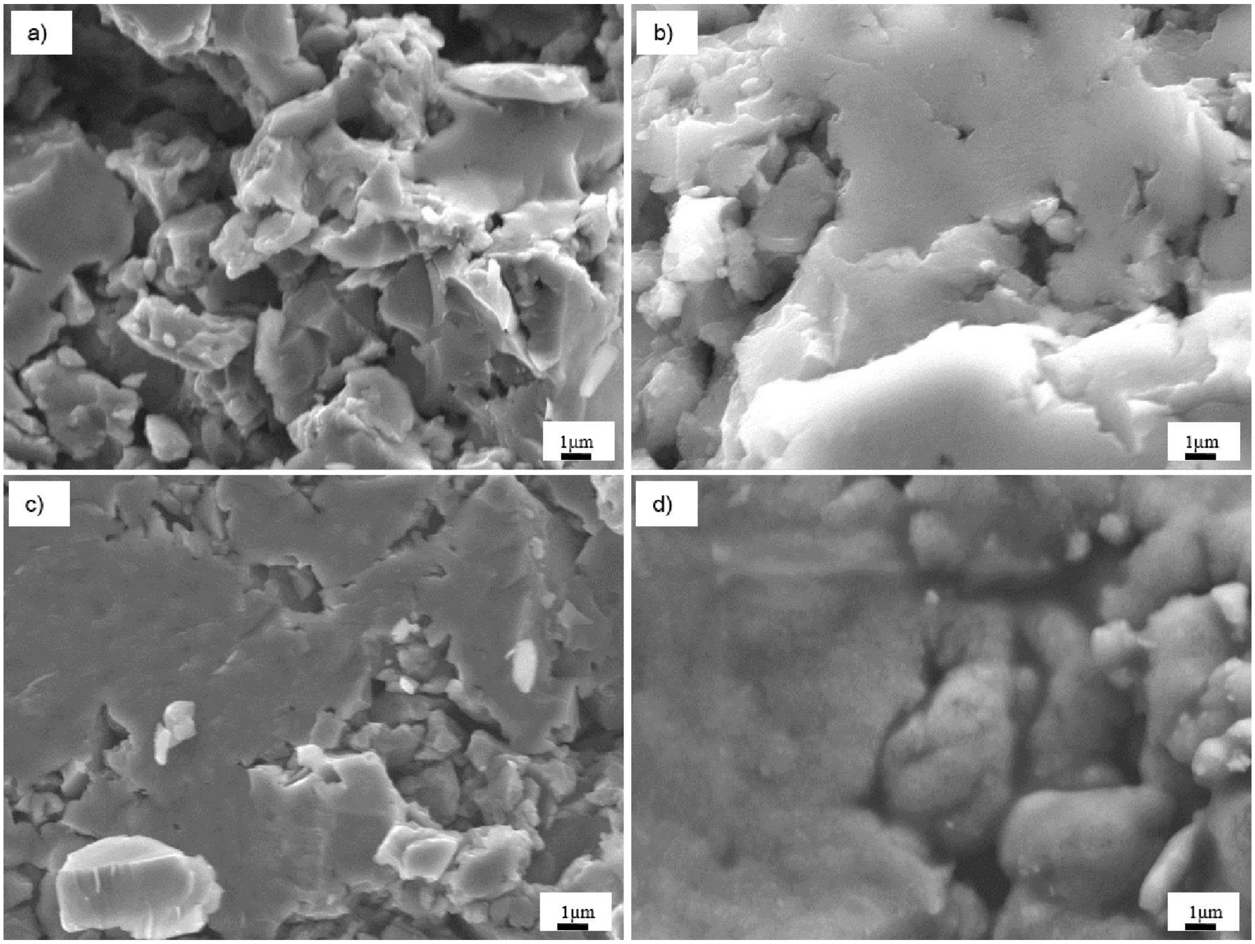

Figure 4.3 *SEM fractographs of the LPS 75-25 of (a) Cold-pressed pellet (b) Hot-pressed pellet at 170 °C (c) Heat-treated at 170 °C and (d) Hot-pressed at 300 °C*

The calculated relative density (Figure 4.4) further confirms that the hot-pressed (pressed between 130 and 300 °C) or heat treated (170 °C) pellets exhibit similar porosity. The mass density of LPS cold-pressed, hot-pressed at 170 °C, heat-treated at 170 °C and hot-pressed at 300 °C was 1.61 ± 0.06 $g{\cdot}cc^{-1}$, 1.46 ± 0.01 $g{\cdot}cc^{-1}$, 1.54 ± 0.01 $g{\cdot}cc^{-1}$ and 1.57 ± 0.03 $g{\cdot}cc^{-1}$, respectively, as determined from their mass and physical dimensions. The calculated bulk densities were divided by the density of a transparent glassy pellet (1.88 $g{\cdot}cc^{-1}$).[88] Thus, the relative density of all pellets ranged from 77 to 83%. Based on these results, it is believed that densification, through thermally activated processes at 47 MPa, was not achieved. Sintering and grain growth theory states that the only mechanisms apart from viscous flow or plastic deformation that can lead to shrinkage and elimination of pores are grain boundary and bulk diffusion.[68] Because the LPS in this work is primarily amorphous or nano-crystalline, the grain boundary contribution to densification is negligible compared to bulk diffusion. Typically, 0.5–0.9 of the melting point (in Kelvin) is required to chemically bond particles and reduce the porosity by bulk diffusion .[93] Hayashi et al.[61] showed that amorphous LPS (3:1) melts at 460 °C via DTA using a heating rate fixed at 10 $°C \cdot min^{-1}$. Therefore, contradictory to what was expected, no significant increase in relative density was observed in any of the hot-pressed pellets.

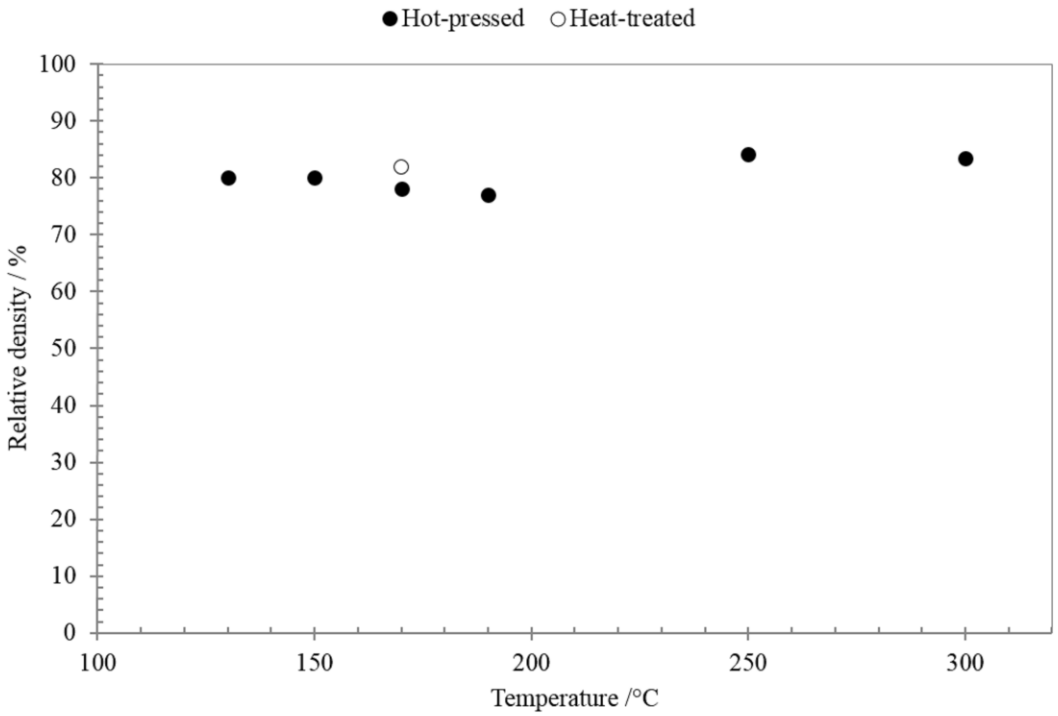

Figure 4.4 *Relative density of LPS hot-pressed and heat-treated pellets as a function of processing temperature*

4.2.2 Electrochemical Characterization

Figure 4.5 shows the EIS spectra of the HP-170 and HT-170 pellets. Considering that ideally each parallel RC (Resistive- Capacitive) constant phase element (CPE) gives rise to a semicircle,[83] the HT-170 was the only sample that showed a distinctive additional semicircle in the low-frequency range (additional CPE). This semicircle could be attributable to either particle-particle boundary resistance or charge transfer resistance. LPS HP-170 and HT-170 not necessarily follow conventional values agreed on sintered ceramic electrolytes[83] given that metastable crystalline phases are present in a non-densified form. Capacitance values for bulk transport phenomena have been found in the order of 10^{-10} F for $80Li_2S$-$20P_2S_5$[94] and 10^{-9} F for $75Li_2S$-$25P_2S_5$ at room temperature. Thus, the low frequency semicircle observed in the heat-treated sample could be assigned to the lack of particle-particle adhesion that was considerably reduced by hot pressing.

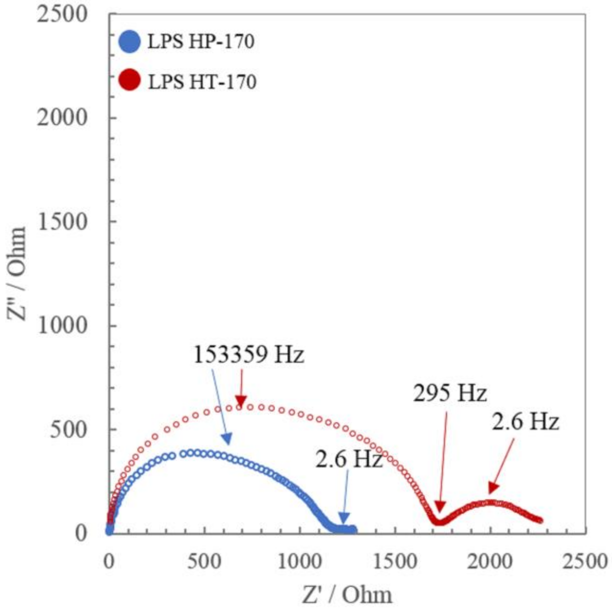

Figure 4.5 *Electrochemical impedance measurements of Li-LPS-Li symmetric cells at room temperature, 316 kPa. Nyquist plots for LPS hot-pressed at 170 °C (blue markers) and heat-treated at 170 °C (red markers) from 7 MHz down to 50 mHz*

A DC asymmetric polarization test at room temperature was conducted on the LPS CP, LPS HP-170, LPS HP-300 and LPS HT-170 where Li-ions passed through the LPS pellets over a range of current densities (Figure 4.6). These were selected among all pellets to exemplify the polarization behavior observed on the three different processing conditions presented in this work, e.g. pressed at room temperature, heated without pressure and simultaneous application of heat and pressure. Ohmic behavior (linear current-voltage behavior) was observed for every cell subjected to 0.01 $mA \cdot cm^{-2}$ (inset image in Figure 4.6). Moreover, a comparison between DC and AC measurements (Table 4.1) indicated that observations under dynamic and steady conditions are consistent with each other for this current density segment, with a maximum difference of 9% for HT-170. At 0.05 $mA \cdot cm^{-2}$ each cell exhibited Ohmic behavior except for the cells consisting of the cold-pressed and heat-treated pellets. The latter showed the most prominent deviation from Ohmic behavior at 0.05 $mA \cdot cm^{-2}$ showing an increase in potential from 0.1 to 0.6 V, whereas the cold-pressed pellet showed an increase in potential from 0.1 to 0.2 V. This may suggest that the simultaneous application of heat and pressure improved the electrochemical stability for hot-pressed pellets (LPS HP-170 and LPS HP-300). For example, all hot pressed LPS pellets followed Ohmic behavior for the majority of the 0.1 $mA \cdot cm^{-2}$ current density segment, while the impedance of the cold-pressed and heat-treated LPS pellets increased by > 10X higher than the impedance predicted by Ohm’s law at the same current density. At the end of the 0.1 $mA \cdot cm^{-2}$ step, however, the hot-pressed LPS pellets started to deviate from Ohmic behavior at the end of the 1 h current segment being more prominent in the LPS HP-300 followed by a drop in the output potential difference towards the end of the 0.1 $mA \cdot cm^{-2}$ segment. At 0.05 and 0.1 $mA \cdot cm^{-2}$, LPS HT-170 exhibited the highest polarization among samples analyzed. This behavior might correspond to lack of particle-particle adhesion within the microstructure that is attained by applying pressure and heat simultaneously.

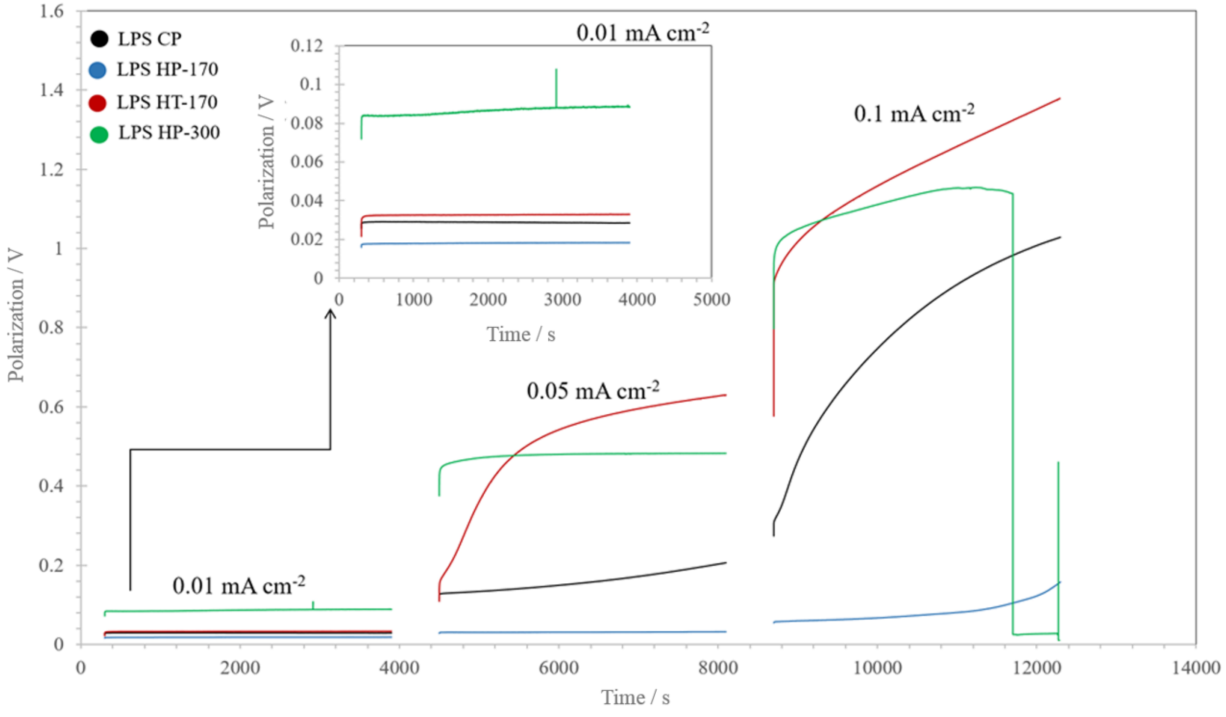

Figure 4.6 *Galvanostatic polarization curves of Li-LPS-Li symmetric cells, asymmetrically cycled at room temperature at 0.01, 0.05 and 0.1 mA·cm*$^{-2}$

Significant deviation from Ohm's law and wide swings in potential were observed at 0.5 and 1.0 mA·cm^{-2} for all the cells. Figure 4.7 shows the galvanostatic polarization curves for (a) LPS CP, (b) LPS HP-170, (c) LPS HT-170 and (d) LPS HP-300. At 0.5 mA·cm^{-2}, all the pellets except for LPS HP-170 exhibited deviation from Ohm's law, first polarizing up to higher potential, followed by a drop in potential near 0 V. After initially dropping to 0 V, the output potential difference was erratic for the duration of the 0.5 mA·cm^{-2} current segment and for the entire 1.0 mA·cm^{-2} current segment. The cell with the LPS HP-170 pellet showed no cell potential drop at 0.5 mA·cm^{-2} for 1 h, although the cell polarization notably increased within the polarization period.

The drop in cell potential for the LPS HP-170 pellet was observed at 1.0 mA·cm^{-2}, similar to what was observed in the LPS CP pellet at 0.5 mA·cm^{-2}.

Sample	DC Ohmic drop [Ohm]	AC Total impedance [Ohm]	Divergence [%]
LPS CP	2165	2186	1
HP-170	1360	1276	6
HT-170	2482	2260	9
HP-300	6700	6494	3

Table 4.1 *Cell resistance comparison between DC and AC measurements at 0.01 mA·cm^{-2}*

The critical current density for the LPS electrolyte was taken as the current segment value where the short circuit occurred. The decrease in potential is believed to be a result of the propagation of an electronically conducting phase between Li electrodes through the entire thickness of the solid electrolyte; also referred as short circuit. It is believed that the electronically conductive phase that penetrates the electrolyte is metallic Li, which is consistent with observations by Ishiguro[95] and Sharafi et al.[96] in solid-state cells consisting of Li-$Li_7La_3Zr_2O_{12}$-Li and Nagao et al.[97] in Li-80Li_2S-20P_2S_5(mol %)-Li glass-ceramic electrolyte. Nagao et al.[97] showed that at current densities higher than 1.0 mA·cm^{-2}, Li was deposited locally, which resulted in the increase in length of pre-existing cracks. In addition, the growth of Li propagated from regions at the Li-LPS interface where there were pre-existing cracks. In this study, the polarization behavior followed by a short circuit might be affected not only by the current density applied, but also by microstructural integrity. For example, different polarization behavior was observed between LPS

HT-170 and LPS HP-170. Even though both exhibited the presence of the highly conductive metastable crystalline phase thio-LISICON III analog, the lack of pressure during heating, resulted in less or no particle-to-particle bonding in the HT-170 pellet compared to the HP-170 pellet (Figure 4.5). The lack of chemistry between particles could have facilitated the Li deposition and growth behavior. The cell with the pellet hot-pressed at 170 °C was the only pellet that did not exhibit the short-circuiting phenomenon at 0.5 $mA\cdot cm^{-2}$. The aforementioned results are summarized in Table 4.1. A plausible explanation for this optimum hot pressing temperature (170 °C) could be correlated not only to the phase present that increases the ionic conductivity, i.e., the LPS hot pressed at 170 °C, had the highest conductivity among all the densification temperatures, but also the adhesion between particles that facilitated the ionic transport within the solid electrolyte. As described above, hot pressing above 250 °C, caused the partial transformation of the highly ion-conducting thio-LISICON III analog to the lower conductivity Li_3PS_4. Since the stoichiometric Li_3PS_4 is known to exhibit significantly lower ionic conductivity, higher polarization may have resulted, thus accelerating the short-circuiting phenomenon. Nevertheless, the cause of failure in these systems may be influenced by other factors aside from atomic/microstructure properties of the electrolyte, such as large Li potential gradients across the electrolyte leading to Li extraction from the electrolyte, or localized high electric field strength at the metallic Li anode/electrolyte interface leading to Li metal propagation. Further work is needed to elucidate the effect of these variables to gain a better understanding of the failure mechanism (Table 4.2).

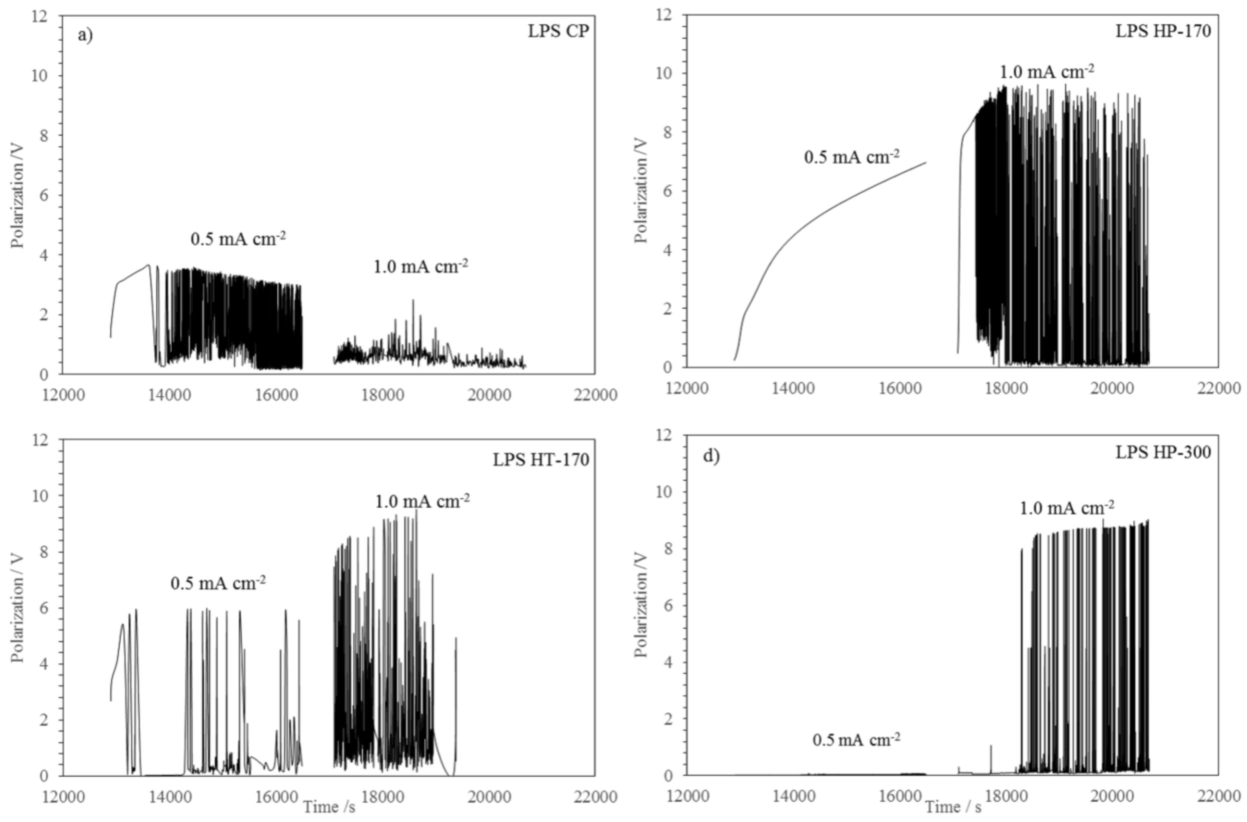

Figure 4.7 *Galvanostatic polarization curves of Li-LPS-Li symmetric cells of (a) LPS CP (b) LPS HP-170 (c) LPS HT-170 and (d) LPS HP-300 asymmetrically cycled at room temperature at 0.5 and 1.0 mA·cm^{-2}*

Sample	Pressing temperature [°C]	Deviation from linear behavior [mA·cm^{-2}]	Critical Current Density [mA·cm^{-2}]	Ionic conductivity at RT [mS·cm^{-1}]
LPS CP	25	0.05	0.5	7.0 x 10^{-5}
LPS HP-170	170	0.1	1.0	1.4 x 10^{-4}
LPS HT-170	170	0.05	0.5	1.2 x 10^{-4}
LPS HP-300	300	0.1	0.1	2.0 x 10^{-5}

Table 4.2 *Deviation from linear behavior and critical current density of Li-LPS-Li cells during DC asymmetric polarization*

4.2.3 Li/LPS Surface Analysis

Table 4.3 shows images of the surface analysis carried out on the LPS-CP, LPS HP-170, LPS HT-170, and LPS HP-300 pellets after DC asymmetric polarizations were completed. All the pellets exhibiting discoloration showed clear evidence of an interfacial phase formed between the Li metal electrode and the electrolyte, which is believed to be a byproduct of the decomposition of the electrolyte. To determine the composition of the byproducts, Raman analysis was conducted.

Cold-pressed (25°C)	170°C Hot-pressed	170°C Heat-treated	300°C Hot-pressed
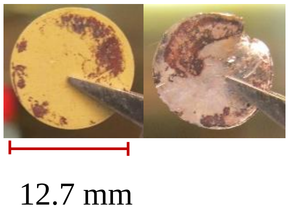		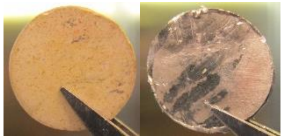	

Table 4.3 *LPS pellets (Li stripping side) and Li foil surfaces after DC asymmetric polarization*

4.2.3.1 Raman Analysis

To determine the structural units of the decomposition phase, Raman point analysis was performed on the surface of the LPS CP pellet. Figure 4.8a shows the Raman spectra of the whole range evaluated on single spots identified on the inset image. Figure 4.8b shows the region near the main band (418 cm^{-1}) observed in all spectra, which is attributed to the stretching vibration of the P–S bonds.[65]

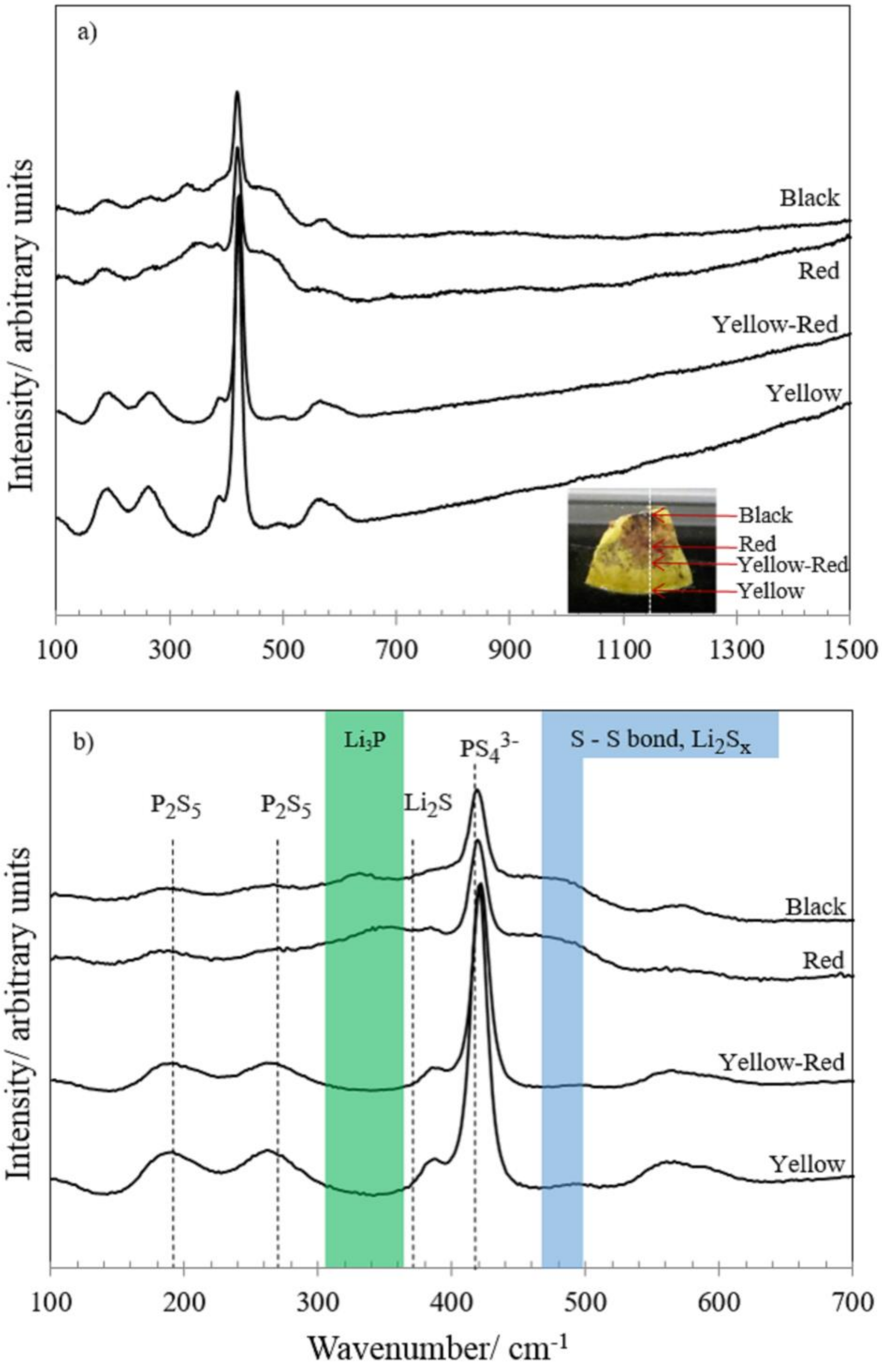

Figure 4.8 *Raman spectra on LPS CP surface after DC asymmetric polarization (a) whole range; 100 to 1500 cm^{-1}, inset shows an image of the sample and regions analyzed (b) specific range; 100 to 700 cm^{-1}*

Meyer [98] showed that the Raman spectra of S6 and S7 sulfur allotropes showed a band at 471 and 481 cm^{-1}, respectively, at 300 K. In addition, Jaroudi et al.[99,100] have reported that the Raman spectra of alkali metal polysulfides, M_2S_x (M = Na and K, $2 \leq x \leq 5$) showed a band at around 470 cm^{-1}. Thus, the band observed at around 480 cm^{-1} could be attributable to S-S bonds and/or Li polysulfides as a by-product of decomposed reaction of the LPS electrolyte for the black and red species. The local structure of the red species is similar to that of the black species suggesting that the difference between them might correspond to concentration not composition. Moreover, Lin et al.[101] showed that an electrolyte that contains P_2S_5 formed a passivation layer on the surface of Li metal. Combined XRD and Raman analyses revealed that the main component was Li_3PS_4, a stable stoichiometric compound in the ternary phase diagram of the Li-P-S system along with Li_2S, Li_3P and $Li_4P_2S_6$.[91] Thus, observed peaks between 300 – 400 cm^{-1} for black and red species are presumably due to phosphorus compounds. Ong et al.[102] predicted that $Li_{10}P_3S_{12}$, decomposes in Li_2S and Li_3P. Additionally, Wenzel et al.[103] reported that $Li_7P_3S_{11}$ forms an interphase against Li metal composed of Li_2S, Li_3P and polyphosphide compounds. Thus, the prediction that polysulfides and Li_3P are present at the Li-LPS interface would be consistent with the peaks observed at around 480 cm^{-1} and 300 – 400 cm^{-1} respectively, for black and red species (Table 4.3).

Further surface and cross-sectional materials characterization as X-ray photoelectron spectroscopy (XPS) and Energy Dispersive Spectroscopy (EDS) are necessary to elucidate the composition of the decomposed species including binding information at the surface and within the bulk.

4.3 Conclusions

This is the first study to measure the critical current density (current density at which short-circuit of the cell occurs) likely due to Li metal penetration of the LPS 75-25 system, and how it can be increased by modifying the processing conditions of the solid electrolyte. It was observed that the presence of the highly conductive phase thio-LISICON III analog, and improved adhesion between particles by hot pressing, exhibited higher critical current densities compared to the samples that also showed the metastable crystalline phase, but were only heat-treated. The preferred high conductivity thio-LISION III analog phase was precipitated from the mother glass when hot pressing between 170 and 250 °C and the lower conductivity Li_3PS_4 was observed when hot pressing at 300 °C. In DC cycling tests, the critical current density of 1 $mA \cdot cm^{-2}$ was obtained when hot pressing at 170 °C. It is believed that further atomic/microstructure optimization can improve the critical current density of LPS. Finally, the results of this study may contribute to the understanding of the metallic Li-solid-electrolyte DC electrochemical behavior to enable the development of all-solid batteries.

4.4 Experimental Details

4.4.1 Solid Electrolyte Synthesis

LPS 75-25 glass solid electrolyte was prepared through mechanochemical synthesis.[104] Starting with crystalline powders of Li_2S (99.98%, Aldrich) and P_2S_5 (99%, Sigma Aldrich), the precursors were mixed in an agate mortar and pestle and placed in a 45-cc zirconia pot with 10 zirconia balls of 10 mm in diameter and 10 zirconia balls of 5 mm in diameter. The pots were spun at 370 RPM for 20 h in a Planetary Micro Mill (Pulverisette 7, Fritsch GmbH), with 2-hour intervals of milling followed by 5-minute rest intervals at room temperature. The zirconia pots were sealed in a dry Ar-filled glove box (water concentration below 0.5 ppm), placed inside stainless steel vessels and transported in an inert atmosphere. The crystallization temperature was characterized using Differential Scanning Calorimetry (DSC). The milled LPS powders were sealed in aluminum hermetic pans in a glove box and transferred to the DSC (Q-100, TA instruments). The samples were heated under flowing nitrogen gas (50 ml·min^{-1}, ultrahigh purity, Airgas). The heating rate was 5 °C· min^{-1} within a temperature range from 40 °C to 300 °C for the LPS powder used for cold pressing, hot pressing and heat treatment. The DSC spectra to study the effect of heating rate on the crystallization temperature of LPS was collected at 0.7, 2 and 5 °C· min^{-1} within a temperature range from 40 °C to 300 °C.

4.4.2 LPS Densification Conditions

Milled LPS powder was cold-pressed (25 °C) and hot-pressed at 360 MPa and 47 MPa for 10 min and 4 h, respectively using a 12.7 mm diameter stainless steel die in a double-acting configuration to assure uniform pressure. 12.7 mm diameter graphite spacers (EDM-1, 01-402, Belmont) were placed above and below the LPS powder to attain a radially homogeneous heat distribution during hot pressing. Two layers of molybdenum foil (20 µm thick) were placed on each end between the powder and spacers to prevent direct contact between spacers and the powder. The powder was hot-pressed between 130 °C and 300 °C (LPS HP- 130 to LPS HP-300) across the glass transition and crystallization temperatures (determined by DSC) by resistive heating (AWH -051-040D, HTS Amptek) with a heating rate of 0.7 ± 0.1 °C·min^{-1}. Mica and quartz wool fiber were used to prevent heat losses during hot pressing. A LPS pellet was cold-pressed at 360 MPa for 10 min, and placed in a muffle furnace (KSL-1100X-S-UL, MTI Corporation) for heat treatment in an inert atmosphere at 170 °C for 4 h with a heating rate of 0.7 °C·min^{-1} (LPS HT-170). To serve as a baseline, one pellet was pressed at room temperature (LPS CP).

The density of the pellets was determined by geometrical measurements. The specimen thickness and diameter were measured by a digital caliper (500-196-20, Mitutoyo) in two places for each specimen and averaged. The relative density values were determined by dividing the bulk density by the theoretical density (1.88 g·cc^{-1} for a transparent LPS (3:1) glass prepared by hot pressing at 200 °C).[88] Nevertheless, we acknowledge that the theoretical density value of the samples that showed the presence of the metastable crystalline phase ($Li_{3.2}P_{0.96}S_4$) and stable crystalline phase (Li_3PS_4), would differ from the glass value. However, the volume fraction of each phase on all samples is unknown.

4.4.3 Materials Characterization

X-ray diffraction (XRD) measurements (CuKa 1.54 Å radiation, step size 0.1°, scan speed of 0.1° 2θ·min^{-1}) were performed using a diffractometer (Smartlab X-Ray diffractometer, Rigaku) to identify crystalline phases precipitated from the mother glass after hot pressing or heat treatment. The electrolyte pellets were manually ground in an agate mortar and pestle and then placed in an air-free holder with a Beryllium window (2455-SH-001, Rigaku) to perform the analysis. The thio-LISICON III XRD pattern adapted from Kanno et al.[59] was digitized by PlotDigitizer 2.6.6. The microstructures of the pellets were examined on fractured surfaces by using a field emission scanning electron microscope (JSM _7800F, JEOL). The pellets were sealed in an airtight sample holder in a dry Ar-filled glovebox and transferred for analysis. Raman spectra of the LPS pellets were collected using a Horiba instrument (LabRAM HR-800, Horibausing an Ar+ laser as exciting beam (532 nm), spot size of 50 mm. Samples were loaded in a quartz tube under a gas tight condition saturated with Argon. The spectra were recorded in the range of wavenumber between 100 cm^{-1} and 1500 cm^{-1}.

4.4.4 Electrochemical Characterization

Symmetric cells Li/LPS/Li (99.9% metals basis, 750 mm thick, 10769, Alfa Aesar) were assembled and aligned with a Teflon PTFE tube using nickel pins (99.98% purity, Goodfellow) as current collectors. Electrochemical impedance spectroscopy (EIS) and direct current (DC) measurements at room temperature under constant pressure (316 kPa) were carried out in a dry Ar-atmosphere using an impedance analyzer (VersaSTAT3, Princeton Applied Research and VMP-300, BioLogic Science Instruments), applying a perturbance amplitude of 20 mV in a frequency range of 7Mhz to 50mHz (20 points·decade^{-1}; 10 repetitions·frequency^{-1}). Preconditioning was performed applying a current density of 0.01 mA·cm^{-2} for 1 h in each direction for 10 cycles. The critical current density was determined by a DC asymmetric polarization method. A 0.01 mA·cm^{-2} current density was applied for 1 h in one direction, followed by a 0 V hold to re-equilibrate the cell to open circuit equilibrium conditions. The DC polarization and 0 V hold was followed by an alternating current (AC) impedance measurement to determine the impedance of the cell. After the AC measurement another 0 V hold for thirty minutes was used to re-equilibrate the cell. After the 0.01 mA·cm^{-2} hold, higher current densities were applied using the same sequence of 0 V hold and impedance measurements. The range of current densities was 0.01, 0.05, 0.1, 0.5 and 1.0 mA·cm^{-2}. Next, a 12 h DC asymmetric polarization was carried out at 1.0 mA·cm^{-2}.

CHAPTER 5 Correlating Macro and Atomic Structure with Elastic Properties and Ionic Transport of Glassy LPS 75-25 Solid Electrolyte

5.1 Introduction

The goal to achieve widespread adoption of EVs has accelerated the development of solid electrolytes for all-solid-state batteries (LMSSBs). [105] LMSSBs have garnered interest since they offer the potential for improved safety and energy density compared to Li-ion batteries. To realize these advantages, the non-flammable solid electrolyte would replace the flammable liquid electrolyte and Li metal would replace carbon anodes to reduce cell volume and weight. [27] As a result, about 100 % higher energy densities could be achieved compared to conventional Li-ion batteries. [7,8] Sulfide-based electrolytes with adequate ionic conductivity, low interfacial resistance against electrodes and low processing cost make them one of the most promising inorganic solid electrolyte materials that could enable LMSSBs.[31] However, despite the development of different compositions through different synthesis techniques in the LPS family [106–110], the successful transition to Li metal with relevant charging rates (≥ 3 mA·cm^{-2} at room temperature) has not been realized.

It has been reported that microstructural defects such as grain boundaries and/or pores can play a role in determining the maximum charging rate (or critical current density, CCD) a solid electrolyte can withstand without Li penetration. [15,16] Thus, a glassy, dense microstructure may be preferred for LMSSB applications. In previous work (Chapter 1), [19] the densification behavior or LPS 75-25 was studied as a function of temperature (25 to 300 °C) at fixed pressure (47 MPa). It was determined that crystallization of the thio-LiSICON III analog phase occurred between 170 °C and 250 °C. Moreover, the relative density was more or less invariant of densification temperature (~80 % RD; calculated dividing the geometrical density by its theoretical density in the amorphous phase: 1.88 $g \cdot cm^{-3}$).[88] While in our previous study the maximum hot-pressing pressure (47 MPa) was limited by the mechanical integrity of the molding die, we recently developed capabilities to increase pressure to achieve 360 MPa. With this new capability, the current study compliments our previous study by investigating the densification behavior of LPS 75-25 as a function of pressure at fixed temperature. The pressure ranged between 47 up to 360 MPa and the temperature was fixed at the glass transition temperature (T_{glass}). We hypothesize that by increasing the molding pressure the relative density will increase. Furthermore, the simultaneous application of pressure at T_{glass} during processing will dramatically reduce the elastic modulus, thereby increasing flow to facilitate densification. It will be shown that the samples obtained through this processing approach indeed have relative densities up to 98 % and that significant enhancement to the ionic conductivity and an increase in elastic modulus were observed. We believe the outcomes of this study can provide mechanistic insight into processing-structure-property relationships to improve the feasibility of LPS-based solid-state battery technology.

5.2 Results and Discussion

5.2.1 Materials Characterization

5.2.1.1 Effect of processing temperature on LPS 75-25 densification

Typically, DSC is used to measure T_{glass}; however, TMA was used because DSC relies on measuring changes in heat capacity and the change in heat capacity associated for LPS during this transition is not sufficient to determine T_{glass}. TMA measures the change in dimensions as a function of temperature to determine the transition from a vitreous solid to an amorphous liquid. The dimension change vs temperature and corresponding derivative data for a cold pressed LPS 75-25 pellet are shown in Figure 5.1. The T_{glass} is more precisely described as a transformation range [111] , thus, it was determined that the onset for this transformation started at 200.0 ± 0.1 °C with and upper limit at 213.6 ± 0.1 °C. The largest change in dimension occurred at 204.6 ± 0.1 °C as observed from the derivative dimension change trace in Figure 5.1a. A heating rate of 0.7 $^{o}C.min^{-1}$ was used to measure T_{glass} to match the heating rate used during the densification in this study. The T_{glass} is similar, but lower compared to the T_{glass} of 220 ^{o}C for LPS 70-30 measured by Minami et al. and Tatsumisago et al.[108,112]. This difference is attributed to the difference in composition, but mainly to the higher heating rate used. Both Minami et al. and Tatsumisago et al. used a heating rate of 10 °C min^{-1}, compared to 0.7 °C min^{-1} for this study. Since T_{glass} refers to a structural relaxation transition, it depends on kinetic factors as proposed by the Bartenev-Ritland equation. [111] The structural relaxation time is inversely proportional to the cooling/heating rate. Thus, LPS 75-25 with a slower heating rate than 70-30 will exhibit the structural relaxation sooner (lower temperature) than the 70-30 LPS with a faster heating rate. More importantly, for processing purposes, a slower heating rate allows sufficient time for atoms to rearrange resulting in a denser glass. [68]

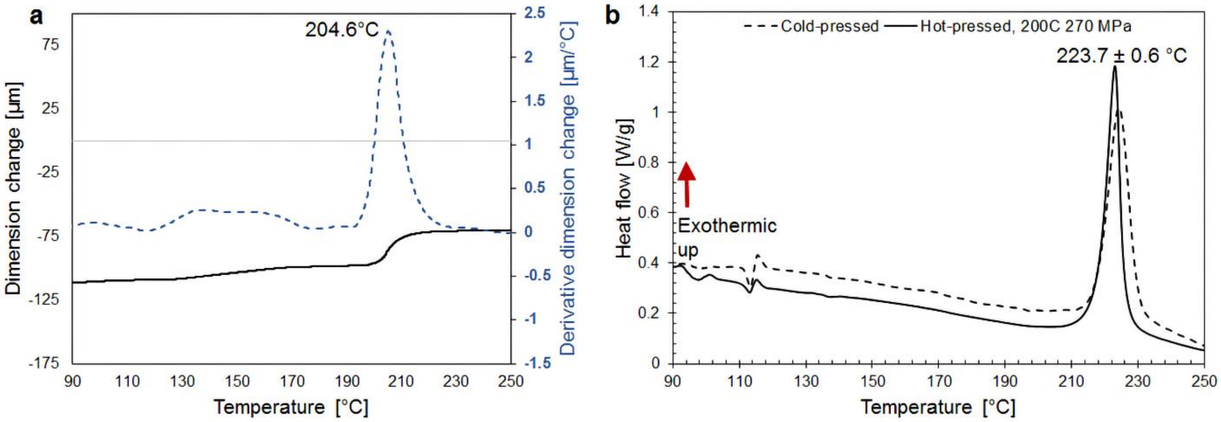

Figure 5.1 *Measurement of glass transition and crystallization temperature for LPS 75-25 via (a) thermomechanical analysis (TMA) and (b) Differential Scanning calorimetry (DSC), respectively. Heating rate on both tests was 0.7 °C min*$^{-1}$*, same used for densification.*

$T_{crystallization}$ was measured using DSC (Figure 5.1b) heating at 0.7°C min^{-1} for cold pressed (360 MPa) and hot-pressed (200°C, 270 MPa). Again, 0.7°C min^{-1} was used to match the heating rate during densification. For both samples, $T_{crystallization}$ was determined to be 223.7±0.6°C, which is in excellent agreement with previous work.[19] Subtle endotherms/exotherms were observed at approximately 100 ^{o}C in both samples and are believed to be associated with traces of moisture in the purging gas, since according to specifications, still contains < 5 ppm of moisture. This is believed to be the case rather than resulting from moisture in the sample/pan given that hermetic pans were used and sealed in a dry (<0.5 ppm H_2O) Ar glovebox in addition to storing the pans in a vacuum oven at 120 ^{o}C. The heat capacity at constant pressure showed no appreciable change after hot-pressing at 200 ^{o}C, 270 MPa, confirming that no or negligible crystallization occurred. Nevertheless, there was a 23% decrease in the latent heat of crystallization after hot-pressing (85.35 J g^{-1}, Figure 5.2), suggesting that hot-pressing while maintaining the amorphous phase results in a slightly more thermodynamically stable structure compared to the amorphous cold-pressed LPS given that the calculated latent heat of crystallization was normalized by mass. From Figure 5.1, several observations can be made. First, TMA determined that the T_{glass} was between

200.0 ± 0.1 °C and 213.6 ± 0.1 C °C. Thus, to increase flow during densification, by heating above T_{glass}, the temperature selected was 200 °C and used throughout this study for all hot-pressed samples. Whereas in our previous study, hot pressing was conducted at 130, 150, 170, 190, 250 and 300 °C at a fixed pressure of 47 MPa, thereby excluding the temperature range between T_{glass} and $T_{crystallization}$. [19] Second, DSC determined that the $T_{crystallization}$ was 223.7±0.6 °C and did not change after hot-pressing at 270 MPa and 200 °C. This confirms that hot-pressing LPS at 270 MPa and 200 °C did not cause crystallization. Taken together, the TMA and DSC analyses determined the upper ($T_{crystallization}$) and lower (T_{glass}) bound temperatures for processing. By hot-pressing between these salient temperatures, we believed significantly higher densities can be achieved. Moreover, it was found that hot-pressing in this temperature regime, and at higher pressures compared to the previous study, [19] had beneficial and unexpected consequences to the atomic packing factor and the physical and electrical properties.

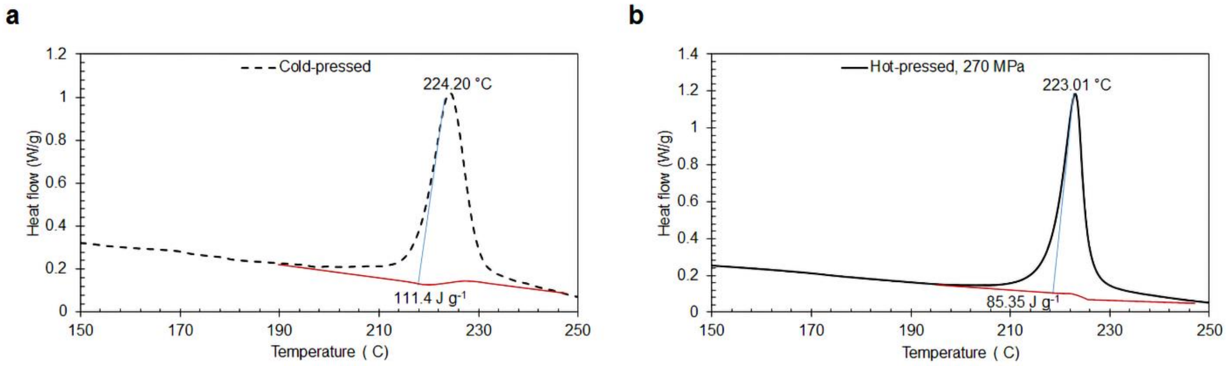

Figure 5.2 *LPS 75-25 latent heat of crystallization of a (a) cold-pressed sample (b) hot-pressed sample at 270 MPa 200°C*

5.2.1.2 Microstructural Analysis

On the previous chapter it was reported that the LPS geometric density values, and consequently, its relative density (RD) values were invariant to processing temperature from 130-

300 °C at fixed pressure (47 MPa). [19] The lack of densification is believed to be attributed to the lack of viscous flow, yielding samples with ~80% RD compared to its theorical density in the amorphous phase (1.88 g cm^{-3}),[88] regardless of the hot-pressing temperature. In this study, dramatically different densification is observed (Figure 5.3). The RD clearly increases with increasing pressure (at the fixed temperature of 200 °C). Pressing at room temperature, or cold-pressing, at 360 MPa achieves 89 ± 2% RD, which is consistent with the theoretical calculations conducted in this study (discussed in the next section), in addition with other reports in literature. [88,89] This represents a 3% increase in mean RD compared to our previous study (86 ± 2% RD). [19] However, the changes observed are within the detection limits of the instrument. For all other samples the hot-pressing temperature was 200 °C. At 47 and 90 MPa, the RD were 91 ± 2% and 92 ± 2%, respectively. It was at pressures of 180 MPa and above that a significant increase in RD was achieved and noticeable change in microstructure (fracture surfaces) was observed. For example, hot-pressing at 47 and 90 MPa produced microstructures consisting of discernable particle boundaries and porosity (Figure 5.3). In comparison, when pressing at 180 MPa, the particle boundaries are more-or-less absent and the fraction and size of the porosity is noticeably lower. Increasing from 90 to 180 MPa also resulted in the largest increase in RD (~ 4%) compared to the other increments in pressure from 180 to 270 and 270 to 360 MPa. Furthermore, the fracture surfaces of samples hot-pressed at and above 270 MPa are consistent with a glassy fracture with no evidence of particle boundaries and negligible porosity. From the relative density and fracture surface analysis, it is believed that the decrease in porosity and lack of discernable particle boundaries or glassy fracture surfaces, suggests that hot-pressing at T_{glass} and at pressures > ~180 MPa produces a microstructure resembling a typical melt processed glass. However, to confirm

that crystallization on the macroscopic scale did not occur along with densification, X-Ray diffraction was conducted.

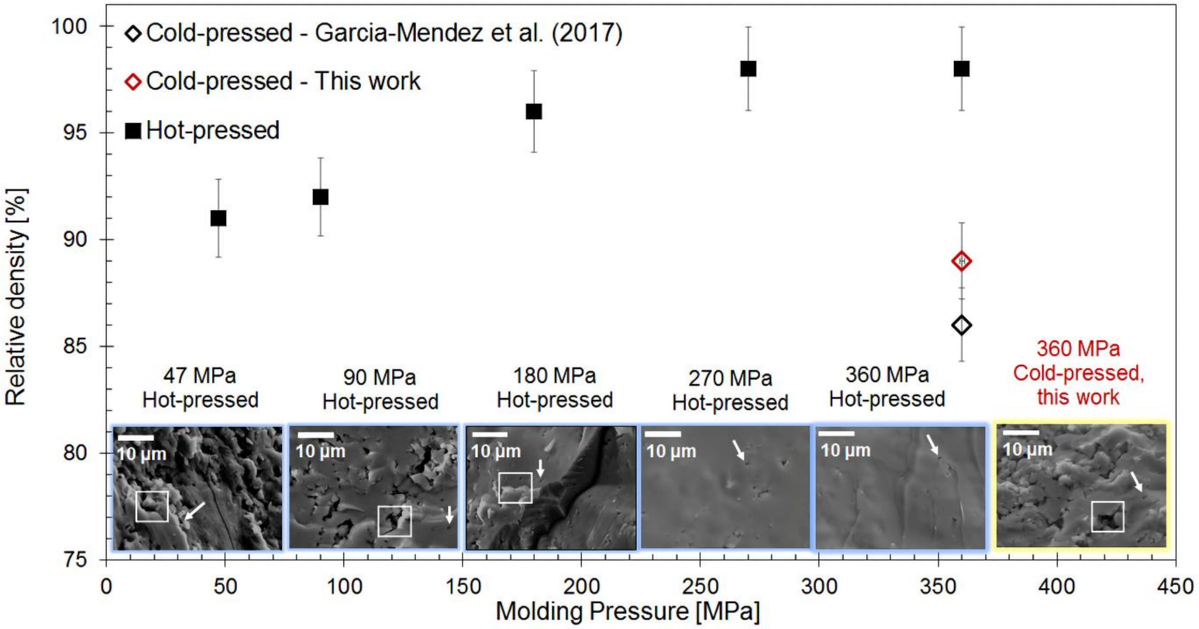

Figure 5.3 *Relative density as a function of molding pressure of LPS 75-25 with a theoretical density of 1.88 g·cm^{-3}. Fracture surfaces and density measurements of LPS 75-25. Insets of Secondary Electron Microscope (SEM) images correspond to fracture surfaces with particle boundaries and porosity highlighted using white boxes and arrows, respectively.*

5.2.1.3 Suppression of heterogeneous nucleation

To determine if crystallization occurred during densification at 200 °C between 47 and 360 MPa X-Ray diffraction was conducted (Figure 5.4). With the exception of the sample pressed at 47 MPa, all samples lacked evidence of crystallinity and resembled the diffraction pattern of cold-pressed LPS. As the molding pressure for hot-pressing decreased from 360 to 47 MPa, gradual intensification of diffraction peaks in the X-Ray spectrum corresponding with the crystallization of the thio-LISICON III analog was evident.[59] This metastable crystalline phase was also observed in our previous work where precipitation from the mother glass was seen in LPS hot-pressed between 170 – 250 °C at 47 MPa. [19] The samples obtained were glass-ceramics under those processing conditions. The presence of crystalline phases below the glass transition and crystallization temperature was unexpected since the T_{glass} corresponds to the transition in which atoms rearrange starting as a vitreous solid transforming into an amorphous liquid followed by crystallization. As explained by nucleation and growth theory, the crystallization process of glassy materials consists of nucleation and crystal growth stages. [68] Typically, the formation of nuclei is around the onset of the $T_{crystallization}$ followed grain growth; however, pores and free surfaces can act as heterogeneous nucleation sites favoring crystal growth. [68] These regions could act as preferred nucleation sites since they have higher free energy, thus, facilitating nucleation and growth of the crystalline phase. Indeed, the samples that showed the presence of the thio-LISICON III analog crystalline phase had a high-volume fraction of porosity (9 – 20%) and free surfaces, both acting as heterogeneous nucleation sites favoring crystal growth. This was also manifested indirectly on the higher latent heat of crystallization measured by DSC on the cold-pressed sample compared to the 98% dense hot-pressed sample at 200 °C, 270 MPa (Figure 5.2). We believe that the lack of pores or free surfaces on the near to theoretical density samples reduces strain energy that suppresses the nucleation or growth of the crystalline or metastable crystalline phases. In agreement, the samples that exhibited RD $\geq$ 98%, showed little to no metastable crystalline phase based on the X-Ray diffraction measurements. In addition, the thermodynamic barrier to nucleation is suppressed as the contact angle between the crystalline nuclei and the amorphous phase decreases. [68] We believe the higher the degree of densification, the lower the contact angle is obtained between the crystalline nuclei and amorphous phase suppressing crystallization. From the X-Ray diffraction pattern, the broad peak observed on the sample hot-pressed at 270 MPa along with the crystallization peak observed from DSC at 223.7±0.6 °C, corroborates that a glassy sample can be attained by hot-pressing at 200 °C.

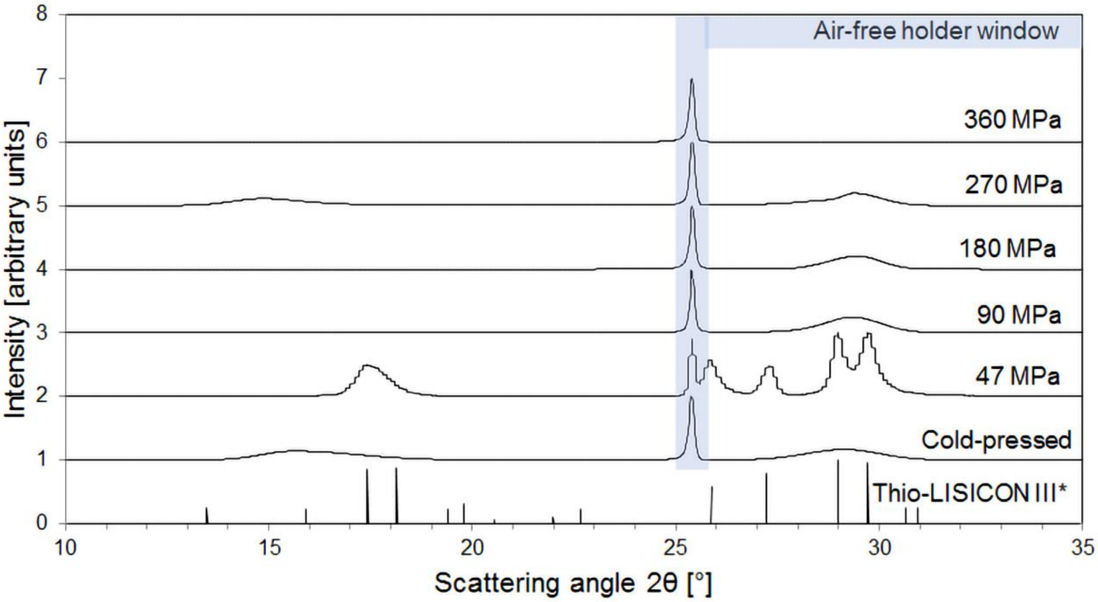

Figure 5.4 *X-Ray Diffraction patterns of LPS 75-25 as a function of molding pressure. The thio-LISICON III X-Ray Diffraction pattern was adapted from Kanno et al.*[59]

5.2.2 Mechanical properties

The elastic constants and hardness were measured using a combination of ultrasonic velocity measurements and nanoindentation experiments (Figure 5.5). Both techniques were used to probe the LPS mechanical properties at different length scales; the ultrasonic velocity measurements to acquire bulk properties and nanoindentation for localized, single-particle properties. Longitudinal and shear wave speeds were used to determine the Young's (E) and Shear (G) Moduli using equations 5.2 and 5.3 (see experimental section).

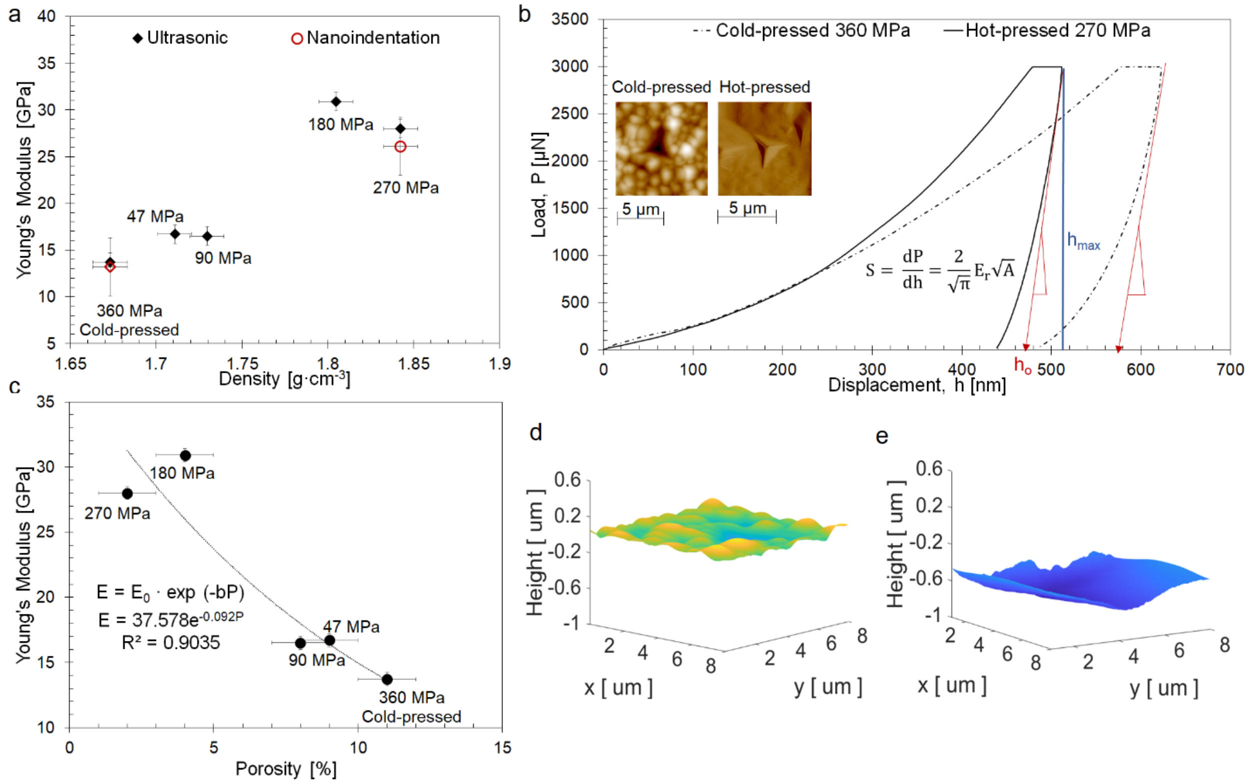

Figure 5.5 *Elastic and plastic behavior of LPS 75-25. Young's Moduli of LPS 75-25 as a function of molding pressure via ultrasonic velocity measurements and nanoindentation (a and b). Inset in b shows the Atomic Force Microscope (AFM) 2D images acquired from cold-pressed and hot-pressed LPS at 270 MPa 200 °C. (c) Young's Moduli as a function of porosity where* E_0 *denotes the Young's Modulus at 0 porosity, P the volume fraction of porosity and b is a dimensionless constant. LPS Atomic Force Microscopy (AFM) 3D maps of (d) cold-pressed sample and (e) hot-pressed sample at 270 MPa, 200°C*

The *E* of cold-pressed LPS at 360 MPa was measured to be 13.7 ± 1.3 GPa, in agreement with Sakuda et al. measurements. [89] As expected, this value is much lower than the *E* reported for Li-ion conducting oxide glasses, such as Li_2O-P_2O_5 50-50, with an *E* of 39.6 GPa. [113] This value would be anticipated to be even higher for a 75-25 composition as observed with sulfide glasses as the glass modifier concentration is increased. [114] The higher moduli observed in oxide glasses compared to sulfide glasses lies in the higher bonding dissociation energies resulting in a more rigid glass network (P-S: 442 kJ mol^{-1}, Li-S: 313 kJ mol^{-1}, P-O: 589 kJ mol^{-1}, Li-O: 341 kJ mol^{-1}), in addition to a higher packing density. [115]

Despite using lower pressure compared to what is typically used for cold-pressing (e.g. 360 MPa), Hot-pressing LPS at 200 ^{o}C at 47 and 90 MPa, resulted in a greater E (16.7 ± 0.6 and 16.5 ± 0.5 GPa, respectively) compared to the cold-pressed pellet (13.2 ± 0.95 GPa). We believe this is a consequence of increasing viscous flow that results from heating at T_{glass}, which lowers the volume fraction of porosity as shown via electron microscopy and density measurements in the previous section. This behavior is consistent with the exponential relationship between E and the volume fraction of porosity reported by Rice *et al*. [116] (Figure 5.5c). The increase in E is believed to be a result of the change in volume fraction of porosity of 3-4 % compared to the cold-pressed sample rather than the presence of the metastable crystalline phase detected via XRD for the sample hot-pressed at 47 MPa. The presence of the thio-LISICON III analog phase is not believed to correlate with the increase in E given that the difference in E for both hot-pressed samples is negligible and the change in density between both samples was only of 1%. Additionally, crystalline phases in the LPS system would be expected to exhibit higher E values compared to the amorphous phase as demonstrated later in the calculated elastic properties. This suggests that the volume fraction of metastable crystalline phase is not sufficient to increase E to a higher extent than the reduction in volume fraction of porosity (Table 5.1). In other words, the volume fraction of metastable crystalline phase is not sufficient to increase E or G at the bulk scale as it was reflected from the time of flight measured for the longitudinal and shear waves for both samples during ultrasonic velocity measurements.

Hot-pressing LPS from 90 to 180 MPa led to a significant increase in Young's Modulus, *E*, reaching 30.9 ± 0.5 GPa. This change in elastic properties agrees well with the above finding that particle boundaries and porosity decreased considerably by hot-pressing at and above 180 MPa, as observed in the SEM fractographs (Figure 5.3). However, a decrease in the volume fraction of porosity alone cannot completely explain the increase in *E* (as it is also evident from the exponential fit shown in Figure 5.5c). We believe the slight deviation from the expected exponential relationship is attributed to changes on the intramolecular level (intermediate-range order) for the samples hot-pressed $\geq$ 180 MPa. It is known that more interconnected molecular organizations, such as a 3D network, can lead to a significant increase in *E*. [117] Thus, to evaluate the local coordination of these disordered materials, pair distribution functions (PDF) were collected via neutron diffraction (Figure 5.8c). In the case of glasses with covalently bonded elements, the mean coordination number can be used to correlate physical properties to structural changes. A higher mean coordination number would correspond to a more interconnected molecular organization resulting in a higher *E*. [117] From the spectra collected, it was observed that the sample hot-pressed at 270 MPa, *E* of 28.0 ± 0.6 GPa, showed a ~20% increase in peak intensity compared to the sample hot-pressed at 47 and 90 MPa (*E* of 16.7 ± 0.6 and 16.5 ± 0.5 GPa, respectively), mostly on the Li-S pairs. This increase is closely related to the change in the coordination environment of the Li ions, [118] but more importantly, suggesting a more interconnected arrangement between Li and S for the samples hot-pressed at 180 and 270 MPa resulting in larger elastic constants.

A slight decrease in *E* was observed for the LPS hot-pressed at 270 MPa (28.0 ± 0.6 GPa) and the sample hot-pressed at 360 MPa was not sufficiently strong to withstand handling and fractured upon instrumentation. Residual stress in uniaxially hot-pressed materials are known to occur due to differences in thermal expansion coefficients between the molding die and the powder, frictional forces between the wall of the die, and the extraction process. [119] It is for these reasons that we believe the samples hot-pressed at 270 and 360 MPa are the most likely to have the highest residual stress among all samples. Anecdotally, the samples hot pressed at 270 and 360 MPa were relatively weak and brittle, consistent with the presence of residual stress. Thus, the slight decrease in *E* (2 GPa), by increasing the hot-pressing pressure from 180 to 270 MPa, is attributed to the presence of microcracks that attenuated the acoustic wave speed. Similar behavior is observed for the Shear modulus (Figure 5.6), which is expected since glasses are generally elastically isotropic. To minimize the impact that particle boundaries and porosity may have on the measurement of *E,* nanoindentation was conducted. The *E* values obtained via nanoindentation for the cold-pressed sample and hot-pressed at 270 MPa (13.2 ± 1.0 GPa and 26.1 ± 3.1 GPa, respectively, load vs displacement curves shown in Figure 5.5b) are in good agreement with the bulk-type measurements (13.7 ± 1.3 GPa and 28.0 ± 0.6 GPa, respectively). These data further suggest that the changes in elastic properties measured were related to atomic/molecular changes rather than just changes in porosity alone. The slight reduction in *E* from nanoindentation for the hot-pressed sample at 270 MPa could be due to the localized nature of the measurements that could have included some indentations that were close to microcracks, thus reducing those particular *E* values. The Hardness H values determined via nanoindentation for the cold-pressed and hot-pressed at 270 MPa showed the behavior expected for reduced volume fraction porosity; an increase in hardness, going from 0.29 ± 0.04 GPa to 0.65 ± 0.07 GPa (89 to 98% relative density) as shown in Figure 5.6. The corresponding shear moduli for all samples including the RMS roughness measured via AFM for the cold-pressed and hot-pressed at 270 MPa 200°C are listed in Table 5.5.

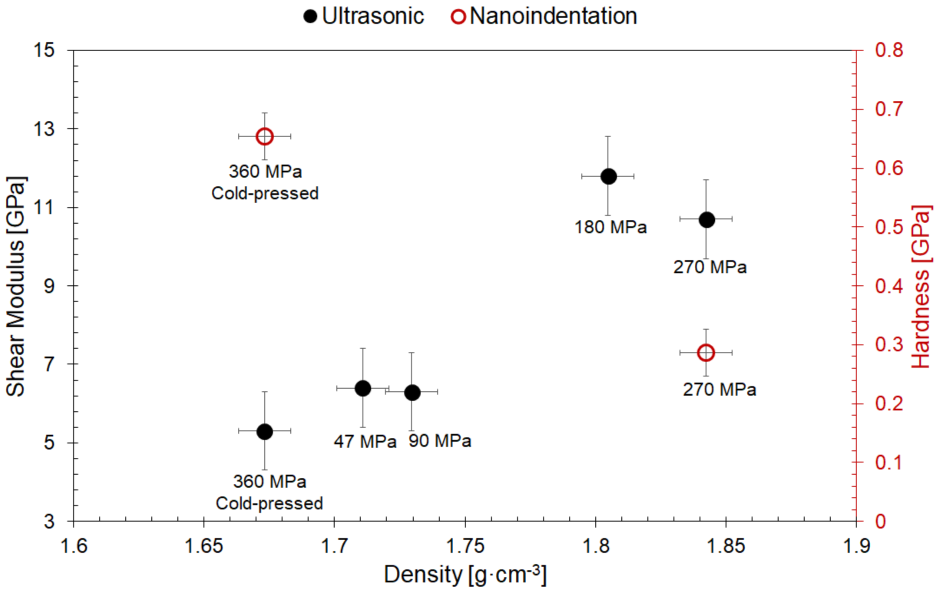

Figure 5.6 *Shear Moduli of LPS 75-25 as a function of molding pressure via ultrasonic velocity measurements and Hardness values measured via nanoindentation*

The calculated elastic coefficients, and moduli of LPS 75-25 as a function of density are shown in Table 5.1. The density of the melt quenched to 300 K under atmospheric pressure was 1.55 g cm^{-3}; Sakuda et al. measured a cold pressed density of 1.45 g cm^{-3} at 180 MPa. [89] Hydrostatic pressure applied at 360 MPa during AIMD resulted in a higher density of 1.65 g cm^{-3}, which is in good agreement with the density of the cold-pressed samples reported here at 360 MPa (1.67 g cm^{-3}, see Table 5.5). Increasing the hydrostatic pressure from 0.1 MPa to 360 MPa within the simulation increased all of the bulk, shear and E, from 9.8 to 14.3 GPa, 5.1 to 6.8 GPa and 13.0 to 17.5 GPa, respectively. Further increasing the density to 1.76 g·cm^{-3} (corresponding to P = 1 GPa) yielded insignificant changes to the shear and E. This density lies within the density experimental values of the samples hot-pressed at 90 and 180 MPa (1.73 and 1.80 g·cm^{-3}, respectively), where the significant increase in E was also observed. The calculated elastic moduli of the glass for the densities of 1.67-1.76 g·cm^{-3} are consistent with the measured values in this work (Table 5.5) and those of Sakuda et al. [89] At these densities, the calculated bulk, shear and E are approximately half the moduli of the related crystalline phases, α- and β-Li_3PS_4, and of $Li_7P_3S_{11}$. (The former phases include an ordered arrangement of PS_4 anions; $Li_7P_3S_{11}$ includes both PS_4 and P_2S_7 anions.) Finally, calculations performed at the highest density investigated, 2.42 g·cm^{-3}, (corresponding to P =10 GPa) resulted in moduli that exceed those of the crystalline materials.

	ρ (g·cm^{-3})	B (GPa)	G (GPa)	E (GPa)	ν	C_{ij}					
glass-Li_3PS_4	1.55	9.82	5.10	13.04	0.28	12.7	6.4	6.8	0.4	0.0	-1.5
						6.4	15.7	7.3	1.7	-1.0	-0.9
						6.8	7.3	19.7	0.8	-1.2	0.1
						0.4	1.7	-1.2	5.5	0.4	-0.3
						0.0	-1.0	-1.2	0.4	5.8	0.4
						-1.5	-0.9	0.1	-0.3	0.4	6.2
	1.65	14.26	6.75	17.49	0.30	20.6	9.7	9.8	-0.4	-0.2	-0.5
						9.7	25.2	10.0	1.3	-0.1	-0.9
						9.8	10.0	24.1	0.4	0.2	-0.3
						-0.4	1.3	0.2	7.4	-0.6	0.0
						-0.2	-0.1	0.2	-0.6	6.6	0.3
						-0.5	-0.9	-0.3	0.0	0.3	6.8
	1.76	16.93	6.61	17.54	0.33	24.4	12.0	13.4	-1.3	-0.1	0.7
						12.0	26.8	12.0	-0.8	0.1	2.0
						13.4	12.0	27.7	1.1	-3.5	0.6
						-1.3	-0.8	-3.5	8.3	-0.7	0.9
						-0.1	0.1	-3.5	-0.7	7.2	-0.2
						0.7	2.0	0.6	0.9	-0.2	5.1
	2.42	50.70	16.27	44.10	0.36	71.8	37.2	41.7	-0.5	-0.2	-0.3
						37.2	71.5	41.2	-1.3	0.7	-0.1
						41.7	41.2	71.0	0.5	6.1	1.8

						-0.5	-1.3	6.1	18.9	0.3	-0.1
						-0.2	0.7	6.1	0.3	17.6	-0.4
						-0.3	-0.1	1.8	-0.1	-0.4	14.4
γ-Li_3PS_4	1.87	31.90	13.02	34.40	0.32						
β-Li_3PS_4	1.80	21.72	11.14	28.55	0.28						
$Li_7P_3S_{11}$	1.80	23.43	9.32	24.69	0.32						

Table 5.1 *Calculated elastic properties of Li_3PS_4 glass and for related crystalline materials (γ-Li_3PS_4, β-Li_3PS_4, and $Li_7P_3S_{11}$) as a function of density, ρ. The elastic constants C_{ij}, bulk modulus B, shear modulus G, and Young's modulus E have units of GPa.*

Additionally, topographic maps were acquired via atomic force microscopy (AFM) of the cold-pressed sample and hot-pressed sample at 200 °C and 270 MPa (Figure 5.5 d and e, respectively). The lack of discernable particles within the microstructure for the hot-pressed sample is in agreement that a glassy material was obtained, resembling a melt-processed glass. Furthermore, the cold-pressed sample map still shows discernable particles within the microstructure as expected, shown as peaks and valleys. Although the RMS roughness values measured for each did not vary significantly (30.03 ± 1.24 for the cold-pressed sample and 35.03 ± 13.20 for the hot-pressed sample), the peaks and valleys found in the hot-pressed sample are taller and deeper than the cold-pressed sample. Also, the distance that separates each peak is larger for the hot-pressed sample. The repercussions to this during cell assembly need to be considered. It is known that Li metal exhibits significant creep at room temperature, [120,121] thus, load above the yield strength of Li [122] can facilitate contact between electrode and electrolyte as it can be observed in Figure 5.7 for all samples when assembling Li | LPS | Li symmetric cells. Therefore, the values selected when measuring ionic conductivity on the following section were taken when the areal specific resistance for the bulk contribution did not show considerable change as a function of cell stack pressure. Ionic measurements were carried out to further investigate the relationship between structure and properties in this thiophosphate solid electrolyte.

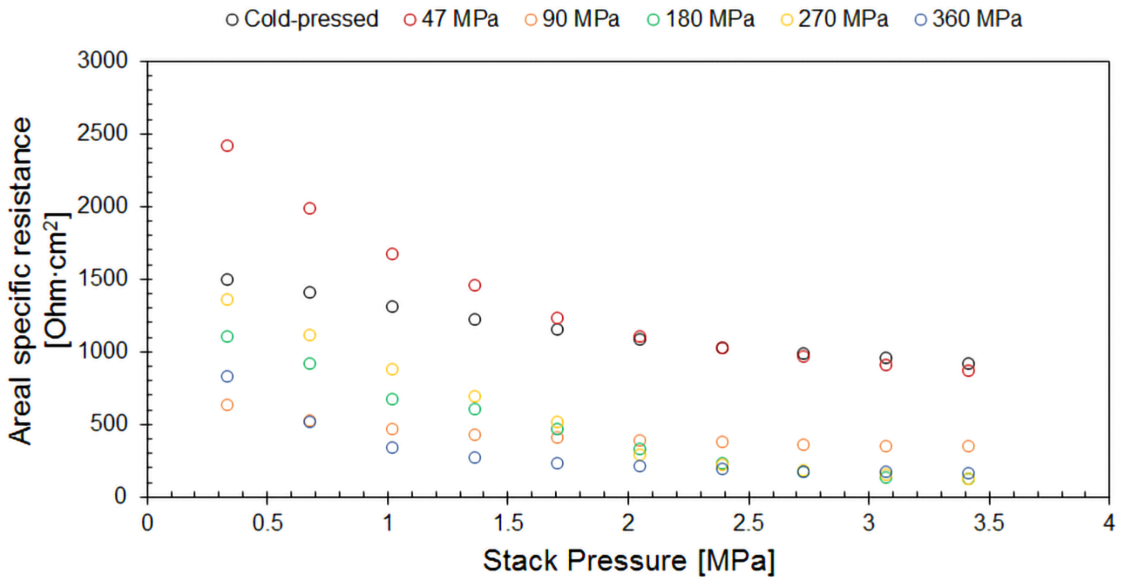

Figure 5.7 *Effect of cell stack pressure on areal specific resistance for the bulk contribution in LPS 75-25 at room temperature*

5.2.3 Lithium ionic transport

The electrochemical impedance spectroscopy (EIS) spectra collected (Figure 5.8a) showed that the LPS cold-pressed (360 MPa) exhibits a room temperature ionic conductivity of 0.2 mS cm^{-1}, which is in good agreement with the values reported previously. [58,104] When hot-pressing the sample at 200 °C and 47 MPa resulting in a glass-ceramic, the ionic conductivity slightly increased to 0.3 mS cm^{-1}. This is expected with the presence of the thio-LISICON III analog phase detected via XRD measurements, since it has been reported to have a slightly higher ionic conductivity of 0.64 mS cm^{-1} at room temperature [58] enhancing the overall ionic transport within the glass-ceramic electrolyte. It has been seen that the ionic conductivity in Li thiophosphate materials depends not only on their structural order (crystalline vs. amorphous), but also on the crystalline phase(s) that precipitate from the mother glass. [58,62,104,112] In the case of the amorphous LPS 75-25, an ionic conductivity of 0.32 mS·cm^{-1} at room temperature has been reported[58] and upon heating (up to 250 °C), conductivities slightly higher, still on the 0.1 mS·cm^{-1} range, have been observed due to the precipitation of the thio-LISICON III analog ($Li_{3.2}P_{0.96}S_4$) metastable crystalline phase. [19] This phase is not thermodynamically stable since upon further heating evolves into other crystalline phases such as ɣ-Li_3PS_4, β- Li_3PS_4 and $Li_4P_2S_6$, all with a lower room temperature conductivity in the order of 1x10^{-3} mS·cm^{-1}. [65,123]

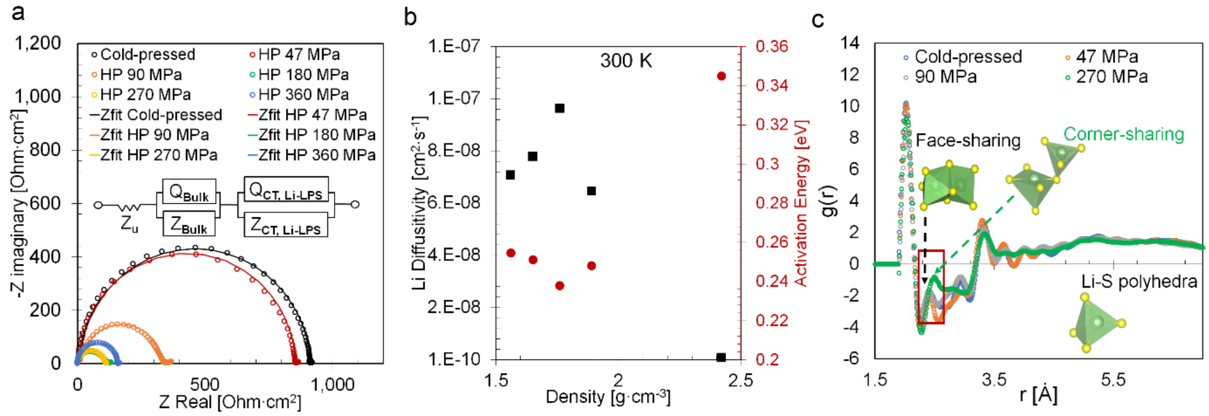

Figure 5.8 *Measured and calculated ionic transport of LPS 75-25 (a) Electrochemical Impedance Spectroscopy (EIS) spectra of Li-LPS-Li cells at room temperature with their corresponding fit (b) Calculated Li self-diffusivity at 300K and activation energy as a function of density. (c) Pair distribution functions g(r) of LPS 75-25 obtained via time-of flight neutron diffraction for all samples processed at different molding pressures showing a shift on the Li-S pair for a corner-sharing configuration on the sample hot-pressed at 270MPa*

Parameter	**Cold-pressed**	**Hot-pressed, 47 MPa**	**Hot-pressed, 90MPa**	**Hot-pressed, 180 MPa**	**Hot-pressed, 270 MPa**	**Hot-pressed, 360 MPa**
Z_u, [Ohm·cm^2]	6.8	3.5	10.1	0.4	0.5	0.4
Q_{Bulk}, [F]	2.8×10^{-9}	2.4×10^{-9}	3.3×10^{-9}	2.0×10^{-9}	0.94×10^{-9}	0.93×10^{-9}
α_{Bulk}	0.96	0.98	0.95	0.85	0.91	0.98
Z_{Bulk}, [Ohm·cm^2]	907.9	852.1	326.7	112.6	109.3	158.3
$Q_{CT,\ Li\text{-}LPS}$, [F]	3.8×10^{-3}	1.8×10^{-3}	3.0×10^{-3}	4.1×10^{-3}	1.2×10^{-3}	6.2×10^{-3}
$\alpha_{CT,\ Li\text{-}LPS}$	0.90	0.97	0.82	0.95	0.94	0.87
$Z_{CT,\ Li\text{-}LPS}$, [Ohm·cm^2]	9	12.6	21.5	9.5	4.8	4.0

Table 5.2 *Electrochemical impedance spectroscopy analysis of LPS processed at different molding* pressures. *The α-values account for deviation from the ideal pure capacitor behavior (α = 1)*[124]

From Figure 5.8a it can be observed that the room temperature ionic conductivity of LPS 75-25 increased from 0.3 mS·cm^{-1} to 1.1 mS·cm^{-1} when hot-pressing from 47 MPa to 270 MPa (1.71 to 1.84 g·cm^{-3}), and a slight decrease to 0.8 mS·cm^{-1} when hot-pressing at 360 MPa (1.86 g·cm^{-3}). To explain the changes observed, the impact of densification on the internal volume (void space) available for Li motion and Li diffusivity was quantified. Moreover, the anionic building units were identified via Raman since it is known that Li is dynamically coupled to the reorientation and thermal vibration of the local anionic building units in thiophosphate glasses. [125]The Raman spectra (Figure 5.9) showed *ortho*-thiophosphate species (PS_4^{3-}) as the dominant species at 421 ± 1 cm^{-1}, known to be responsible for the high ionic conductivity in Li thiophosphate glasses [126]. In addition, *hypo*-thiophosphate species ($P_2S_6^{4-}$) at around 380 cm^{-1} were detected, in agreement with Dietrich et al. for this composition. [126] The intensity of both signals were independent from the densification conditions, therefore, the concentration of PS_4^{3-} and $P_2S_6^{4-}$ are believed to be the same among all samples. Consequently, the fraction of anion polymorphs are not responsible for the changes in ionic transport observed in this study.

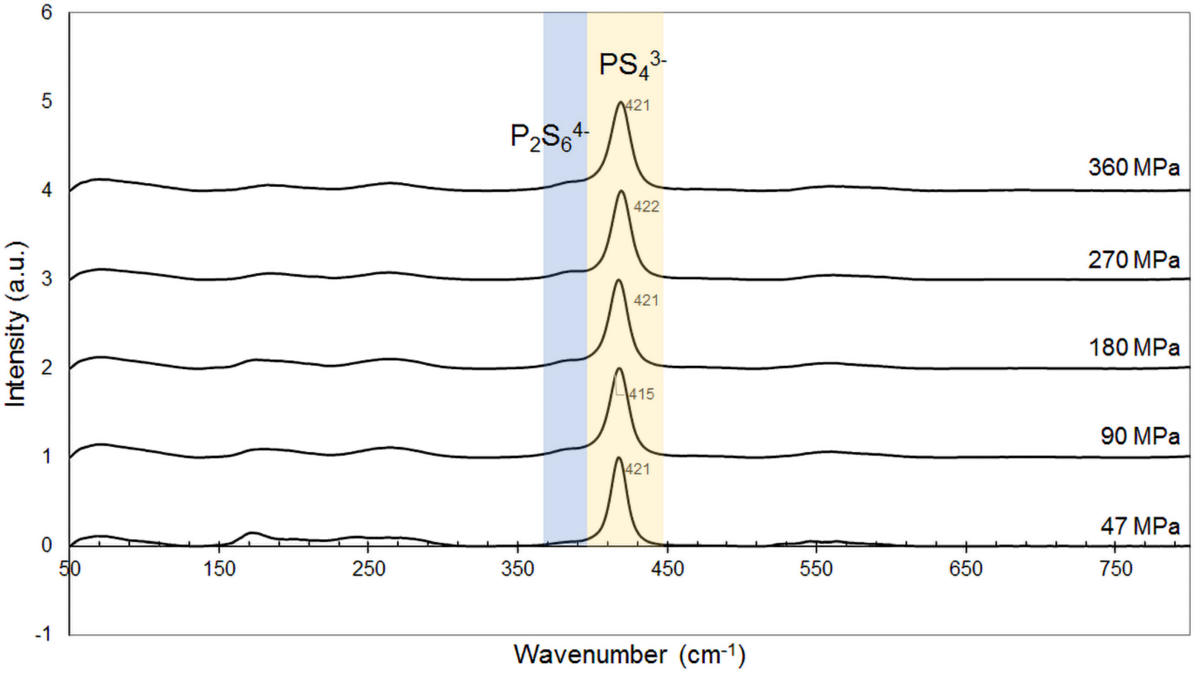

Figure 5.9 *Raman spectra on LPS 75-25 samples processed at different molding pressures*

Regarding the volume available for Li migration, Figure 5.10 plots the relationship between the glass density and the characteristic dimensions for the channels (i.e., void space) available for Li migration within the glass. Earlier studies of ion migration in solids have shown that the size of the migration channel strongly correlates with ion mobility.[127] For example, Ichihashi et al.[127] have shown that ion migration is facilitated when the channel diameter is neither too small – a narrow bottleneck tends to block migration – nor too large. (In the latter case the mobile species migrates along the pore surface.) Using the crystallographic topology analysis routines implemented in the Zeo++ code, Figure 5.10 demonstrates that, as expected, the diameters of both the largest included sphere (D_i) and the largest included sphere along the free sphere path (D_{if}) monotonically decrease with increasing density. (D_i describes the diameter of the largest pore found anywhere within the glass model, while D_{if} refers to the largest diameter along a channel that permeates the entire system, and which is everywhere large enough to accommodate Li+ migration.) From Figure 5.8b, the activation energy and diffusivity of Li are predicted to be minimized and maximized, respectively, for a density of 1.75 $g \cdot cm^{-3}$. The void space analysis in Figure 5.10 shows that at this density, $D_i = D_{if} = 3.1$ Å. This implies that the optimal channel size for Li migration in the LPS glass is approximately 3.1 Å, and that this dimension is achieved for densities near 1.75 $g \cdot cm^{-3}$. Thus, the highest ionic conductivity would have been expected near such density. Experimentally, the highest ionic conductivity value of 1.1 $mS \cdot cm^{-1}$ was observed at 1.84 $g \cdot cm^{-3}$. Even though there is a ~5 % deviation between predicted vs experimental values, it is reasonable to believe that the ionic transport changes observed as a function of density can be explained via theoretical calculations. When hot-pressing LPS 75-25 at 90 MPa a room temperature ionic conductivity of 0.4 mS cm^{-1} was observed. The change observed compared to the sample hot-pressed at 47 MPa is attributed mainly to increased diffusivity reflected as higher ionic conductivity according to the Nernst-Einstein equation. [128] AIMD calculations predicted that when going from 88 % to 94 % relative density (1.65 to 1.77 $g \cdot cm^{-3}$), the Li self-diffusivity increases from 7.8×10^{-8} $cm^2 \cdot s^{-1}$ to 9.6×10^{-8} $cm^2 \cdot s^{-1}$ at 300 K as shown in Figure 5.8b and Table 5.3. Furthermore, activation energies for Li ion conduction are in agreement with the changes observed in Li self-diffusivity; samples with higher Li self-diffusivity exhibit a lower activation energy for Li ion conduction.

	Temperature [K]				
Density [g · cm^{-3}]	**300**	**700**	**850**	**1000**	**Ea [eV]**
1.56	7.08 x 10^{-8}	1.99 x10^{-5}	4.04 x10^{-5}	7.08 x10^{-5}	0.255
1.65	7.80 x10^{-8}	1.94 x10^{-5}	4.58 x10^{-5}	6.70 x10^{-5}	0.251
1.76	9.64 x 10^{-8}	1.91 x10^{-5}	3.45 x10^{-5}	6.34 x10^{-5}	0.238
1.89	6.47 x 10^{-8}	1.55 x 10^{-5}	3.23 x 10^{-5}	5.32 x 10^{-5}	0.248
2.42	9.60 x10^{-10}	2.01 x10^{-6}	5.09 x10^{-6}	1.13 x10^{-5}	0.345

Table 5.3 *Calculated Li diffusion coefficients in* $cm^{2}{\cdot}s^{-1}$ *and energy of activation for ionic conduction in LPS 75-25 samples as a function temperature and pressure*

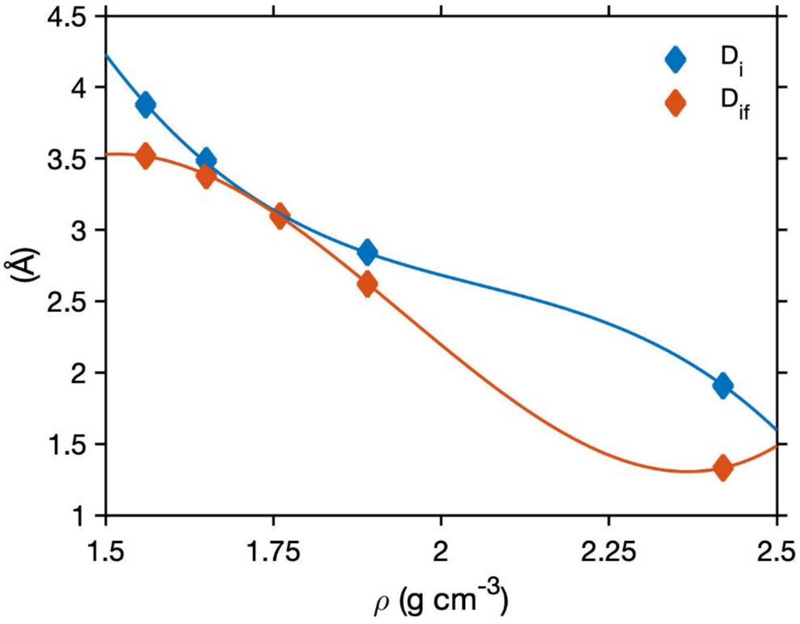

Figure 5.10 *Calculated largest included sphere* D_i *(blue diamonds) and the largest included sphere along the free sphere path* D_{if} *(orange diamonds) in* Li_3PS_4 *glass. The lines are a cubic polynomial fit to the data at five densities*

The largest change in ionic conductivity compared to the cold-pressed sample occurred when hot-pressing LPS at 180 and 270 MPa, resulting in 1.0 mS cm^{-1} and 1.1 mS cm^{-1}, respectively. The increase in conductivity observed in the LPS hot-pressed at 180 and 270 MPa is also consistent with the microstructural changes (glassy fractures and nearly theoretical densities). Aside from the optimal channel size found for Li migration in LPS glass that facilitates ionic transport, the impact of densification on Li diffusivity for different Li coordination environments was quantified. It has been reported that Li-ions in thiophosphate glasses experience a range of different coordination environments. [125] Therefore, partial pair distribution functions (p-PDF) and total neutron weighted PDF, G'(r) were simulated, (Figure 5.11) and compared to the experimental data acquired via neutron scattering. First, from the pair distribution functions (PDF) obtained via neutron diffraction (Figure 5.8c), it was observed that the Li environment changes as a function of molding pressure. More specifically, shifts on the bond lengths for the Li-S pairs were measured. The sample hot-pressed at 270 MPa with highest ionic conductivity of 1.1 $mS \cdot cm^{-1}$ showed a Li-S bond distance of 2.54 Å compared to a bond distance of 2.4 Å for the sample hot-pressed at 90 MPa (0.4 $mS \cdot cm^{-1}$). Even though the Li-Li bond lengths were not well defined to determine shifts, calculations determined that Li-S polyhedra exhibiting corner sharing show a Li-S bond length of 2.52 Å as opposed to a 2.43 Å bond length for Li-S polyhedra with a face-sharing configuration. Although the shift between Li-S pairs was not expected to increase as the molding pressure increased, mechanical anisotropy has been reported for $Li_4P_2S_6$ via first-principles calculations. [129] Based on the Raman spectra collected, *hypo*-thiophosphate species ($P_2S_6^{4-}$) were indeed present in the samples and the mechanical anisotropy of such species may be accentuated at higher molding pressures, and could explain the shift observed. Nevertheless, corner-sharing and face-sharing configurations differ considerably in activation energies for Li ion conduction 0.25 vs 0.34 eV, respectively. Additionally, the corner-sharing configuration presents about an order of magnitude higher Li diffusivity values compared to the face-sharing configuration (9.2×10^{-8} $cm^2 \cdot s^{-1}$ and 9.6×10^{-9} $cm^2 \cdot s^{-1}$ at 300K and 1 bar, respectively). Further characterization with ^7Li NMR spectroscopy is needed to analyze molecular interactions more thoroughly. Nonetheless, the increase in diffusivity with pressure reaches a limit when the available volume of cation diffusion pathways constrains anion rotational mobility. [125] This is consistent with the calculations performed that showed a diffusion coefficient nearly one order of magnitude lower when pressing LPS glass at a hypothetical pressure of 100 x10^2 MPa (Figure 5.8b). The slight decrease in conductivity of LPS hot-pressed at 360 MPa could be explained by this constriction in anion reorientation [125] and the presence of microcracks in the microstructure resulting in an ionic conductivity of 0.8 mS cm^{-1}.

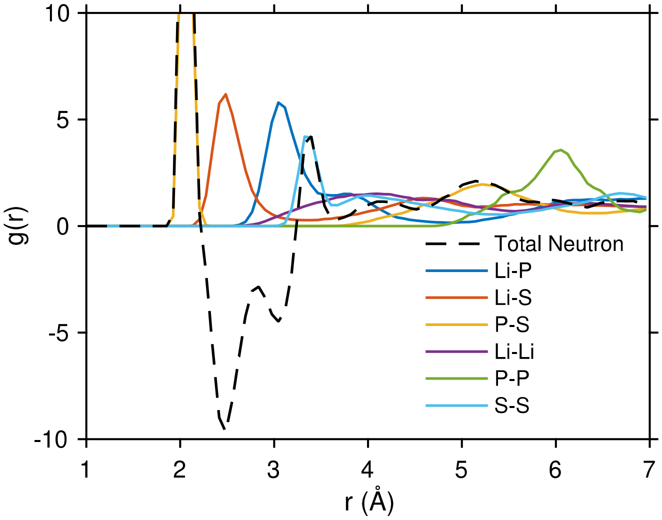

Figure 5.11 *Local ordering of amorphous LPS 75-25 at 25 °C. Calculated partial pair distribution functions (p-PDF) and total neutron weighted PDF, G' (r)*

Additionally, critical current density (CCD) measurements were performed at room temperature as a function of stack pressure (1.5, 3.1 and 6.1 MPa) for cold-pressed LPS, and at 60 °C, 1.5 MPa for both LPS cold-pressed and hot-pressed at 270 MPa (Figure 5.12, Figure 5.13 and Table 5.4). As it was expected from the outcomes of this work, the sample that was hot-pressed at 270 MPa, with higher ionic conductivity and less volume fraction of porosity (2 % compared to 12% for the cold-pressed) exhibited a CCD of 1.1 mA·cm^{-2} compared to 0.4 mA·cm^{-2} for the cold-pressed sample at 60 °C, 1.5 MPa. Even though the CCD increased by a factor of almost three, the voltage traces of the hot-pressed sample showed significant overpolarization suggesting unstable cycling at the higher current densities (Figure 5.12c). The tests performed at different stack pressures elucidated that the overpolarization was a result of loss in contact area due to void formation between the electrode and electrolyte as it has been observed and reported in other systems, such as: Li-argyrodite (Li_6PS_5Cl),[130] Li-LLZO,[131,132] and Na-Na ß'' alumina.[133] Given that Li creep is the dominant mechanism transporting Li to the interface rather than Li diffusion,[130,131] such replenishment can be aided via stack pressure or temperature. In the case of the measurements conducted at room temperature, it was observed that the critical stack pressure (pressure at which the rate of replenishment of Li at the interface is equal to the rate at which Li is depleted from it) was $\geq$ 3.1 MPa at 0.1 $mA \cdot cm^{-2}$. However, such stack pressure could not be applied to the sample hot-pressed at 270 MPa without fracture given its brittle nature. Hence, the attempt of testing CCD of the hot-pressed sample at a lower stack pressure (1.5 MPa) at 60°C. It is worth noting that the critical stack pressure is dependent on the current density. Thus, even though Li creep was facilitated by temperature, it was not sufficient to remain below the critical current density for stripping resulting in loss of contact between Li and LPS, leading to increasing local current density for the same overall current density. In other words, the limitation of applying a high enough stack pressure to enable sufficient Li replenishment at the Li-LPS interface impeded the measurement of the "real" CCD for plating in this system, which would be expected to be $\geq$ 1.1 $mA \cdot cm^{-2}$. These results highlight some of the practical challenges that sulfide-based and other solid electrolytes need to overcome to enable all-solid-state batteries.

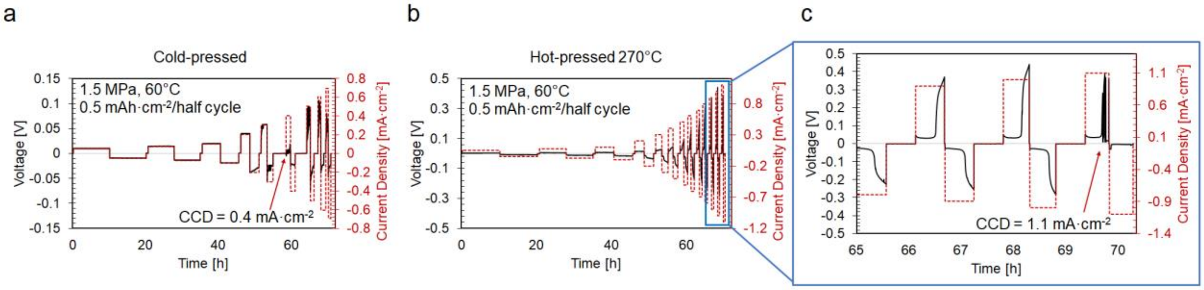

Figure 5.12 *Critical Current Density (CCD) measurements of LPS 75-25 at 1.5 MPa, 60 °C. (a) Cold-pressed sample, (b) Hot-pressed sample at 270 MPa, (c) zoomed-in galvanostatic test of the hot-pressed sample at 270 MPa from 65 h to 72 h.*

Stack pressure [MPa]	CCD [mA·cm^{-2}]
1.5	0.3
3.1	0.4
6.2	0.4

Table 5.4 *Critical Current Density (CCD) measurements of cold-pressed LPS 75-25 at room temperature, as a function of stack pressure*

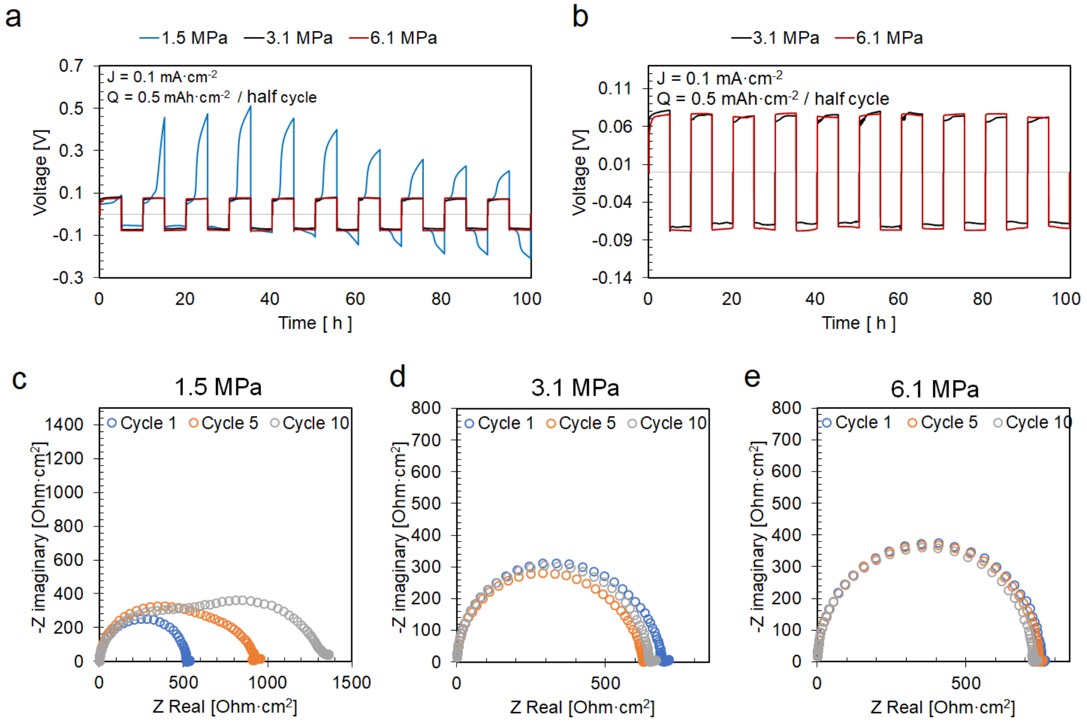

Figure 5.13 *AC and DC testing of Li-LPS-Li symmetric cells under constant current density of 0.1 mA·cm^{-2}, fixed charge of 0.5 mAh·cm^{-2} per half cycle as a function of stack pressure. (a) Voltage response as a function of stack pressure. (b) Voltage response under a stack pressure of 3.1 and 6.1 MPa. Impedance evolution at (c) 1.5 MPa, (d) 3.1 MPa, and (e) 6.1 MPa.*

Molding Pressure [MPa]	Molding temperature [°C]	Density [±0.01 g cm^{-3}]	RMS Roughness	Ultrasonic velocity		Nanoindentation		Ionic conductivity @25°C [mS cm^{-1}]
				Shear Modulus [GPa]	Young's Modulus [GPa]	Young's Modulus [GPa]	Hardness [GPa]	
47	200	1.71		6.4 ± 0.2	16.7 ± 0.6			0.3
90		1.73		6.3 ± 0.2	16.5 ± 0.5			0.4
180		1.80		11.8 ± 0.2	30.9 ± 0.5			1
270		1.84	35.03 ± 13.20	10.7 ± 0.7	28.0 ± 0.6	26.1 ± 3.1	0.65 ± 0.07	1.1
360		1.86		----	----			0.8
360	25	1.67	30.03 ± 1.24	5.3 ± 0.5	13.7 ± 1.3	13.2 ± 1.0	0.29 ± 0.04	0.2

Table 5.5 *Density, mechanical properties and ionic conductivity of LPS 75-25 as a function of molding pressure*

5.3 Conclusions

In this work, it was demonstrated that Li_2S-P_2S_5 75-25 can be densified close to its theoretical density while preserving the preferred amorphous phase by hot-pressing at the glass transition temperature (~200 °C) at 180 MPa or above. Through the simultaneous application of pressure at T_{glass} to facilitate plastic flow, but below $T_{crystallization}$ to prevent crystallization, near theoretical density was achieved. Moreover, the distinction between particles and particle boundaries was nearly eliminated at 270 MPa or above, resulting in a material that more closely resembled a melt-processed glass. If it were not for the simultaneous application of pressure above 47 MPa, we believe crystallization would have occurred as we previously demonstrated. [19] It was observed that crystallization was suppressed using pressures $\geq$ ~90 MPa at T_{glass} by eliminating particle boundaries and pores that would otherwise act as nucleation sites to promote crystallization of the less desirable thio – LISICON III-analog phase. Even though the metastable crystalline thio-LISICON III analog phase exhibits slightly higher ionic conductivity than the amorphous phase, the presence of grain boundaries may not be desirable as they are known to facilitate Li propagation at higher charging rates. [16] In this study, the application of relatively high pressure (47 MPa) while heating at T_{glass} resulted in dramatic changes in material properties such as the mechanical and electrical properties. While changes to the extrinsic properties were observed and analyzed, such as microstructure and relative density, changes to the intrinsic properties such as *E* and the ionic conductivity were also observed.

The change in *E* was divided in two regimes. One that is distinguished mainly by reduction in the volume fraction of porosity and the other that combines the latter with intermediate-range order changes; rearrangement of atoms at the molecular level leading to a more compact material. The cold-pressed and hot-pressed at 47 and 90 MPa, which observed a slight increase in relative density as a function of molding pressure (3 % RD) are in excellent agreement with the exponential relationship between *E* and the volume fraction of porosity described by Rice et al. [116] However, when hot-pressing at 180 MPa and above, changes at the molecular-level may explain the significant increase (>100%) in *E*. The pair distribution functions collected via neutron diffraction with a higher mean coordination number, mostly on the Li-S pairs, suggested a more interconnected arrangement between the Li and S atoms, resulting in higher elastic constants. This is considered a change in intrinsic behavior that we believe is a result of the simultaneous application of pressure and temperature during densification.

This study also showed that LPS hot pressed at 200 °C and 270 MPa with a 98% relative density can attain ionic conductivities of 1.1 $mS\cdot cm^{-1}$ at room temperature with a higher *E* compared to a standard processed cold-pressed sample (360 MPa) with a room temperature ionic conductivity of 0.2 $mS\cdot cm^{-1}$, 89% dense. This conductivity represents the highest room temperature ionic conductivity reported for the LPS 75-25 composition to date. The step increase in ionic conductivity was attributed to a change in Li coordination environment for the sample hot-pressed at 270 MPa, that exhibited the highest value of 1.1 $mS\cdot cm^{-1}$ at room temperature. The change between corner-sharing to face-sharing of the Li-S polyhedra with higher diffusivity at 270 MPa found via neutron pair distribution functions and the reduction of the available volume of cation diffusion pathways facilitates the Li ion mobility in the glass structure. Such favorable Li coordination environment and increased diffusivity and mobility explain the step increase in ionic conductivity as a function of molding pressure. Nevertheless, the increase in diffusivity with pressure reaches a limit when the available volume of cation diffusion pathways constrains anion rotational mobility, which we believe it explains the slight decrease in ionic conductivity of the sample hot-pressed at 360 MPa. Interestingly, it was found that the residual stress could play an important role not only on the mechanical integrity of the specimens resulting in an increase in brittleness, but also in ionic transport. The ionic transport behavior observed on the denser microstructures (at and above 1.77 $g \cdot cm^{-3}$, molding pressure of ≥ 90 MPa) could be explained by the microstructures constructed through ab *initio* Parrinello-Rahmen dynamics (NPT) at and above 360 MPa, suggesting that even though the EIS measurements were performed at 3.15 MPa, the microstructures resemble the properties of microstructures that are under compression at 360 MPa and above. This was an unexpected result; thus, we believe that the role that residual stress could play on Li transport and consequently in Li electrodeposition should be considered for future studies.

Although it is counterintuitive that a metal such as Li, that is relatively soft at room temperature, [120,121] could penetrate stiff ceramic solid electrolytes, [134] it has been shown that this is possible at high charging rates. [57] Moreover, pores and particle/grain boundaries are common defects that are believed to play a role in causing ionic current focusing effects or “hot spots,” thus influencing stable vs unstable Li electrodeposition. [15,16,18] From this work it was observed that such defects can be tuned by changing the processing conditions. It was found that E is affected by defects such as pores, but most importantly by molecular arrangements. Moreover, these rearrangements result in a higher diffusivity increasing ionic transport. The outcomes of this work show that optimization of the microstructure of the solid electrolyte likely be intimately connected to the maximum tolerable current density since it can define the resulting defects/properties that have been identified to have an effect on CCD. In addition, the importance of external variables such as stack pressure and/or temperature to aid Li creep during stripping were identified as practical challenges that sulfide-based solid electrolytes need to overcome to enable all-solid-state batteries. Finally, this work provides insight into processing-structure-property relationships that can be used as a guideline to increase the feasibility of LPS-based all-solid-state battery technology.

5.4 Experimental Details

5.4.1 Synthesis and processing

The amorphous $75Li_2S\text{-}25P_2S_5$ (mol %) solid electrolyte was synthesized from crystalline Li_2S (99.98%, Aldrich) and P_2S_5 (99%, Sigma Aldrich) by mechanochemical synthesis after being mixed in an agate mortar and pestle. The mixed precursors were placed in a 45-cc zirconia pot with 10 zirconia balls of 10 mm in diameter and 10 zirconia balls of 5 mm in diameter, sealed in a dry Ar-filled glovebox (water concentration below 0.5 ppm), placed inside stainless steel vessels and transported in an inert atmosphere. The pots were spun at 510 RPM for 10 h in a Planetary Micro Mill (Pulverisette 7, Fritsch GmbH), with 2-hour intervals of milling followed by 10-minute rest intervals at room temperature.

Milled LPS 75-25 powder was hot-pressed at 200°C for 4h between 47 and 360 MPa with a heating rate of 0.7 ± 0.1 $°C\cdot min^{-1}$ by resistive heating. Cold-pressed pellets (25°C) were pressed at 360 MPa for 10 min using a 6 mm diameter stainless steel die in a double-acting configuration.

5.4.2 Glass transition determination via thermomechanical analysis (TMA)

Assignment of the glass transition temperature (T_{glass}) of the cold-pressed LPS specimens was conducted by TMA using (TA Instruments, Q400, 6.07 mm diameter macro-expansion probe) in an Argon atmosphere. Expansion mode was selected, following ASTM Standard Test Method E1545-11 (Reapproved 2016) [135] Cold-pressed specimens were 6 mm and > 2 mm in diameter and thickness, respectively, heated at 0.7°C min^{-1} – same heating rate used for hot-pressing the samples. No temperature gradients are considered to have affected the data acquired given the slow heating rate used and the thickness of the samples. The TMA specimens were tested using a preload of 0.01 N to ensure good contact between the probe and the specimen. 0.2 N was used as the applied force, and argon as the purge gas (200 mL min^{-1}). To reduce presence of moisture, the TMA instrument chamber was heated at 10 °C min^{-1} to 400 °C for 30 min and cooled down before loading the samples. The intersection of the extrapolation of the slope of the probe displacement curve before and after the transition was used to determine the glass transition temperature.

5.4.3 Crystallization temperature determination via Differential Scanning Calorimetry (DSC)

The cold-pressed sample and hot-pressed samples were grounded with an agate mortar and pestle and sealed in aluminum hermetic pans inside a dry (< 0.5 ppm H_2O) Ar-filled glovebox. To avoid any residual moisture, the aluminum pans were kept in a vacuum oven at 120 °C. The samples were transferred to the DSC (Q-100, TA Instruments) and heated under flowing nitrogen gas (50 mL min^{-1}) within a temperature range from 40 to 300°C using a heating rate of 0.7°C min^{-1}. The zeroline was subtracted from the measured heat flow rate on all samples to get the true sample heat flow rate eliminating influences from apparatus and reference samples, and facilitate analysis of transitions.

5.4.4 Density determination

Mass densities were obtained by the Archimedes Principle using an Archimedes density determination kit (OHAUS Corp., NJ) inside a dry Ar-filled glovebox. Wet masses were measured with pellets immersed in cyclohexane.

5.4.5 Microstructural features via Scanning Electron Microscopy (SEM)

Fractured surfaces of the LPS cold-pressed and hot-pressed bulk specimens were mounted on carbon tape and examined by SEM (JSM-7800F, JEOL) at 15.0 kV using an air-tight transfer vessel (JU2010218, JEOL).

4.4.6 Crystallinity via X-Ray Diffraction (XRD)

Long-range order and identification of the crystalline phases present were determined by analysis of X-ray diffraction patterns (CuKα 1.54 Å radiation, step size 0.1°, scan speed of $0.1°2\theta\cdot min^{-1}$) at 40 kV and 15 mA using a diffractometer (Smartlab X-Ray diffractometer, Rigaku). The electrolyte pellets were manually ground in an agate mortar and pestle, and then placed in an air-free holder with a Beryllium window (2455-SH-001, Rigaku) to perform the analysis. The thio-LISICON III XRD pattern adapted from Kanno et al. [59] was digitized by PlotDigitizer 2.6.6.

5.4.7 Elastic constants from ultrasonic velocity measurements

This technique displaces particles through a material via propagation of a longitudinal or shear wave. For isotropic materials, such as glasses, the two types have distinct values of wave velocity that depend on structural characteristics such as density and elasticity. Thus, this method can be used to determine the elastic constants of materials with different structural properties in a non-destructive way.

The samples were prepared following the ASTM E494-15 standard [136] and tested inside of a dry (< 0.5 ppm H_2O) Ar-filled glovebox using a pulse-receiver from Olympus (5073PR with M110 and V156 transducers). The couplants used were mineral oil and SWC-2 from Olympus for longitudinal and shear wave speed measurements, respectively. The equations used to determine the elastics constants are as follows:

$$\mathrm{V_L} = \frac{2 \cdot \Delta \mathrm{x}}{\Delta \mathrm{t_L}} \qquad (5.1)$$

$\mathrm{V_L}$ denotes the longitudinal speed, Δx corresponds to the specimen thickness in which the wave travels through and $\Delta \mathrm{t_L}$ the time of flight that takes the longitudinal wave to travel the specimen back and forth during a pulse-echo measurement. The same equation is used to determine the shear/transverse wave speed using the corresponding time of flight. The time of flight was measured with an oscilloscope (PicoScope 2207a, Pico Technologies).

$$G = \rho \cdot v_s^2 \qquad (5.2)$$

Where G corresponds to the shear modulus, ρ is the density of the material being tested and v_s is the shear/transverse wave speed.

The Young's Modulus was calculated using the equation below:

$$E = \frac{[\rho v_s^2 (3v_l^2 - 4v_s^2)]}{(v_l^2 - v_s^2)} \qquad (5.3)$$

Where v_L and v_s corresponds to the longitudinal and shear wave speed, respectively.

5.4.8 Young's Moduli and Hardness via nanoindentation

Nanoindentation was performed using a Hysitron 950 Triboindenter using a high-load Berkovich probe. The samples were mounted on magnets (Ted Pella, AFM specimen disks) and polished for surface preparation inside a dry Ar-filled glovebox. Silicon carbide 1200 grit sandpaper was used as initial polishing step, followed by 30 um, 15 um, 6 um, 1um and 0.5 um diamond pastes against PSA polishing cloths (Mager Scientific). A glass plate along with a custom-made holder were used to maintain flat surfaces, anhydrous cyclohexane was selected to rinse the samples between polishing steps. The samples were transferred to the instrument using air-tight containers, and a thin layer of mineral oil (non-reactive with LPS) was applied onto the samples to protect them from moisture exposure during measurements. The measured values did not change throughout the acquisition period (~1h). Thus, validating that the mechanical integrity of the samples was conserved throughout the measurements.

The initial unloading contact stiffness, S, for an axisymmetric indenter such as a Berkovich probe, the relationship is:

$$S = \frac{dP}{dh} = \frac{2}{\sqrt{\pi}} E_r \sqrt{A} \qquad (5.4)$$

Where P denotes the indentation load, h the displacement during one complete cycle of loading and unloading. E_r corresponds to the reduced modulus that accounts for the fact that measured elastic displacement includes contributions from both the specimen and the indenter. The reduced modulus is given by:

$$\frac{1}{E_r} = \frac{\left(1-\nu_f^2\right)}{E_f} + \frac{\left(1-\nu_i^2\right)}{E_i} \qquad (5.5)$$

Where E_f and ν_f are the elastic modulus and Poisson's ratio of the specimen, and E_i and ν_i are the same quantities for the indenter (Berkovich, $E_i = 1140$ GPa and $\nu_i = 0.07$). In order to independently establish the hardness and modulus, the projected contact area needs to be measured [17]. The contact areas measured for the cold-pressed sample (360 MPa) and hot-pressed sample at 270 MPa were 8.873 μm^2 and 6.118 μm^2, respectively.

$$H = \frac{P_{max}}{A} \qquad (5.6)$$

Where P_{max} is the peak load and A corresponds to the contact area.

5.4.9 Surface imaging via Atomic Force Microscopy (AFM)

Atomic Force Microscopy was performed using a Hysitron 950 Triboindenter with in-situ imaging capabilities. A PeakForce tapping technique was used, where the maximum load applied was 2 uN. The samples were transferred to the instrument using air-tight containers, and a thin layer of mineral oil (non-reactive with LPS) was applied onto the samples to protect them from moisture exposure during imaging.

5.4.10 Electrochemical Impedance Spectroscopy (EIS) measurements

Symmetric Li | LPS | Li cells were assembled (99.9% metals basis, 750 um thick, Alfa Aesar) and aligned with a Teflon PTFE tube using nickel pins (99.98% purity, Goodfellow) as current collectors. EIS measurements were acquired on a potentiostat (BioLogic VMP 300) at room temperature under 3.5 MPa (load necessary to minimize the effect of stack pressure on cell impedance). The frequency range used was 50 mHz to 7 MHz using 10 mV as the perturbation voltage and 3 measurements were acquired per frequency. Li metal electrodes were used for ionic conductivity measurements due to inaccessibility to a sputter coater inside an inert atmosphere. Additionally, the ability to achieve low interfacial resistances between Li and LPS allows to clearly identify the contribution of each transport phenomena of the spectra. Since it is known that LPS reacts with Li to form an SEI, measurements were conducted immediately after cell assembly to eliminate Li-LPS contact time as a variable. Furthermore, equivalent circuit modeling was performed to validate the analysis. The equivalent circuit used to analyze frequency-dependent transport phenomena was $Z_u + Q_{Bulk}/Z_{Bulk} + Q_{CT,\ Li\text{-}LPS}/Z_{CT,\ Li\text{-}LPS}$, where Z_u corresponds to the uncompensated impedance, Q_{Bulk} and Z_{Bulk} correspond to the constant phase element and ionic impedance of the bulk, respectively. $Q_{CT,\ Li\text{-}LPS}$ and $Z_{CT,\ Li\text{-}LPS}$ denote the constant phase element and impedance at the electrode/electrolyte interface (CT = charge transfer).The results obtained for the fitting are listed in Table 5.2. 1.27 cm^2 was the area used for the cold-pressed, hot-pressed at 47 MPa and 90 MPa samples. 0.079 cm^2 was the area used for the samples hot-pressed at 180 MPa, 270 MPa and 360 MPa.

5.4.11 High resolution Pair Distribution Functions (PDF)

The samples used were synthesized with a 99 atomic percent ^{7}Li enriched mixture for the Li_2S precursor and pressed at the same conditions as the samples with natural Li (92.5 at % ^{7}Li, 7.5 at % ^{6}Li). The samples were ground into powder using an agate mortar and pestle and sealed in quartz capillaries (2 mm in diameter, 0.01 mm for the wall thickness, Hampton Research, ~60 mm^3 of sample) in a dry (< 0.5 ppm H_2O) Ar-filled glovebox. The measurements were carried out at 380K using the Nanoscale-Ordered Materials Diffractometer (NOMAD) at Oak Ridge National Laboratory, Spallation Neutron Source. The data was reduced and corrected for attenuation and multiple scattering using ADDIE (ADvanced Diffraction Environment) user software.

5.4.12 Raman Spectroscopy

Raman spectra were collected using a Horiba instrument (LabRAM HR-800, Horibausing). A 532 nm laser was used, spot size of 50 um. Samples were loaded and sealed in a quartz window holder custom-made inside of a dry Ar-filled glovebox.

5.4.13 Computational methods

Ab initio molecular dynamics (AIMD) were conducted to study the structure and diffusivity of amorphous Li_3PS_4. The initial amorphous structure with Li^+ and tetrahedral PS_4^{3-} ionic units was generated via a Monte Carlo approach [137] with periodic boundary conditions at a density of 1.88 g cm^{-3}; followed by a AIMD melt-and-quench routine. The structure was heated to 1000 K at 70 K·ps^{-1}, held at 1000 K for 3 ps, then cooled at the same rate with an additional 3 ps of equilibration at the target temperature. The simulation cell consisted of 60 Li^+ and 20 PS_4^{3-} ions. Calculations were performed using the Vienna ab initio simulation package. [138] The generalized gradient approximation in the formulation of Perdew-Burke-Emzerhof was used in combination with the projector augmented method. [139,140] Li trajectories were propagated with a 2 femtosecond time step within the isothermal-isobaric (NPT) ensemble, employing the Langevin thermostat. [111] The plane-wave energy cutoff was set to 400 eV and a single k-point was used. Li diffusivities were evaluated using the Einstein relation:

$$D = \frac{1}{6tN} \sum_i^N \langle |\boldsymbol{r}_i(t+t') - \boldsymbol{r}_i(t')|^2 \rangle \tag{5.7}$$

Where $\boldsymbol{r}_i(t)$ is the position of the i_{th} Li ion, N is the number of Li ions, and the enclosing brackets $\langle \cdots \rangle$ indicate an average over the time interval *t*. The diffusivity was calculated at temperatures of 700, 850, and 1000 K; and at pressures of 0.1, 360, 1000, 2000, and 100 × 10^2 MPa.

The elastic properties of amorphous Li_3PS_4 subject to hydrostatic pressure were calculated with DFT using the stress-strain approach. [141] The amorphous simulation cell exhibited triclinic symmetry, which requires the calculation of 21 independent elastic coefficients C_{ij}. The stresses resulting from the application of six finite strains with displacements of ±0.015 Å were used to solve for C_{ij} in $\sigma_i = C_{ij}\varepsilon_j$ $(i, j = 1,2, \dots, 6)$. The force and electronic convergence were set to 10^{-4} eV/Å and 10^{-6} eV, respectively. The bulk, shear, and Young's moduli were subsequently determined using the Voigt-Reuss-Hill approximation. This approximation relates the single-crystal elastic constants to the polycrystalline elastic moduli. [142] The Voigt (V) moduli provide an upper bound to these values, the Reuss (R) moduli provides a lower bound, and the Hill (H) moduli is the arithmetic average of the two. The bulk *B* and shear modulus *G* within these approximations are defined as:

$$B_V = \frac{\left(C_{11} + C_{22} + C_{33} + 2(C_{12} + C_{23} + C_{31})\right)}{9} \tag{5.5.8}$$

$$\mathrm{B_R} = \frac{1}{\left(\mathrm{S}_{11} + \mathrm{S}_{22} + \mathrm{S}_{33} + 2(\mathrm{S}_{12} + \mathrm{S}_{23} + \mathrm{S}_{31})\right)} \tag{5.5.9}$$

$$\mathrm{B_H} = \frac{(\mathrm{B_V} + \mathrm{B_R})}{2} \tag{5.5.10}$$

$$\mathrm{G_V} = \frac{\left(\mathrm{C_{11}} + \mathrm{C_{22}} + \mathrm{C_{33}} - \mathrm{C_{12}} - \mathrm{C_{23}} - \mathrm{C_{31}} + 3(\mathrm{C_{44}} + \mathrm{C_{55}} + \mathrm{C_{66}})\right)}{15} \tag{5.5.11}$$

$$\mathrm{G_R} = \frac{15}{\left(4(\mathrm{S_{11}} + \mathrm{S_{22}} + \mathrm{S_{33}}) - 4(\mathrm{S_{12}} + \mathrm{S_{23}} + \mathrm{S_{31}}) + 3(\mathrm{S_{44}} + \mathrm{S_{55}} + \mathrm{S_{66}})\right)} \tag{5.5.12}$$

$$\mathrm{G_H} = \frac{(\mathrm{G_V} + \mathrm{G_R})}{2} \tag{5.5.13}$$

where $\mathrm{S} = \mathrm{C}^{-1}$ is the compliance matrix and the subscripts refer to either the Voigt, Reuss, or Hill moduli. Finally, the Young's modulus E and Poisson's ratio v are determined by:

$$E = \frac{9BG}{3B + G}, \quad \nu = \frac{(3B - 2G)}{2(3B + G)} \tag{5.5.14}$$

The Voight-Reuss-Hill approximation is ideal for an amorphous material since the approach averages all methods over all possible lattice orientations. [142] Given that there is no directionality in amorphous materials, this approach is best suited for LPS in this work.

An analysis of the connectivity of void/pore space within Li_3PS_4 glass that is available for Li+ migration was obtained via Voronoi network analysis (Zeo++ code). [143] Ionic radii were adopted as the effective sizes for each elemental component. [144]

CHAPTER 6 Electrostatic potential effect on charge transfer processes at the Li-LLZO interface in connection with Li metal penetration through the garnet solid electrolyte

6.1 Introduction

Li metal solid electrolyte batteries (LMSSBs) have gained significant attention for their potential to meet the energy storage demands for applications such as electric vehicles (EVs) and microelectronics. [8] Replacing the liquid electrolyte in state-of-the-art Li-ion technology with a SSE that is non-flammable can also address safety concerns. However, despite significant progress made in achieving ionic conductivities commensurate with liquid electrolytes [9,10,35–37] and achieving low Li-SSE interface resistance (< 10 $\Omega.cm^2$),[12] the maximum charge rate does not match that of Li-ion technology (> 1C or ~3$mA\cdot cm^{-2}$) in planar cell architectures. Owing to their relatively high bulk elastic moduli, [88,134] presumably ceramic SSE should be impenetrable by Li metal; however, this is not the case. It has been observed that at charging current densities in the 0.1 to 1 $mA\cdot cm^{-2}$ range in planar cell architectures Li metal penetrates all ceramic bulk-scale SSEs. [15,16,19,96]. To explain Li nucleation and propagation through SSEs under electrolytic conditions, several mechanisms have been proposed based on experimental observations and theoretical modelling. Recent studies have examined the role of surface defects/mechanical properties [15,145], Li^+ flux imbalance at the interface due to limited self-diffusivity of Li or lack of intimate interfacial contact [12,57,131,146] and electronic conduction in the SSE causing internal precipitation of the alkali metal under electrolytic conditions [147]. [148] While these studies are remarkably enlightening, a specific analysis of Li nucleation at and below cathodic potentials of 0 V has not been directly addressed. Assessing the electrochemical stability of a SSE at 0 V vs Li/Li^+ can help determine whether a Li metal anode could be enabled.

Earlier work in Na -ß'' alumina (SBA) attributed sodium metal penetration to two failure mechanisms upon charging. First, Mode I proposed that a path for dendrite growth was created by fracture of the ceramic SSE as a result of stress near the tip of an existing surface crack. The driving force for rupture was the Poiseuille pressure arising from the "flow" of metal (as a result of electrolysis) in the crack. [149] Mode II proposed that failure occurred as a result of internal electrolysis, which leads to internal alkali metal precipitation when a critical potential over the electrolyte was exceeded and electrons are transferred from the electrode to the SSE. This phenomenon was proposed to be facilitated by the polarization of the Na-SBA interface upon charging. [148,150,151] However, the lack of a reference electrode prevented isolation of each interface polarization to further understand the charge transfer processes at the interface. Furthermore, the electronic structures of neither the bulk or surface of the ceramic SSE under reducing conditions were estimated/evaluated via theoretical calculations to validate the transfer of electronic species (electrons) from the adjacent electrode.

Although a purely mechanical or electronic mechanism do not necessarily occur independently, but can occur simultaneously or consecutively, this work intends to address the unresolved questions regarding the electronic aspect of the phenomenon. Herein, we consider the Li- $Li_{6.25}Al_{0.25}La_3Zr_2O_{12}$ (LLZO) interface instability as a voltage-controlled phenomenon. LLZO was selected as a model system, as its chemical stability against Li facilitates the analysis of the Li-LLZO interfacial stability upon charging/plating. In addition, it has been predicted to show the lowest reduction potential of as low of 0.05 V, and the least favorable decomposition potential of only -0.02 eV per atom at 0 V vs. Li/Li^+ among the most promising ceramic SSEs. [34] Toward this goal, a reference electrode was integrated into a solid-state cell that allowed to control the plating potential of the Li-LLZO interface and consequently, the charge transfer processes occurring at such interface ≤ 0 V vs. Li/Li^+. The potential onset at which Li nucleation occurred (critical potential, V_c) was identified and described using a combination of direct and alternate potentiostatic measurements. First-principal calculations were used to predict the density of states (DOS), band gap, and absolute positions of the band edges of LLZO under reducing conditions. A V_c was clearly observed below (i.e. more negative than) 0 V vs. Li/Li^+; the first measurement of a critical potential in a SSE. Moreover, we hypothesize that the origin of V_c may be quantum mechanical in nature. The outcomes from this study provide new insight into one of the underlying mechanisms that drive failure in ceramic electrolytes upon charging/plating that could serve as a guideline towards enabling higher rate-capabilities in LMSSBs.

6.2 Results and Discussion

6.2.1 Three-electrode critical current density (CCD) measurement

To decouple the voltage contribution of each electrode from the cell potential response (WE – CE, black trace in Figure **6.1**), three-electrode cells were assembled. Moreover, the Li | SSE DC electrochemical stability was evaluated via galvanostatic cycling to determine the critical current density (CCD) of LLZO. CCD is the current density at which Li metal penetrates the SSE throughout its thickness, thus, it determines the rate capability of a LMSSB.

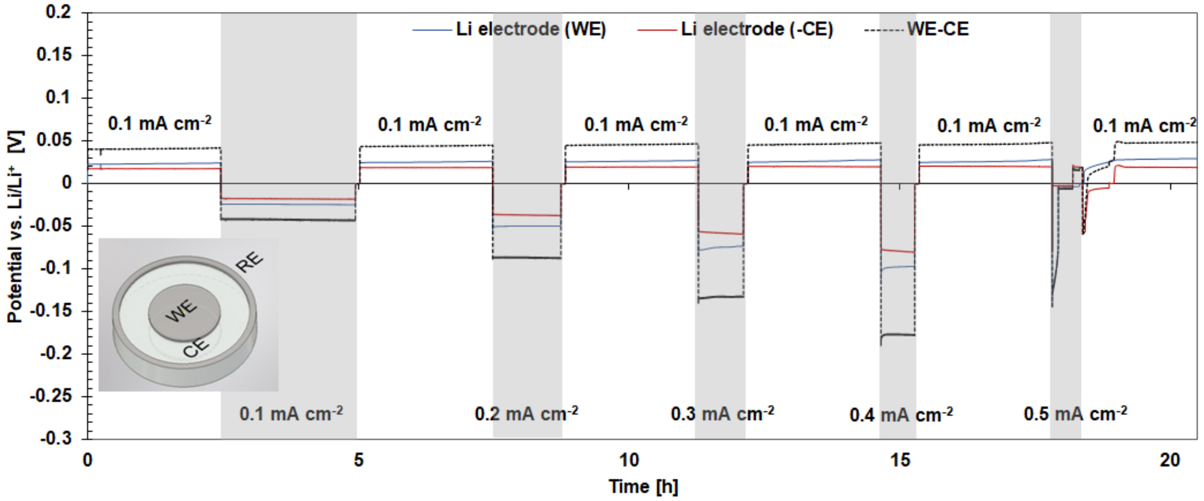

Figure 6.1 *Li-Li$_{6.25}$Al$_{0.25}$Zr$_2$O$_{12}$ (Li-LLZO) DC electrochemical stability as a function of current density. Three-electrode measurements showing the cell polarization contributions from the Li working electrode (WE) and Li counter electrode (CE). The CE voltage has been inverted for visual clarity. Inset schematic depicts the three-electrode cell configuration designed for this work.*

To characterize the CCD upon plating, the working electrode (WE) Li plating current density was increased in 0.1 mA·cm-2 increments while the counter electrode (CE) Li plating was maintained at a relatively low current density (0.1 mA cm^{-2}) to assure stable Li plating. Three different voltage behaviors were observed during cycling. First, at low current densities (0.1 and 0.2 mA·cm-2), an ohmic behavior or linear potential response was observed and interpreted as stable plating of Li. At 0.3 and 0.4 mA·cm^{-2}, even though the cell potential ostensibly shows a linear response suggesting stable plating, each electrode potential contribution exhibits deviation from Ohm’s law. It is clear that each electrode contribution deviates from stable plating/stripping at the WE and CE electrodes, respectively. The initial peak in the current density segment can be attributed to Li nucleation overpotential on the WE and gradually decreases, whereas the CE electrode potential response gradually increases with time. This increase in potential is interpreted as the Li depletion during stripping that results in an decrease in contact area at that interface as it has been reported in LLZO and other ceramic SSEs.[130–133,152] Finally, at 0.5 mA·cm^{-2}, a drop in polarization is observed near 0 V vs. Li/Li+ interpreted as short-circuiting as a result from Li metal penetration . Inductive behavior observed in Electrochemical Impedance Spectroscopy (EIS) analysis confirmed electronic short-circuiting (Figure 6.2b). These results further validate that a standard two-electrode cell configuration cannot isolate the behavior of a single electrode, thus justifying the need for a three-electrode cell to further understand the interfacial stability of Li-LLZO upon plating.

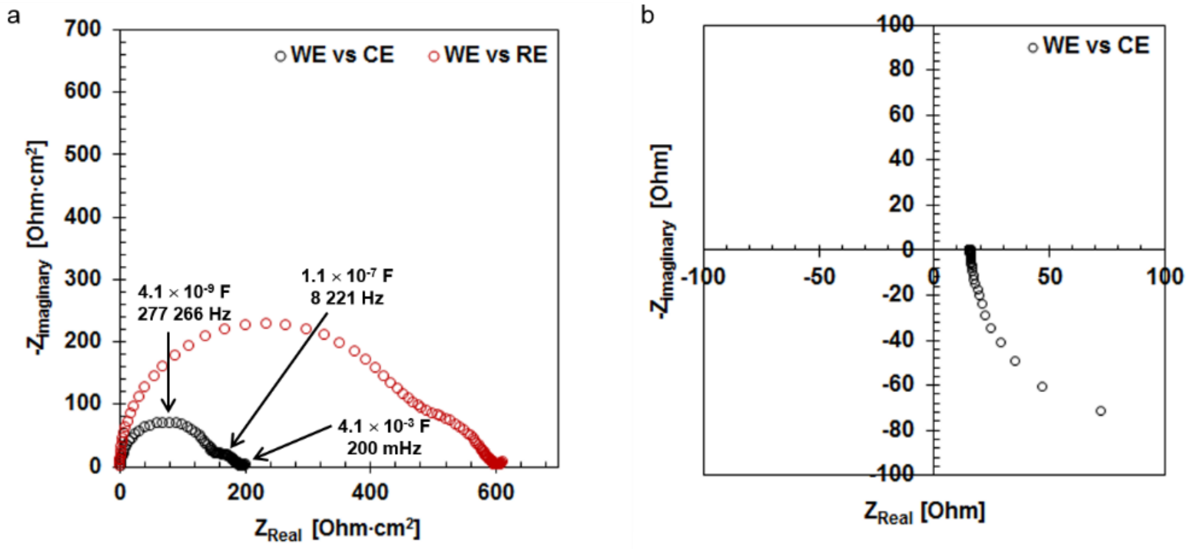

Figure 6.2 *Representative Electrochemical Impedance Spectroscopy (EIS) spectra of Li|LLZO|Li cells. A) Impedance plots of WE versus CE showing characteristic capacitances of different transport phenomena in the electrolyte: 10*$^{-9}$ *F for bulk LLZO, 10*$^{-7}$ *F, for grain boundaries in LLZO and 10*$^{-3}$ *F for Li | LLZO interfaces. Impedance plot between WE and RE shows no electrical short between electrodes. B) Impedance plot between WE and CE electrodes after the critical current density (CCD) has been exceeded showing inductive behavior resulting from Li metal penetration in the solid electrolyte.*

6.2.2 Electrochemical stability of LLZO at low potentials

A wide electrochemical window (~5 – 6 V) is a necessary, but not sufficient condition for evaluating the electrochemical stability of a SSE against a Li anode and a high-voltage cathode according to our previous work. [33] More specifically, to evaluate the garnet LLZO electrochemical stability against a Li anode, the absolute position of its conduction band edge relative to the electrochemical potential of Li metal needs to be determined. This leads to predict whether electron transfer from the Li anode to the LLZO can occur resulting in either electrochemical reduction of LLZO or recombination of electrons with ionic species at the Li-LLZO interface.

Although the electrochemical reduction of LLZO is not thermodynamically favorable according to DFT calculations given its low decomposition potential (-0.02 eV per atom or 49 kJ/mol of LLZO at 0 V vs. Li/Li^+), the phase equilibria at low potentials has been predicted. At the onset of reduction (0.05 V), LLZO decomposes into Zr_3O, La_2O_3, and Li_2O followed by Zr formation at 0.004 V vs. Li/Li^+. [34,42] It is worth noting that the authors stated the small reaction energy suggests that the reduction of LLZO is likely to be kinetically inhibited, and the reduction products may provide passivation to the material. Furthermore, it was inconclusive whether the garnet LLZO is reduced to Zr_3O or Zr at 0 V vs. Li/Li^+ since the energy and voltage magnitudes are below typical accuracy of DFT and the approximations of the scheme. Nevertheless, the formation of Zr would be thermodynamically favorable at a potential significantly lower than 0 V. [42]

Based on a first-principles calculation of the absolute position of the conduction band edge of LLZO, Thompson, *et al.* [33] reported that the LLZO (100)-oriented slab (lowest energy surface) conduction band minimum (CBM) is 0.2 eV higher in energy than the electrochemical potential of bulk Li. (In other words, charge injection to the LLZO CBM is expected to occur at -0.2 V relative to the Li/Li^+ level.) Thus, LLZO should not be susceptible to reduction or chemical decomposition under open-circuit conditions or above (more positive than -0.2 V). From these calculations, it is apparent that the cathodic stability of LLZO under equilibrium conditions is predicted to be close to 0 V vs Li/Li$^+$. However, there remains uncertainty as to what the low voltage stability is under dynamic conditions or when cycling. Under these conditions the potential of the Li electrode can potentially swing to voltages that are negative with respect to Li/Li$^+$, thereby inducing electron transfer from the Li electrode to LLZO.

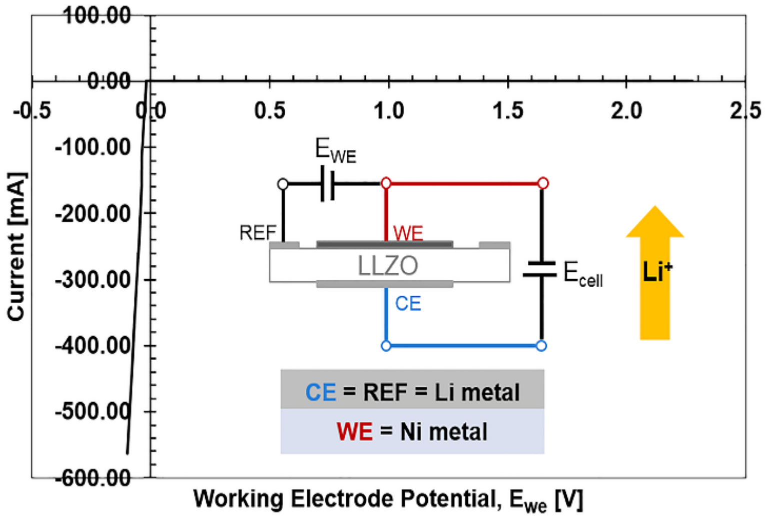

Figure 6.3 *Cyclic voltammetry used to characterize the low potential electrochemical stability of* $Li_{6.25}Al_{0.25}La_3Zr_2O_{12}$ *(LLZO) vs Li/Li*$^+$ *from open circuit voltage (OCV) of 2.3 V down to -0.1 V. Schematic shows the cell configuration used and the ionic current direction*

Typically, cyclic voltammetry (CV) has been used to determine the oxidation and reduction potentials of solid electrolytes using Au/Pt-LLZO|Li cells. However, Li is soluble in gold and platinum within a broad range of compositions,[153] preventing characterization of the low voltage stability. Thus, herein, the low potential stability of LLZO was determined using a Ni WE via CV measurements. Since the solubility of Li in Ni is negligible at room temperature,[153] elimination of alloying enables precise analysis at low potentials. The scan was conducted from open circuit voltage down to – 0.1 V vs. Li/Li$^+$ (Figure 6.3). From 2.28 V down to 0 V vs. Li/Li$^+$, no apparent electrochemical decomposition of LLZO was detected given that no extra current was measured while decreasing the potential. The only additional signal detected was at 1.18V resulting in a current of -0.17 μA (Figure 6.4) We believe that the current generated at this voltage does not correspond to Li_2O ($NiO + 2Li + 2e \rightarrow Li_2O + Ni,\ \Delta G_{Reaction} = -328.6\ kJ\ mol^{-1}$, 1.7 V vs. Li/Li^+) at the interface, or a LLZO decomposition product reported in literature to our knowledge. Considering the magnitude of the current generated is low and that the reaction is not sustained as the potential decreased, we believe that the reaction at 1.18V vs. Li/Li^+ does not correspond to the decomposition of LLZO. Returning back to measuring the low potential stability, the aforementioned results agree with the thermodynamic calculations that predict LLZO is stable near or at 0 V vs. Li/Li^+.

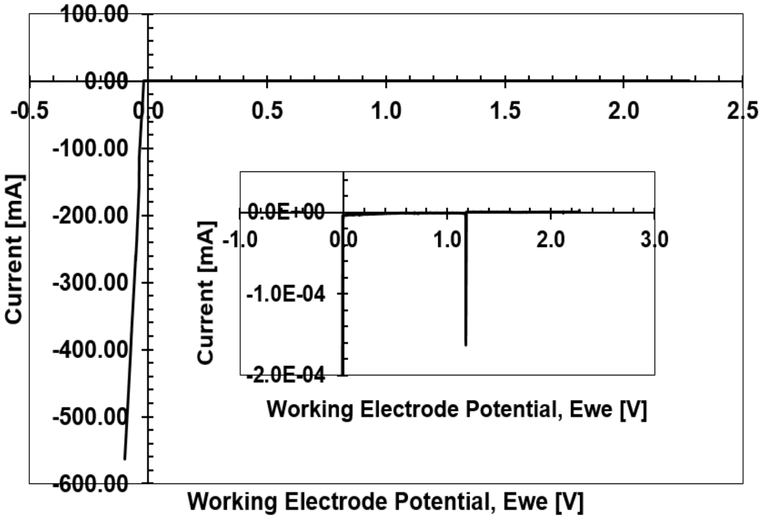

Figure 6.4 *Low potential electrochemical stability of* $Li_{6.25}Al_{0.25}La_3Zr_2O_{12}$ *(LLZO) against metallic Li with Ni as WE and Li as CE. Inset shows a current signal detected with a magnitude of -0.17 μA at 1.18 V, which is not sustained. Thus, suggesting that it does not correspond to an electrochemically decomposed product of LLZO that is electronically conductive that could lead to misinterpretation of the electrochemical stability of LLZO from open circuit voltage (OCV) of 2.28 V down to 0 V vs* Li/Li^+

At and below 0V, however, a sufficiently negative potential is applied to the Ni in this cell configuration, causing deposition of Li^0. Therefore, to study the < 0 V behavior three-electrode cells employing a Li WE were assembled used.

6.2.3 Li - LLZO interface behavior ≤ 0 V vs Li/Li^+

The open circuit voltage of an electrochemical cell is simply related to the difference between the Fermi levels of the electrodes. Consequently, any change of the cell voltage can be a direct measurement of the shift of the Fermi level with respect to the band edges at one electrode, if it is fixed at the other. [154] This leads to the following hypothesis; control of the plating potential at the Li-LLZO interface may shift the electrochemical potential of the Li electrode (related to its Fermi level) closer to the CBM of the garnet LLZO allowing for electron injection to occur. In other words, polarizing the Li WE electrode negatively to a higher energy may surpass the conduction band edge of LLZO resulting in electron transfer from the Li electrode to LLZO. To probe this hypothesis, a custom designed cell was assembled consisting of a ring reference electrode and independently-compressed WE and CE Li electrodes. Stability was characterized sweeping from 0 to -0.1 V vs. Li/ Li^+, in which the potential of the Li working electrode was controlled and the current response of the cell was measured. Several behaviors were observed below 0 V (Figure 6.5). First, at low overpotentials the current response was linear (blue region in Figure 6.6). This region was considered ohmic and stable owing to the linear voltage-current response. Moreover, the slope of the DC curve was determined to be 2065 Ohms and represents the total cell resistance, which is in good agreement (< 7%) with the total cell impedance (1936 Ohms) measured using Electrochemical Impedance Spectroscopy (EIS) (Figure 6.5b). Furthermore, to illustrate our interpretation of ohmic polarization of the Li- LLZO interface, a schematic constructed using crystallographic and electronic structure data, highlights the electron density onto the LLZO (100)-oriented slab in its ground state (Figure 6.6b). The second behavior observed while sweeping down in voltage was a transition between linear/ohmic to non-linear behavior (yellow region in Figure 6.6a). A clear transition is observed at -0.025±0.005 V (cells tested N = 6, see Table 6.1). We believe this potential correlate to a critical potential above which (less negative value) polarization is stable and below which (more negative value) polarization is not stable, or Li nucleation occurs. We believe that when the interface polarization exceeds (more negative value) a critical potential (V_c), not only the Fermi level of the Li WE electrode has shifted to a higher energy, but also the conduction band edge of LLZO at the interface bends closer to the Fermi level of the SSE allowing free electrons to combine with Li-ions leading to Li metal internal precipitation (Figure 6.6c). To analyze the viability of this phenomena more in depth, theoretical calculations on LLZO electronic levels and energies were performed and are explained in more detail on the following subsection. Density of states (DOS) and band edge positions relative to the Li/Li^+ energy level can provide insight to its stability against electron injection. For example, Thompson *et al.* [33] predicted that the La-Li terminated $Li_{6.25}Al_{0.25}La_3Zr_2O_{12}$; (100) and (110) are the two most thermodynamically stable surfaces given their low surface energy. The energy difference between the CBM and the Li/Li^+ level of these surfaces is of 0.2 eV and 0.6 eV, respectively. Thus, these slabs are moderately stable against electron injection at 0 V. These theoretical calculations were obtained under equilibrium conditions. However, in this work, we proposed the energy necessary to shift the Fermi level of the electrode into the conduction band of LLZO is provided by polarization. In the former case, a clear value of polarization (V_c) was determined to be -0.025±0.005 V vs Li/Li^+. This value measured as the V_c for $Li_{6.25}Al_{0.25}La_3Zr_2O_{12}$ has significance in that it is below the Li redox potential, which is a necessity to enable Li as an anode without the need of additional interfacial layers.

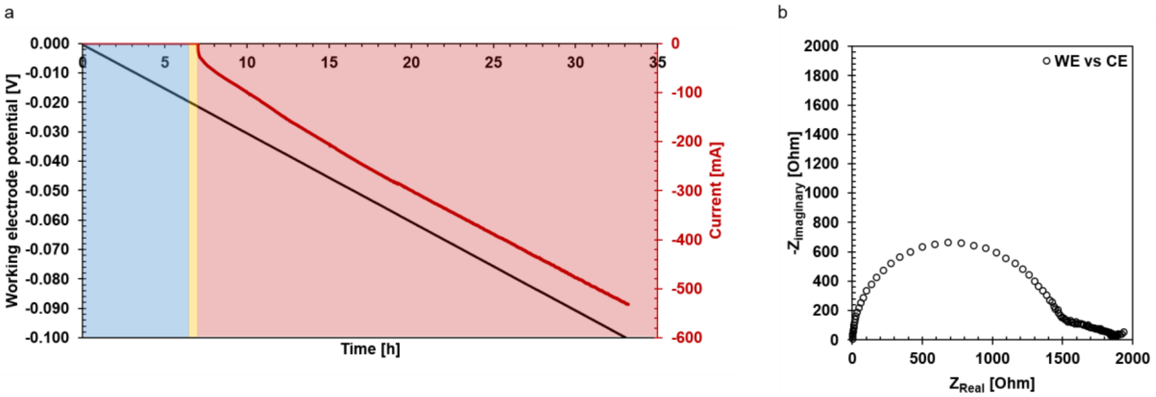

Figure 6.5 *Representative Li – $Li_{6.25}Al_{0.25}La_3Zr_2O_{12}$ (Li-LLZO) interface behavior at an below 0 V vs Li/Li$^+$. (a) Current response to the WE voltage sweep from 0 to -0.1 V vs Li/Li$^+$, composed of three regions (blue, yellow, pink). The potential at which the transition between stable (blue) and unstable (yellow) is observed represents the critical potential (Vc) of LLZO: 0.0025+/-0.0005 V (N =6) vs Li/Li$^+$. The unstable pink region represents Li propagation followed by electrical shorting. (b) Impedance plot of the WE vs CE used to calculate the current expected during the WE voltage sweep and determine the transition between ohmic (stable) to non-ohmic (unstable) behavior.*

Sample No.	AC total impedance [Ohm]	DC resistance [Ohm]	Linear fit for DC data, R^2	Divergence between AC and DC [%]	Critical potential [V]
1	1936.5	2065.3	0.9922	6.7	-0.0206
2	974.8	846.2	0.9992	15.2	-0.0327
3	1053.8	1264.1	0.9994	19.9	-0.0268
4	631.3	753.6	0.9965	19.4	-0.0281
5	691.4	845.3	0.9989	22.3	-0.0288
6	800.7	958.4	0.9970	19.7	-0.0255
Average critical potential [V]					-0.0255 ± 0.0049

Table 6.1 *Determination of the critical potential of the Li – $Li_{6.25}Al_{0.25}La_3Zr_2O_{12}$ (Li-LLZO) interface. Total impedance from AC measurements was compared to the DC resistance obtained from the slope of the cell potential vs current to determine the transition between ohmic (stable) to non-ohmic (unstable) behavior*

Lastly, a significant increase in the current was observed as the potential approached -0.1 V (pink region in Figure 6.6a). This stage is believed to be associated with macroscopic propagation of Li to the extent that electrical shorting eventually occurs (Figure 6.6d). Even though the hypothesis of this work focuses on the electronic aspect of the initiation/nucleation mechanism at the atomic level at which Li penetrates LLZO, EIS superimposed onto the DC voltage sweep support that macroscopic Li propagation occurred on the last stage. (Figure 6.7). The total impedance of the cell decreases dramatically (by 92% from the end of the initiation/nucleation stage, Figure 6.7b), followed by inductive behavior (Figure 6.7c), indicating that electrical shorting occurred and Li propagated from one electrode to the other. Unlike Li metal propagation that occurs during galvanostatic tests where sparsely distributed Li metal filaments cause soft shorting, the volume of Li propagated through LLZO was significantly greater in these potentiostatic tests. This observation could suggest that the Li - LLZO interface stability is voltage-controlled rather than current-controlled. Post-mortem examination of the cells was done using optical and scanning electron microscopy (Figure 6.6d). In addition to the magnitude of the current response measured during the voltage sweep, the macroscopic metallic features observed also support a scenario in which Li metal propagation has occurred. Some of the features started from the Li WE (plating electrode) growing into the potential gradient, parallel to the current flow. These observations are consistent with what Virkar predicted when internal precipitation of cations occurs in cation conductors under electrolytic conditions where an electrically conducting metal propagates perpendicular to the electrolyte/electrode interface.(16) Although some features observed on the optical image appeared to be isolated from the electrode from a 2D view, we believe that they are still connected to the electrode in a different 2D plane. These findings differ with earlier work of Na and Li propagation through inorganic SSEs. First, in Na-SBA and Li-LLZO, it was suggested that internal and isolated metal precipitation was due to electronic conductivity within the bulk electrolyte. [147,150] However, based on these images (Figure 6.6d), there is no clear evidence to suggest that the Li features are isolated and instead appear to be extensions of the original Li metal electrode interface. This is not consistent with other observations where the alkali metal appears to be electrically isolated from the electrode surface. Second, this unstable behavior is not attributed to dielectric breakdown given that wide band gap insulators, such as LLZO, usually require fields on the order of 10^9 V m^{-1},[155] which is far greater than the voltage field used and measured in this study. Finally, Li metal penetration patterns consistent with electrode/electrolyte field discontinuities [17] was not observed in this study. Instead, Li metal penetration occurred uniformly across the Li-LLZO interface.

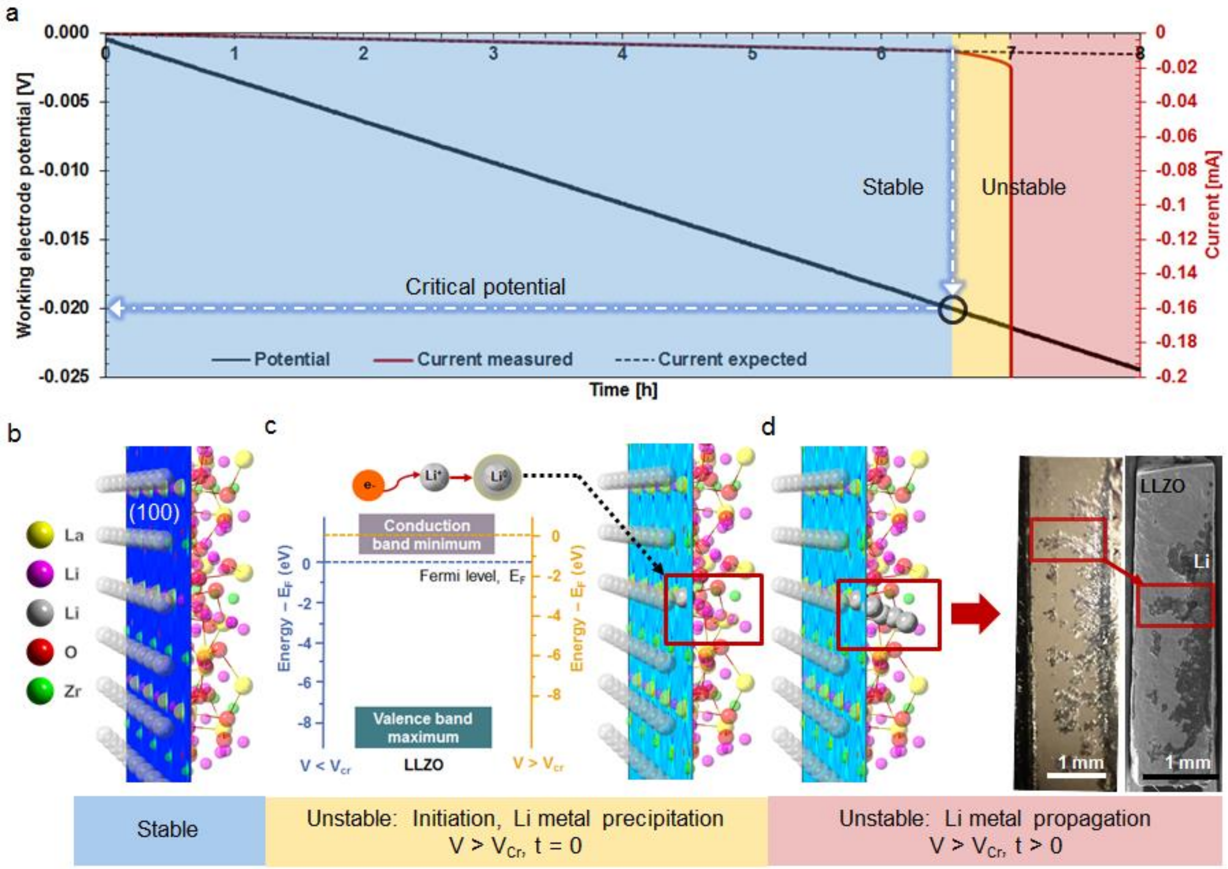

Figure 6.6 *Voltage-controlled quantum and electrochemical analysis of the Li - $Li_{6.25}Al_{0.25}La_3Zr_2O_{12}$ (LLZO) interface behaviour at and below 0V. (a) Current response from 0 to -0.025 V vs Li/Li$^+$, composed of three regions (blue, yellow, pink), for full trace see Figure 6.5a. The critical potential (V_c) is the transition between stable (blue) and unstable (yellow) behavior. The V_c of LLZO was determined to be -0.0025+/-0.0005 V (N =6) vs Li/Li$^+$. The transition from the unstable yellow and pink regions represents the transition between the onset of internal precipitation to meso and macroscopic Li propagation. The current expected (black dotted line) shows the current response expected from EIS total impedance measurements (Figure 6.5) and potential applied. (b) Illustration of ohmic (blue region) polarization of the Li - LLZO interface maps electron density onto the LLZO (100)-oriented slab in its ground state. The highest electron density is observed near the La atoms. (c) Illustration of unstable polarization (yellow region) when V_c is exceeded at t =0. The LLZO Fermi level shifts into the conduction band minimum allowing free electrons to combine with Li-ions leading to Li metal internal precipitation. (d) Illustration of unstable polarization (pink region), or Li propagation followed by electrical shorting. Optical image of the LLZO cross-section shows macroscopic metallic features growing into the potential gradient, parallel to the current flow. Secondary electron image shows the same sample after etching Li with ethanol, where black features in the electrolyte correspond to regions where Li was previously present.*

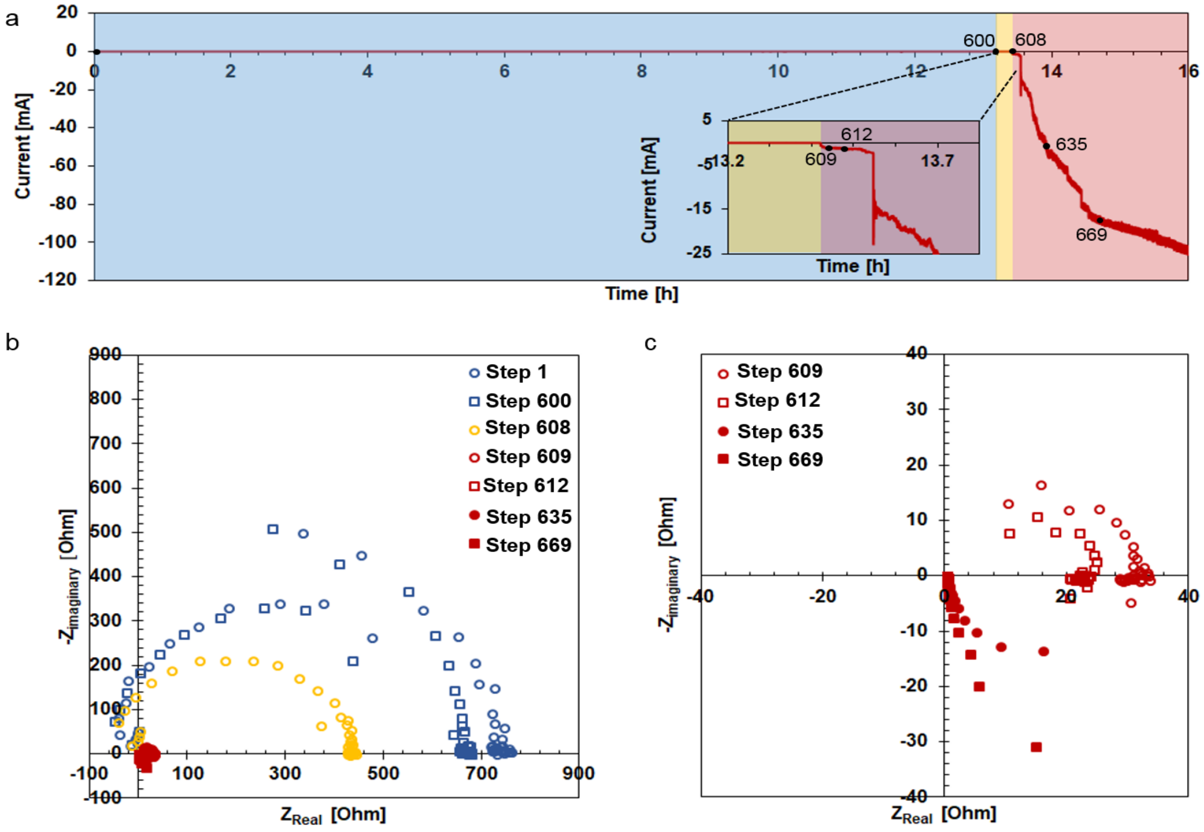

Figure 6.7 *Alternating Current (AC) and (DC) electrochemical behavior of the Li-*$Li_{6.25}Al_{0.25}La_3Zr_2O_{12}$ *(Li-LLZO) interface at and below 0 V vs Li/Li+. (a) Current response of the WE voltage sweep from 0 to -0.1 V vs Li/Li+, composed of three regions (blue, yellow, pink), while superimposing Electrochemical Impedance Spectroscopy (EIS) measurements at the end of each voltage step (voltage step used: -50 uV). The labels indicate the step at which the EIS measurement was conducted. (b) Impedance plots of the three-electrode cell showing a 10% decrease in total impedance suggesting linear/ohmic behavior (stable), shown in blue. The Nyquist plot in yellow shows the AC response of the cell at the end of what is believed to be the initiation stage, is accompanied by a decrease in total impedance of 41% suggest non-ohmic behavior. The Nyquist plots in red that correspond to Li propagation are enlarged on the next figure. (c) Impedance plots of the three-electrode cell showing the evolution of the AC response during what is believed to be Li propagation. First, a dramatic decrease in ionic resistance is observed on voltage steps 609 and 612, interpreted as severe Li propagation, followed by electrical shorting of the cell confirmed by inductive behavior with voltage steps 635 and 669*

6.2.4 Theoretical calculations

First-principles calculations were used to predict the density of states (DOS), band gap, and absolute positions of the band edges of LLZO under reducing conditions. This was accomplished by adding an electron to the LLZO simulation cell, and allowing for ionic relaxation. Such calculations were performed on Li terminated LLZO surfaces and on bulk LLZO. More specifically, (100)-oriented Li-terminated surfaces were employed in these calculations since these are the lowest-energy surfaces identified in our previous study. Hence, the most thermodynamically stable surface slabs in LLZO[33] Recent calculations have suggested that Zr-terminated surface slabs show excellent stability based on their surface energies. However, the (100) Zr- poor (i.e. Li and La rich) are energetically more stable than the (100) Zr-rich surfaces (0.74 vs. 0.83 J·m^{-2}, respectively).[156] Such values suggest that Zr-rich surfaces are somewhat stable. Consequently, herein, the calculations were performed in (100) Li-terminated surface slabs, but the implications of having Zr-terminated slabs will be discussed in the next subsection.

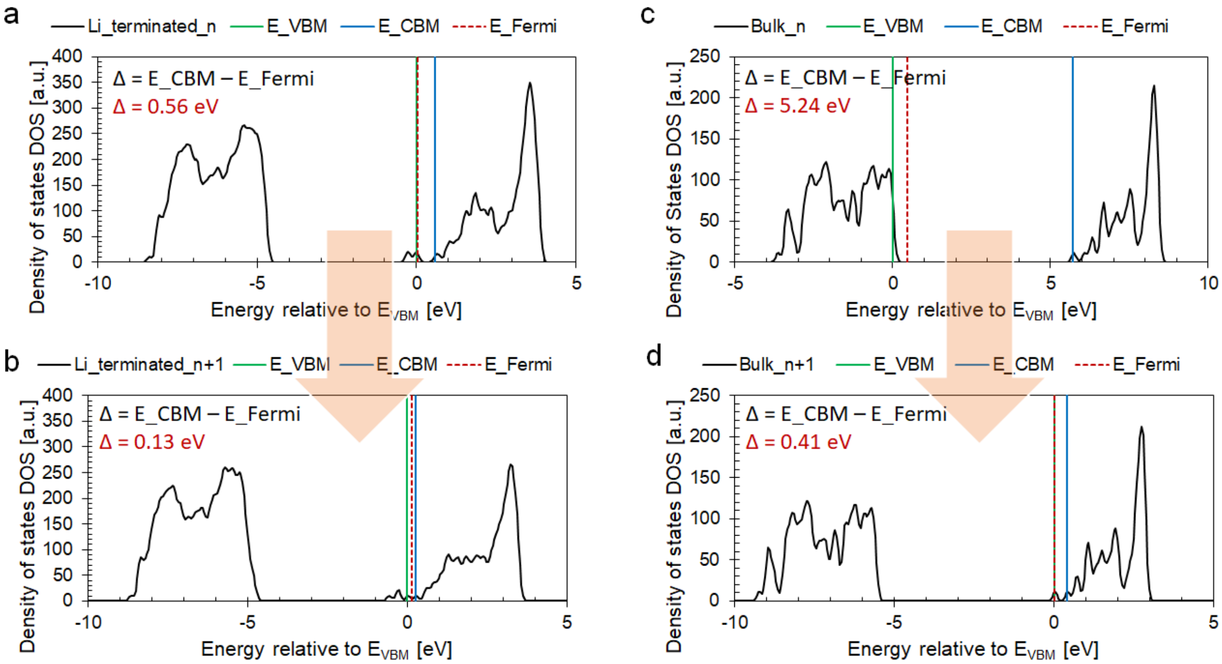

Figure 6.8 *Total density of states (TDOS), band gap and relative positions of the band edges (vs E$_{VBM}$) of (a) Li-terminated surface LLZO slab before and (b) after adding an electron. (c) Bulk LLZO before and (d) after adding an electron. The dotted lines depict the position of the Fermi level and solid lines the position of the conduction band minimum (CBM) and valence band maximum (VBM) at each stage*

The calculations for the (100)-oriented Li-terminated surface slab resulted in a narrow band gap of 0.56 eV compared to a band gap of 5.71 eV for the bulk in its ground state (Figure 6.8a and c, respectively). This difference is a consequence of the additional Li atoms at the surface that result in modification of the electronic states of LLZO. Such slight increase in Li concentration at the interface is in good agreement with EELS measurements at the Li-LLZO interface without any bias.[157] More importantly, the conduction band minimum (CBM) lies slightly above the Fermi level; 0.556 eV in its ground state, which is indicative of moderate stability against electron injection. When an electron is added to the surface, the Fermi level of both the SSE and the electrode shifts to a higher energy whereas the CBM of the SSE shifts to a lower energy level, dramatically reducing the gap between them to 0.130 eV as shown in Figure 6.8b.

The band gap is also reduced by the addition of an electron in the bulk. However, the Fermi level does not shift towards the CBM as it occurs in the surface slab. Differences between the bulk and the surface slab will be further discussed later on the text. The calculations indicate that a shift in the Fermi level and the band edges of a SSE is plausible under dynamic conditions. Moreover, if the energy required for this shift to occur is provided, LLZO is prone to electron injection from the Li negative electrode at the interface, suggesting that the electrochemical stability of an electrolyte might not be an intrinsic property, but can change under dynamic conditions. This result has deeper meaning since most studies on SSEs have considered the electrochemical window to be an intrinsic property, thus, not reflecting the effective stability of the electrolyte against electronic transport during plating.

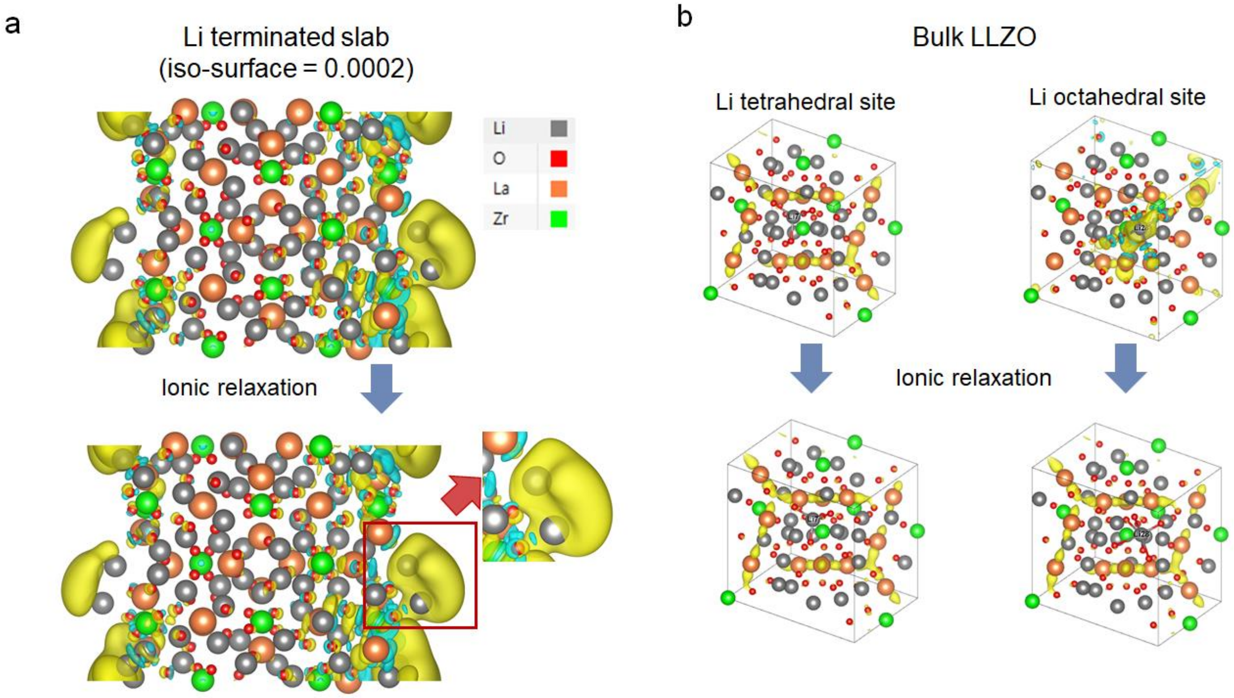

Figure 6.9 *Charge density difference iso-surface plots after adding an electron followed by ionic relaxation of (a) (100)-oriented Li-terminated slabs, showing electron localization near the Li atoms (b) Bulk LLZO, Li tetrahedral sites do not show charge localization upon electron addition, whereas Li octahedral sites do. Charge delocalizes from Li octahedral sites after ionic relaxation redistributing near the lanthanum atoms.*

The value predicted represents the energy necessary for electrons to recombine with Li ions in LLZO and precipitate as Li metal at the interface for one of the most thermodynamically stable surface slabs in LLZO. This additional energy required for the shift to occur could be readily provided potentiostatically during plating at the Li-LLZO interface given its that the small gap between the Fermi level and the CBM in combination with electrons localized at the interface as observed in Figure 6.9a can result in Li metal precipitation. For the bulk calculations, both Li tetrahedral and octahedral sites were studied for charge localization upon addition of electrons. The Li octahedral sites accumulated charge instantaneously, however, upon ionic relaxation the charge redistributed near the lanthanum atoms as shown in Figure 6.9b. This is in excellent agreement with the bulk LLZO partial DOS calculations from our previous work, which indicated that La had the lowest-energy unoccupied states, near the bottom of the conduction band. [33] Thus, we believe that Li^0 precipitation is feasible at the Li-LLZO interface upon polarization, but not the bulk. Consequently, emphasizing that our hypothesis focuses on the electronic aspect of the initiation/nucleation mechanism by which Li penetrates LLZO at the atomic level, and not on the macroscopic propagation of Li. The connection between the atomic level and meso/macroscopic level phenomena need to be further investigated in the future.

The theoretical results showed the feasibility of Li ions precipitating at the Li-LLZO interface as a result of the shift in the Femi level of the electrolyte towards the CBM coupled with charge localization upon polarization. It is noteworthy that the theoretical calculations do not take into account microstructural effects or interfacial interactions that could also shift the band edges. [34,158] Therefore, the value determined could be an overestimation of the effective energy gap needed for the Fermi level to shift into the conduction band minimum. Accounting for these effects would require modeling the full interface at the GW level of theory. Such calculation is a challenge due to the large size of the LLZO unit cell and the expense of these calculations. [159] Further discussion on structural and interfacial effects on the magnitude of the low voltage stability of the Li-LLZO interface can be found next.

6.2.5 Structural and interfacial effects on low potential stability of the Li-LLZO interface

V_c is interpreted as the lowest energy barrier needed to shift the Fermi level of both the electrode and SSE interface near the conduction band edge of the SSE. Thus, any defects or disruption in the bonding environment such as localized non-stoichiometric LLZO compositions at the Li-LLZO interface and/or in the LLZO lattice, could decrease the magnitude of V_c. For instance, it was shown that reactions between Li and LLZO resulted in the presence of an oxygen deficient interphase (ODI) that forms as a consequence of reduction of Zr^{4+}.[160] The reduction of the electrolyte creates oxygen vacancies, where charge could be balanced by electron transfer into the electrolyte according to the reaction: $2Li^0 + O \rightarrow Li_2O + V_O^{\cdot\cdot} + 2e'$, which was also proposed by De Jonghe in SBA for sodium. [161]

Since Zr-terminated surface slabs are somewhat stable, Zr reduction at the interface is plausible. However, based on thermodynamic and kinetic arguments, the low exothermic energy associated with such decomposition (reduction) makes it unfavorable and kinetically inhibited.[34,42] Even though previous theoretical calculations have predicted the phase equilibria may provide passivation to LLZO, [42] Zr_3O is an electronically conductive binary compound.[162] Thus, a mixed ionic-electronic conductive interphase is plausible. It is worth noting that such compound is not thermodynamically stable, and has not been detected experimentally, but its presence at the interface could lead into formation of ion current focusing locations or “hot spots”. Consequently, leading to preferential Li deposition resulting in enhanced mechanical stress at such locations.

Other aspects to consider in the interpretation of V_c are crystallographic orientation and defects such as grain boundaries. [163] As mentioned in Thompson et al.[33], the position of the band gap edges relative to the electrochemical potentials of the electrodes vary with crystallographic orientation. Thus, it is conceivable that the conduction band minimums for some crystallographic orientations are more likely to overlap with the Fermi level than others. Consequently, controlling preferential orientation through grain growth of LLZO, could improve < 0 V stability. Since it has been observed that Li metal can propagate along grain boundaries, the role that grain boundaries play in the manifestation of V_c should be considered (Figure 6.10). For example, since grain size affects the CCD [164], increasing the grain size or reducing the number of grain boundaries per unit area could further improve < 0 V stability. Regardless of the role that crystallographic orientation and microstructural defects may play in the interpretation of V_c, the proposed mechanisms can reconcile some ongoing debate as to why Li metal penetrates not only polycrystalline, but also single crystal LLZO.

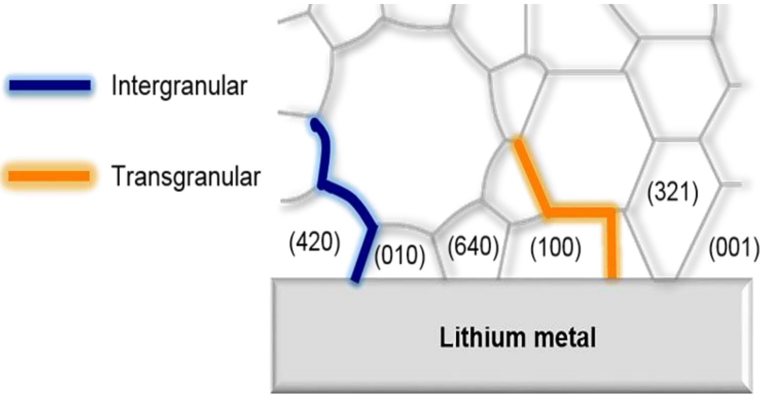

Figure 6.10 *The critical potential could be affected by variations in crystallographic orientation and defects such as grain boundaries. Schematic highlighting multiple Li metal initiation and propagation paths at the Li – $Li_{6.25}Al_{0.25}La_3Zr_2O_{12}$ (Li-LLZO) interface*

6.3 Conclusions

A custom-made three-electrode cell was designed and tested to examine the Li plating potential of the model Li-$Li_{6.25}Al_{0.25}La_3Zr_2O_{12}$ interface. It was demonstrated that LLZO is stable at cathodic potentials below 0 V vs Li/Li$^+$, confirming its compatibility with Li anodes. Based on the Li - LLZO interfacial behavior ≤ 0 V coupled with theoretical calculations, an electronic initiation/nucleation mechanism by which Li penetrates LLZO has been proposed. When the Li-LLZO interface exceeds the critical potential (V_c) of -0.025±0.005 V (cells tested, N = 6) vs Li/Li$^+$, a transition from ohmic to non-ohmic behavior occurs. We believe the origin of this transition is rooted in quantum mechanics. Once the V_c is exceeded, both the electrode and SSE Fermi level shifts near the conduction band minimum (CBM) allowing free electrons to combine with Li-ions leading to Li metal precipitation. Band structure calculations showed the feasibility of Li ions precipitating at the Li-LLZO interface in one of the most thermodynamically stable slab surfaces as a result of the shift in the Femi level of both the electrode and the electrolyte towards the SSE CBM coupled with charge localization near the Li atoms upon polarization. Thus, we believe that Li^0 precipitation is feasible at the Li-LLZO interface upon polarization, but not the bulk. Consequently, emphasizing that our hypothesis focuses on the electronic initiation mechanism by which Li penetrates LLZO at the atomic level and not the macroscopic propagation of Li. This is the first time to our knowledge that a critical potential is measured and used to elucidate the onset of Li metal nucleation in LLZO and may generally apply to other garnet-solid electrolytes. The proposed mechanism can not only provide insight into the fundamental nature of the variables that control the stability of alkali metal-SE interfaces, but also serve as a guideline towards higher charge rates in solid-state battery applications.

6.4 Experimental Details

6.4.1. Preparation of the LLZO solid electrolytes

$Li_{6.25}Al_{0.25}La_3Zr_2O_{12}$ (Al-LLZO) samples were synthesized from starting powders of Li_2CO_3, Al_2O_3, La_2O_3, and ZrO_2 from a solid-state reaction method, calcined at 1000C for 4 h in dry air. Densification of Al-LLZO was achieved by Rapid Induction Hot Pressing (RIHP) green bodies of calcined Al-LLZO at 1225C, 48 MPa for 40 min in an argon atmosphere. Polishing and surface preparation to attain low interfacial resistance was done following a previously reported procedure,[12] adding a final polishing step of 0.1 μm of diamond polishing abrasive before heat treatment at 400°C for 3 h in an Ar atmosphere.

6.4.2 Three-electrode cell fabrication

The three-electrode cell design used in this work (inset illustration in Figure **6.1**a) satisfies the criteria proposed by Winkler *et al.*,[79] which impose constraints on the positioning and size of the reference electrode. These constrains prevent electrochemically driven reactions over the reference electrode. If such reactions would occur, the resulting overpotentials affect measurement with the reference electrode. Calculations were carried out for the samples tested with the reference electrode length and distance between working and reference electrodes. Both of these parameters were normalized by the electrolyte thickness, within 0.50 – 0.56 and 1.4 - 1.6, respectively, thus were within the allowable values that result in a normalized potential difference below 10^{-3}. Moreover, alignment of working and counter electrodes was attained by vapor depositing Li onto laser-cut Kapton masks placed against the solid electrolyte that had the solid electrolyte dimensions. The working and counter electrodes were 0.635 cm in diameter.

Figure 6.2a depicts the EIS measurement of the working versus the counter electrode showing capacitance values that can be assigned to the expected transport phenomena in the order of 10^{-9} F for the bulk, 10^{-6} F for the grain boundary and 10^{-3} F for the Li | LLZO interfaces, respectively. These values follow the trend reported by Irvine *et al.*[83] for an ideal ceramic that uses a brickwork model of grain and grain boundary regions between metal electrodes. The EIS measurement between the working and reference electrodes was measured to assure no electrical short existed between them, as shown with a resistive-capacitive behavior on the figure.

The Ni(WE)/LLZO/Li(CE) with a Li reference electrode was prepared by integrating the Ni working electrode during densification and vapor depositing 10 µm nominal thickness of Li metal as counter and reference electrodes onto laser-cut Kapton with the electrolyte dimensions after heat treatment. The Li three-electrode cells were prepared by vapor depositing (Angstrom

Engineering deposition system) 10 µm nominal thickness of Li as all three electrodes onto laser-cut Kapton masks that were placed onto the solid electrolyte. Preconditioning of the Li-LLZO interfaces was conducted following a previous report. [96]

6.4.3 Materials Characterization

Cubic-LLZO phase purity of hot-pressed samples was confirmed by X-Ray Diffraction (XRD) on a Rigaku Miniflex 600 with a copper anode and graphite monochrometer at 40 kV and 15 mA from 15° to 65° 2θ, step size of 0.02°, speed of 2° min^{-1} as scan parameters (Figure 6.11).

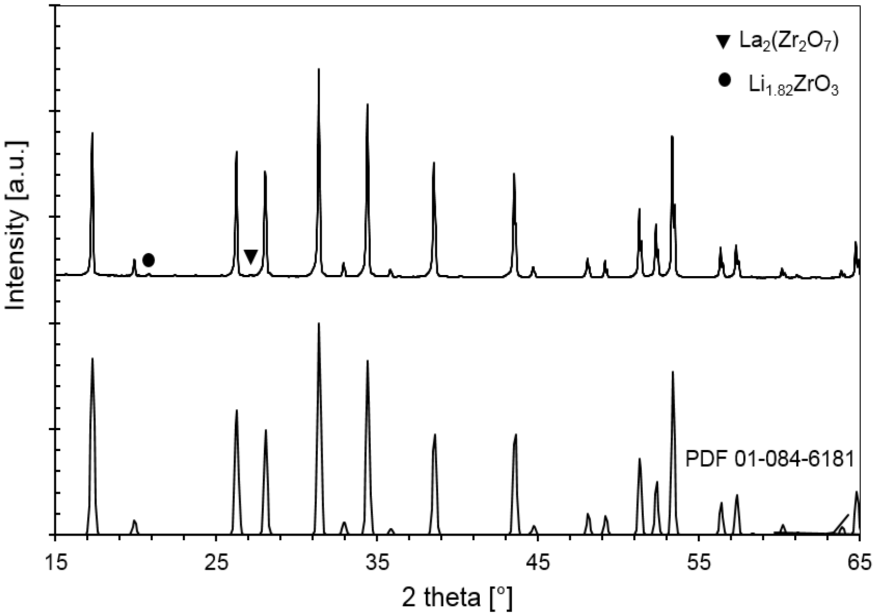

Figure 6.11 *X-Ray diffraction pattern of densified* $Li_{6.25}Al_{0.25}La_3Zr_2O_{12}$ *(LLZO). Representative X-Ray diffraction pattern showing presence of* $La_2(Zr_2O_7)$ *and* $Li_{1.82}ZrO_3$ *as impurities, yielding 0.1 and 1.1 weight percent per Rietveld refinement, respectively*

Optical analysis was performed on a EMZ-13TR microscope inside an Ar filled glovebox with an O_2 trace below 1 ppm. Metallic Li was dissolved with ethanol after optical analysis was completed and morphology was examined using a MIRA3 Tescan SEM at an accelerating voltage of 20 kV and a working distance of 15 mm.

6.4.4. Electron density maps

CrystalMaker 10.2 was used to visualize the crystal structures and electron density maps for the (100)-oriented LLZO surface slab. The Inorganic Crystal Structure Database (ICSD) was used to acquire the crystallographic files for LLZO and Li, no. 261302 and 44367, respectively.

6.4.5. Electrochemical Characterization

The direct current (DC) and electrochemical impedance spectroscopy (EIS) measurements were performed on a potentiostat (BioLogic VMP 300) at room temperature under 4.2 MPa. The EIS measurements were measured in the frequency range from 50 mHz to 7 MHz, 10 mV as perturbation voltage, 3 measurements per frequency. The voltage sweep tests were conducted from OCV for the three-electrode Ni (WE) cell and 0V for the Li three-electrode cells down to -0.1 V vs Li^+/Li. The voltage step used was -50 μV min^{-1}, acquisition settings were adapted for the test to obtain a resolution of 50 μV.

6.4.6 First-principles Calculations

Density functional theory (DFT) calculations were performed using a plane wave basis set and the projector augmented wave method as implemented in the Vienna ab initio simulation package. [138,165] The semi-local generalized gradient approximation (DFT-GGA) of Perdew, Burke, and Ernzerhof (PBE) was used for the exchange-correlation energy.[139] An energy cutoff of 600 eV was used for the plane wave basis, and monkhorst-Pack [166] k-point grids with a 2×2×2 and 2×2×1 density were used for the bulk cells and surface slabs, respectively. The convergence criterion for electronic self-consistency loop was set to 10−5 eV and atomic positions were relaxed until the forces were less than 0.03 $eV \cdot Å^{-1}$. Density of states (DOS) and charge density calculations were performed using the hybrid functional of Heyd, Scuseria, and Ernzerhof (HSE06) [167,168] with a 450 eV energy cutoff. Bulk LLZO (primitive unit cell, 4 formula units) and the lowest surface energy slab (Li-terminated (100) slab, $Li_{67}La_{28}Zr_{20}O_{112}$) cells were adopted from our previous work. [33,159] The details of cell constructions, lowest surface energy slabs, and methods for DOS are provided in previous work. [33,159]

CHAPTER 7 Conclusions and Future Work

Conclusions

In this work, galvanostatic and potentiostatic electrochemical tests were used to gain insight into the role structural and interfacial effects have in Li penetration in SSEs. First, it was shown that processing conditions affect microstructural defects such as pores, particle/grain boundaries in LPS that play a role in causing ionic current focusing effects or “hot spots” leading to Li penetration (Chapter 4). Furthermore, it was determined that the volume fraction of porosity and presence of particle/grain boundaries is negligible (≤ 2 %) by simultaneously applying pressures above 180 MPa heating at the glass transition temperature, 200 °C (Chapter 5). The outcomes of these works show that optimization of the microstructure of the SSE is intimately connected to its maximum tolerable current density that can withstand without short-circuiting (CCD). Second, the integration of a reference electrode in a solid-state cell enabled to control the plating potential at the Li-LLZO interface allowing to detect the onset at which initiation/nucleation and propagation of Li penetration occurs. The experimental results and their corresponding interpretation were validated via first-principles calculations. These results provide new insight into the underlying mechanisms that drive failure in ceramic electrolytes upon charging/plating that could serve as a guideline towards enabling higher rate-capabilities in LMSSBs.

More specifically, in Chapter 4 it was shown that the structural order of LPS SSE can be tuned by strategically controlling the processing conditions, yielding amorphous, glass-ceramic or crystalline materials. Consequently, the differences observed in electrochemical performance were correlated to their respective atomic and micro structures. It was demonstrated that the CCD can be increased by controlling the crystalline structure that precipitates from the mother glass and improving particle-particle adhesion. Nevertheless, further microstructural refinement was highlighted as a future direction to increase the CCD of the solid-state cell. Subsequently (Chapter 5), the thermal behavior of the starting amorphous powder was studied more in depth, and an alternative processing strategy was followed. High molding pressures (> 47 MPa) were used at the glass transition temperature to simultaneously reduce the presence of pores/particle boundaries while suppressing heterogeneous nucleation for crystallization. Moreover, it was determined that molecular rearrangements and favorable Li coordination environments for ionic conduction are attained at ≥ 180 MPa. Consequently, the Young's Modulus approximately doubled and the ionic conductivity increased by a factor of five compared to conventional room temperature molding conditions. Finally, the DC electrochemical stability of the optimized microstructure showed an increase in CCD compared to the conventional cold-pressed sample. However, the role that external variables such as stack pressure and/or temperature play in stable Li stripping were identified as practical challenges that sulfide-based need to overcome for a more straightforward pathway towards improved cycling of Li metal.

Finally, Chapter 6 presents a mechanistic understanding of the coupled interfacial and quantum mechanical effects on the Li-LLZO interface stability at low potentials. Integration of a Li reference electrode in a solid-state cell and precise experimental control allowed measurement, for the first time, of LLZO stability at low potentials. LLZO was determined to be stable at Li cathodic potentials below 0 V vs Li/Li$^+$. An atomistic perspective by which Li penetrates LLZO

SSE at the interface is proposed and validated via first-principles theoretical calculations. Polarization of the Li-LLZO interface shifting the Fermi level of the SSE near the conduction band coupled with charge localization near Li atoms at the interface results in Li metal precipitation. The potential at which the transition between Ohmic and non-ohmic behavior represents the energy needed for this transition to occur, coined as the critical potential of a SSE. Finally, superimposition of Electrochemical Impedance Spectroscopy (EIS) measurements onto the DC measurements allowed analysis of individual transport phenomena *in operando*, thus allowing distinguish between Li initiation and propagation. The findings from this study can help mature LMSSB technology by providing guidelines for the design of bulk SSEs/interfaces to increase the cycling stability, which is one of the major challenges impending their commercialization.

Future Work

Even though improved cycling performance was observed with the dense glassy LPS in terms of CCD, subsequent studies on how to facilitate Li creep at the interface during stripping, pressure-less assisted may be pursued. The behavior of a molten Li electrode could be further examined to elucidate this hypothesis. Furthermore, to predict/assess the possibility of SSE fracture upon plating, hydrostatic pressure estimations are needed from experimental dimensions of surface pores. Gaining insight in this regard can further the understanding of the coupled mechano-electrochemical nature of microscopic Li penetration in ceramic SSEs.

The atomistic model presented in Chapter 6 suggested that structural effects such as grain boundaries and crystallographic orientations can affect the potential at which Li precipitation occurs at the Li-LLZO interface. This creates the opportunity for microstructural engineering to control crystallographic orientation at interfaces. Moreover, it has been demonstrated that the position of the band gaps edges relative to the electrochemical potentials of the electrodes vary with crystallographic orientation. Thus, it is conceivable that the conduction band minimum (CBM) for some crystallographic orientations in LLZO are more likely to overlap with the Fermi level than others. Consequently, one approach to prevent such electrochemical degradation could be performing computational screening, potentially by machine learning, of the most-observed/common crystallographic orientations and calculate the energy difference between their CBM and the Fermi level before and after adding an electron. These data could inform efforts to control preferential orientation through grain growth of LLZO to improve the electrochemical stability of the SSE. Additionally, this approach would reduce the grain boundary area, minimizing the microstructural defects identified to be where Li preferentially penetrates.

Finally, if directional/epitaxial growth of LLZO can be attained for the more stable crystallographic orientations, efforts towards facilitating the deposition stability may be pursued. Surface engineering methods that could make the SSE surface as flat as possible could dramatically reduce the population of critical flaws where fracture could be initiated upon plating/charging. These methods could include mechanical polishing to decrease the defect depth or plasma surface etching that could modify the defect shape (i.e. increase average defect surface area). These surface engineering techniques would translate into lower hydrostatic pressure build up at the Li-LLZO interface upon plating enabling a more stable Li electrodeposition at potentially relevant charging rates (≥ 3 mA·cm^{-2}).

Bibliography

1. Saber, A. Y. & Venayagamoorthy, G. K. Plug-in Vehicles and Renewable Energy Sources for Cost and Emission Reductions. *IEEE Transactions on Industrial Electronics* **58**, 1229–1238 (2011).
2. U.S. Energy Information Administration. *U.S. Energy Related Carbon Dioxide Emissions, 2018*. https://www.eia.gov/environment/emissions/carbon/ (2019).
3. Energy Information Administration. U.S. energy consumption by source and sector, 2018. (2019).
4. International Energy Agency. *Global EV Outlook 2019: Scaling-up the transition to electric mobility*. (OECD, 2019). doi:10.1787/35fb60bd-en.
5. John Warner. *The Handbook of Lithium-Ion Battery Pack Design*. (Elsevier, 2015).
6. United States Advanced Battery Consortium LLC. USABC Goals for Advanced High-Performance Batteries for Electric Vehicle (EV) Applications. (2019).
7. McCloskey, B. D. Attainable Gravimetric and Volumetric Energy Density of Li–S and Li Ion Battery Cells with Solid Separator-Protected Li Metal Anodes. *J. Phys. Chem. Lett.* **6**, 4581–4588 (2015).
8. Albertus, P., Babinec, S., Litzelman, S. & Newman, A. Status and challenges in enabling the lithium metal electrode for high-energy and low-cost rechargeable batteries. *Nat Energy* **3**, 16–21 (2018).
9. Murugan, R., Thangadurai, V. & Weppner, W. Fast Lithium Ion Conduction in Garnet-Type Li7La3Zr2O12. *Angewandte Chemie International Edition* **46**, 7778–7781 (2007).
10. Kamaya, N. *et al.* A lithium superionic conductor. *Nature Mater* **10**, 682–686 (2011).

11. Mizuno, F., Hayashi, A., Tadanaga, K. & Tatsumisago, M. High lithium ion conducting glass-ceramics in the system Li2S–P2S5. *Solid State Ionics* **177**, 2721–2725 (2006).
12. Sharafi, A. *et al.* Surface Chemistry Mechanism of Ultra-Low Interfacial Resistance in the Solid-State Electrolyte Li $_7$ La $_3$ Zr $_2$ O $_{12}$. *Chem. Mater.* **29**, 7961–7968 (2017).
13. Gupta, A. *et al.* Evaluating the Effects of Temperature and Pressure on Li/PEO-LiTFSI Interfacial Stability and Kinetics. *J. Electrochem. Soc.* **165**, A2801–A2806 (2018).
14. Takeda, Y., Yamamoto, O. & Imanishi, N. Lithium Dendrite Formation on a Lithium Metal Anode from Liquid, Polymer and Solid Electrolytes. *Electrochemistry* **84**, 210–218 (2016).
15. Porz, L. *et al.* Mechanism of Lithium Metal Penetration through Inorganic Solid Electrolytes. *Advanced Energy Materials* **7**, 1701003 (2017).
16. Cheng, E. J., Sharafi, A. & Sakamoto, J. Intergranular Li metal propagation through polycrystalline Li6.25Al0.25La3Zr2O12 ceramic electrolyte. *Electrochimica Acta* **223**, 85–91 (2017).
17. Swamy, T. *et al.* Lithium Metal Penetration Induced by Electrodeposition through Solid Electrolytes: Example in Single-Crystal Li $_6$ La $_3$ ZrTaO $_{12}$ Garnet. *J. Electrochem. Soc.* **165**, A3648–A3655 (2018).
18. Shen, F., Dixit, M. B., Xiao, X. & Hatzell, K. B. Effect of Pore Connectivity on Li Dendrite Propagation within LLZO Electrolytes Observed with Synchrotron X-ray Tomography. *ACS Energy Lett.* **3**, 1056–1061 (2018).
19. Garcia-Mendez, R., Mizuno, F., Zhang, R., Arthur, T. S. & Sakamoto, J. Effect of Processing Conditions of 75Li2S-25P2S5 Solid Electrolyte on its DC Electrochemical Behavior. *Electrochimica Acta* **237**, 144–151 (2017).

20. Garcia-Mendez, R., Smith, J. G., Neuefeind, J. C., Siegel, D. J. & Sakamoto, J. Correlating Macro and Atomic Structure with Elastic Properties and Ionic Transport of Glassy Li2S-P2S5 (LPS) Solid Electrolyte for Solid-State Li Metal Batteries. *Adv. Energy Mater* doi:10.1002/aenm.202000335.
21. Goodenough, J. B. & Park, K.-S. The Li-Ion Rechargeable Battery: A Perspective. *J. Am. Chem. Soc.* **135**, 1167–1176 (2013).
22. Besenhard, J. O. *Handbook of Battery Materials*. (John Wiley & Sons, 2008).
23. Nazri, G.-A. & Pistoia, G. *Lithium Batteries: Science and Technology*. (Springer, 2009).
24. Wu, Y. *Lithium-Ion Batteries: Fundamentals and Applications*. (CRC Press, 2015).
25. Huggins, R. A. *Advanced Batteries: Materials Science Aspects*. (Springer).
26. Bruce, P. G. *Chemistry of Solid State Materials: Solid State Electrochemistry*. (Cambridge University Press, 1997).
27. Lewis, J. A., Tippens, J., Cortes, F. J. Q. & McDowell, M. T. Chemo-Mechanical Challenges in Solid-State Batteries. *Trends in Chemistry* (2019) doi:10.1016/j.trechm.2019.06.013.
28. Tarascon, J. M. & Armand, M. Issues and Challenges facing rechargeable lithium batteries. *Nature* **414**, (2001).
29. Quartarone, E. & Mustarelli, P. Electrolytes for solid-state lithium rechargeable batteries: recent advances and perspectives. *Chem. Soc. Rev.* **40**, 2525 (2011).
30. Kato, Y. *et al.* High-power all-solid-state batteries using sulfide superionic conductors. *Nat Energy* **1**, 16030 (2016).
31. Manthiram, A., Yu, X. & Wang, S. Lithium battery chemistries enabled by solid-state electrolytes. *Nat Rev Mater* **2**, 16103 (2017).
32. Munshi, M. Z. A. *Handbook of Solid State Batteries & Capacitors*. (World Scientific, 1995).

33. Thompson, T. *et al.* Electrochemical Window of the Li-Ion Solid Electrolyte $Li_7La_3Zr_2O_{12}$. *ACS Energy Lett.* **2**, 462–468 (2017).

34. Zhu, Y., He, X. & Mo, Y. First principles study on electrochemical and chemical stability of solid electrolyte–electrode interfaces in all-solid-state Li-ion batteries. *J. Mater. Chem. A* **4**, 3253–3266 (2016).

35. Seino, Y., Ota, T., Takada, K., Hayashi, A. & Tatsumisago, M. A sulphide lithium super ion conductor is superior to liquid ion conductors for use in rechargeable batteries. *Energy Environ. Sci.* **7**, 627–631 (2014).

36. Thangadurai, V., Narayanan, S. & Pinzaru, D. Garnet-type solid-state fast Li ion conductors for Li batteries: critical review. *Chem. Soc. Rev.* **43**, 4714 (2014).

37. Aono, H. Ionic conductivity and sinterability of lithium titanium phosphate system. *Solid State Ionics* **40–41**, 38–42 (1990).

38. Tsai, C.-L. *et al.* $Li_7La_3Zr_2O_{12}$ Interface Modification for Li Dendrite Prevention. *ACS Appl. Mater. Interfaces* **8**, 10617–10626 (2016).

39. Zhang, Y. *et al.* Garnet-Based Solid-State Lithium Fluoride Conversion Batteries Benefiting from Eutectic Interlayer of Superior Wettability. *ACS Energy Lett.* 1167–1176 (2020) doi:10.1021/acsenergylett.0c00383.

40. Wakayama, H., Yonekura, H. & Kawai, Y. Three-Dimensional Bicontinuous Nanocomposite from a Self-Assembled Block Copolymer for a High-Capacity All-Solid-State Lithium Battery Cathode. *Chem. Mater.* **28**, 4453–4459 (2016).

41. Richards, W. D., Miara, L. J., Wang, Y., Kim, J. C. & Ceder, G. Interface Stability in Solid-State Batteries. *Chem. Mater.* **28**, 266–273 (2016).

42. Zhu, Y., He, X. & Mo, Y. Origin of Outstanding Stability in the Lithium Solid Electrolyte Materials: Insights from Thermodynamic Analyses Based on First-Principles Calculations. *ACS Appl. Mater. Interfaces* **7**, 23685–23693 (2015).

43. García-Martín, S., Amador, U., Morata-Orrantia, A., Rodríguez-Carvajal, J. & Alario-Franco, M. Á. Structure, Microstructure, Composition and Properties of Lanthanum Lithium Titanates and some Substituted Analogues. *Zeitschrift für anorganische und allgemeine Chemie* **635**, 2363–2373 (2009).

44. Ma, C. *et al.* Atomic-scale origin of the large grain-boundary resistance in perovskite Li-ion-conducting solid electrolytes. *Energy Environ. Sci.* **7**, 1638 (2014).

45. Xu, X., Wen, Z., Wu, J. & Yang, X. Preparation and electrical properties of NASICON-type structured Li1.4Al0.4Ti1.6(PO4)3 glass-ceramics by the citric acid-assisted sol–gel method. *Solid State Ionics* **178**, 29–34 (2007).

46. Li, S. *et al.* Reaction mechanism studies towards effective fabrication of lithium-rich anti-perovskites Li3OX (X= Cl, Br). *Solid State Ionics* **284**, 14–19 (2016).

47. Ohta, S. *et al.* Co-sinterable lithium garnet-type oxide electrolyte with cathode for all-solid-state lithium ion battery. *Journal of Power Sources* **265**, 40–44 (2014).

48. Inaguma, Y. & Nakashima, M. A rechargeable lithium–air battery using a lithium ion-conducting lanthanum lithium titanate ceramics as an electrolyte separator. *Journal of Power Sources* **228**, 250–255 (2013).

49. Kasper, H. M. Series of rare earth garnets Ln3+3M2Li+3O12 (M=Te, W). *Inorg. Chem.* **8**, 1000–1002 (1969).

50. Geiger, C., A. *et al.* Crystal Chemistry and Stability of ‘Li7La3Zr2O12’ Garnet: A Fast Lithium-Ion Conductor. *Inorg. Chem.* **50**, 1089–1097 (2011).

51. Allen, J. L., Wolfenstine, J., Rangasamy, E. & Sakamoto, J. Effect of substitution (Ta, Al, Ga) on the conductivity of Li7La3Zr2O12. *Journal of Power Sources* **206**, 315–319 (2012).
52. Ohta, S., Kobayashi, T. & Asaoka, T. High lithium ionic conductivity in the garnet-type oxide Li7−X La3(Zr2−X, NbX)O12 (X=0–2). *Journal of Power Sources* **196**, 3342–3345 (2011).
53. Bernstein, N., Johannes, M. D. & Hoang, K. Origin of the Structural Phase Transition in Li 7 La 3 Zr 2 O 12. *Phys. Rev. Lett.* **109**, 205702 (2012).
54. Rangasamy, E., Wolfenstine, J. & Sakamoto, J. The role of Al and Li concentration on the formation of cubic garnet solid electrolyte of nominal composition Li7La3Zr2O12. *Solid State Ionics* **206**, 28–32 (2012).
55. Wolfenstine, J., Ratchford, J., Rangasamy, E., Sakamoto, J. & Allen, J. L. Synthesis and high Li-ion conductivity of Ga-stabilized cubic Li7La3Zr2O12. *Materials Chemistry and Physics* **134**, 571–575 (2012).
56. Logéat, A. *et al.* From order to disorder: The structure of lithium-conducting garnets Li7−xLa3TaxZr2−xO12 (x=0–2). *Solid State Ionics* **206**, 33–38 (2012).
57. Wang, M., Wolfenstine, J. B. & Sakamoto, J. Temperature dependent flux balance of the Li/Li7La3Zr2O12 interface. *Electrochimica Acta* **296**, 842–847 (2019).
58. Hayashi, A. & Tatsumisago, M. Electrolytes: Glass. in *Secondary Batteries - Lithium Rechargeable Systems* 138–144 (Elsevier, 2009).
59. Kanno, R. & Murayama, M. Lithium Ionic Conductor Thio-LISICON: The Li2 S - GeS2 - P 2 S 5 System. *J. Electrochem. Soc.* **148**, A742–A746 (2001).
60. Xiao, Y. *et al.* Understanding interface stability in solid-state batteries. *Nat Rev Mater* (2019) doi:10.1038/s41578-019-0157-5.

61. Hayashi, A., Hama, S., Minami, T. & Tatsumisago, M. Formation of superionic crystals from mechanically milled Li2S–P2S5 glasses. *Electrochemistry Communications* **5**, 111–114 (2003).

62. Mizuno, F., Hayashi, A., Tadanaga, K. & Tatsumisago, M. New, Highly Ion-Conductive Crystals Precipitated from Li2S–P2S5 Glasses. *Advanced Materials* **17**, 918–921 (2005).

63. Mizuno, F., Hayashi, A., Tadanaga, K. & Tatsumisago, M. New Lithium-Ion Conducting Crystal Obtained by Crystallization of the Li2S–P2S5 Glasses. 4.

64. Muramatsu, H., Hayashi, A., Ohtomo, T., Hama, S. & Tatsumisago, M. Structural change of Li2S–P2S5 sulfide solid electrolytes in the atmosphere. *Solid State Ionics* **182**, 116–119 (2011).

65. Tachez, M., Malugani, J.-P., Mercier, R. & Robert, G. Ionic conductivity of and phase transition in lithium thiophosphate Li3PSS4. **14**, 181–185 (1984).

66. German, R. M. *Powder metallurgy science*. (Metal Powder Industries Federation, 1994).

67. Ring, T. A. *Fundamentals of Ceramic Powder Processing and Synthesis*. (Academic Press, 1996).

68. Barsoum, M. W. *Fundamentals of ceramics*. (IOP, 2003).

69. Kingery, W. D. *Introduction to ceramics*. (John Wiley & Sons, 1960).

70. Radomir, I., Geamăn, V. & Stoicănescu, M. Densification Mechanisms Made During Creep Techniques Applied to the Hot Isostatic Pressing. *Procedia - Social and Behavioral Sciences* **62**, 779–782 (2012).

71. Sharafi, A. *et al.* Impact of air exposure and surface chemistry on Li–$Li_7La_3Zr_2O_{12}$ interfacial resistance. *J. Mater. Chem. A* **5**, 13475–13487 (2017).

72. Bard, A. & Faulkner, L. R. *Electrochemical Methods: Fundamentals and Applications*. (John Wiley & Sons).

73. Belt, J. R., Bernardi, D. M. & Utgikar, V. Development and Use of a Lithium-Metal Reference Electrode in Aging Studies of Lithium-Ion Batteries. *J. Electrochem. Soc.* **161**, A1116–A1126 (2014).

74. Nagasubramanian, G. & Doughty, D. H. 18650 Li-ion cells with reference electrode and in situ characterization of electrodes. *Journal of Power Sources* **150**, 182–186 (2005).

75. Wu, M.-S., Chiang, P.-C. & Lin, J.-C. Electrochemical Investigations on Advanced Lithium-Ion Batteries by Three-Electrode Measurements. *Journal of the Electrochemical Society* **152**, A47–A52 (2005).

76. Pham, A. Q. & Glass, R. S. Three Electrode Measurements on Solid Electrolytes. in *MRS Online Proceedings Library* (Cambridge University Press, 2011). doi:10.1557/PROC-411-237.

77. Tenhaeff, W. E. *et al.* Resolving the Grain Boundary and Lattice Impedance of Hot-Pressed Li7La3Zr2O12 Garnet Electrolytes. *ChemElectroChem* **1**, 375–378 (2014).

78. Han, G. *et al.* Correlating the effect of dopant type (Al, Ga, Ta) on the mechanical and electrical properties of hot-pressed Li-garnet electrolyte. *Journal of the European Ceramic Society* **40**, 1999–2006 (2020).

79. Winkler, J. Geometric Requirements of Solid Electrolyte Cells with a Reference Electrode. *J. Electrochem. Soc.* **145**, 1184 (1998).

80. Cullity, B. D. *Elements of x-ray diffraction*. (Addison-Wesley Pub. Co, 1978).

81. Barsoukov, E. & Macdonald, J. R. *Impedance Spectroscopy*. (John Wiley & Sons, Ltd, 2018). doi:10.1002/9781119381860.

82. Huggins, R. A. Simple method to determine electronic and ionic components of the conductivity in mixed conductors a review. *Ionics* **8**, 300–313 (2002).

83. Irvine, J. T. S., Sinclair, D. C. & West, A. R. Electroceramics: Characterization by Impedance Spectroscopy. *Advanced Materials* **2**, 132–138 (1990).

84. Schwarz, R. B. Introduction to the viewpoint set on: Mechanical alloying. *Scripta Materialia* **34**, 1–4 (1996).

85. Koch, C. C. Amorphization of single composition powders by mechanical milling. *Scripta Materialia* **34**, 21–27 (1996).

86. Kerman, K., Luntz, A., Viswanathan, V., Chiang, Y.-M. & Chen, Z. Review—Practical Challenges Hindering the Development of Solid State Li Ion Batteries. *J. Electrochem. Soc.* **164**, A1731–A1744 (2017).

87. Wakihara, M. & Yamamoto, O. *Lithium Ion Batteries: Fundamentals and Performance*. (John Wiley & Sons, 2008).

88. Sakuda, A., Hayashi, A. & Tatsumisago, M. Sulfide Solid Electrolyte with Favorable Mechanical Property for All-Solid-State Lithium Battery. *Sci Rep* **3**, 2261 (2013).

89. Sakuda, A., Hayashi, A., Takigawa, Y., Higashi, K. & Tatsumisago, M. Evaluation of elastic modulus of Li2S^|^ndash;P2S5 glassy solid electrolyte by ultrasonic sound velocity measurement and compression test. *J. Ceram. Soc. Japan* **121**, 946–949 (2013).

90. Eom, M., Kim, J., Noh, S. & Shin, D. Crystallization kinetics of Li 2 S–P 2 S 5 solid electrolyte and its effect on electrochemical performance. *Journal of Power Sources* **284**, 44–48 (2015).

91. Murayama, M., Sonoyama, N., Yamada, A. & Kanno, R. Material design of new lithium ionic conductor, thio-LISICON, in the Li2S–P2S5 system. *Solid State Ionics* **170**, 173–180 (2004).

92. Ranasinghe, K. S., Ray, C. S. & Day, D. E. A generalized method for determining the crystal nucleation and growth rates in glasses by differential thermal analysis. 9.

93. Somiya, S. *Handbook of Advanced Ceramics*. (Academic Press, 2013).

94. Berbano, S. Low temperature processing of sulfide and oxide lithium solid electrolytes to bridge ionically resistive boundaries. (The Pennsylvania State University, 2016).

95. Ishiguro, K. *et al.* Stability of Nb-Doped Cubic Li $_7$ La $_3$ Zr $_2$ O $_{12}$ with Lithium Metal. *J. Electrochem. Soc.* **160**, A1690–A1693 (2013).

96. Sharafi, A., Meyer, H. M., Nanda, J., Wolfenstine, J. & Sakamoto, J. Characterizing the Li–Li7La3Zr2O12 interface stability and kinetics as a function of temperature and current density. *Journal of Power Sources* **302**, 135–139 (2016).

97. Nagao, M. *et al.* In situ SEM study of a lithium deposition and dissolution mechanism in a bulk-type solid-state cell with a Li2S–P2S5 solid electrolyte. *Phys. Chem. Chem. Phys.* **15**, 18600 (2013).

98. Meyer, B. Elemental Sulfur. *Chem. Rev.* **76**, 367–388 (1976).

99. El Jaroudi, O., Picquenard, E., Demortier, A., Lelieur, J.-P. & Corset, J. Structure and Vibrational Spectra of the S22 - and S32- Anions. Influence of the Cations on Bond Length and Angle. in *Polysulfide Anions* vol. 38 2394–2401 (Inorganic Chemistry, 1999).

100. El Jaroudi, O., Picquenard, E., Demortier, A., Lelieur, J.-P. & Corset, J. Structure and Vibrational Spectra of the S42- and S52- Anions. Influence of the Cations on Bond Lenght,

Valence and Torsion Angle. in *Polysulfide Anions* vol. 39 2593–2603 (Inorganic Chemistry, 2000).

101. Lin, Z., Liu, Z., Fu, W., Dudney, N. J. & Liang, C. Phosphorous Pentasulfide as a Novel Additive for High-Performance Lithium-Sulfur Batteries. *Advanced Functional Materials* **23**, 1064–1069 (2013).
102. Ong, S. P. *et al.* Phase stability, electrochemical stability and ionic conductivity of the $Li_{10±1}MP_2X_{12}$ (M = Ge, Si, Sn, Al or P, and X = O, S or Se) family of superionic conductors. *Energy Environ. Sci.* **6**, 148–156 (2013).
103. Wenzel, S. *et al.* Interphase formation and degradation of charge transfer kinetics between a lithium metal anode and highly crystalline Li7P3S11 solid electrolyte. *Solid State Ionics* **286**, 24–33 (2016).
104. Hayashi, A., Hama, S., Morimoto, H., Tatsumisago, M. & Minami, T. Preparation of Li2S–P2S5 Amorphous Solid Electrolytes by Mechanical Milling. *Journal of the American Ceramic Society* **84**, 477–79 (2001).
105. Chu, S. & Majumdar, A. Opportunities and challenges for a sustainable energy future. *Nature* **488**, 294–303 (2012).
106. Liu, Z. *et al.* Anomalous High Ionic Conductivity of Nanoporous β-Li_3PS_4. *J. Am. Chem. Soc.* **135**, 975–978 (2013).
107. Sakuda, A., Hayashi, A., Hama, S. & Tatsumisago, M. Preparation of Highly Lithium-Ion Conductive 80Li2S·20P2S5 Thin-Film Electrolytes Using Pulsed Laser Deposition. *Journal of the American Ceramic Society* **93**, 765–768 (2010).

108. Minami, K., Mizuno, F., Hayashi, A. & Tatsumisago, M. Lithium ion conductivity of the Li2S–P2S5glass-based electrolytesprepared by the melt quenching method. **178**, 837–847 (2007).

109. Ito, S., Nakakita, M., Aihara, Y., Uehara, T. & Machida, N. A synthesis of crystalline Li7P3S11 solid electrolyte from 1,2-dimethoxyethane solvent. *Journal of Power Sources* **271**, 342–345 (2014).

110. Hayashi, A., Minami, K., Ujiie, S. & Tatsumisago, M. Preparation and ionic conductivity of Li7P3S11−z glass-ceramic electrolytes. *Journal of Non-Crystalline Solids* **356**, 2670–2673 (2010).

111. S. Gutzow, I. *The vitreous state: thermodynamics, structure, rheology, and crystallization*. (Springer, 2013).

112. Hayashi, A. *et al.* Characterization of Li2S–P2S5glass-ceramics as a solid electrolytefor lithium secondary batteries. **175**, 683–686 (2004).

113. Sidek, H. A. A., Chow, S. P., Talib, Z. A. & Halim, S. A. Formation and elastic properties of lithium chlorophosphate glasses. *Solid State Science and Technology* **11**, 7 (2003).

114. Kato, A. *et al.* Mechanical properties of sulfide glasses in all-solid-state batteries. *J. Ceram. Soc. Japan* **126**, 719–727 (2018).

115. *CRC handbook of chemistry and physics: a ready-reference book of chemical and physical data*. (CRC Press, 2013).

116. Rice, R. W. *Porosity of ceramics*. (M. Dekker, 1998).

117. Rouxel, T. Elastic Properties and Short-to Medium-Range Order in Glasses. *Journal of the American Ceramic Society* **90**, 3019–3039 (2007).

118. Ohara, K. *et al.* Structural and electronic features of binary Li2S-P2S5 glasses. *Sci Rep* **6**, 21302 (2016).

119. Serbena, F. C. & Zanotto, E. D. Internal residual stresses in glass-ceramics: A review. *Journal of Non-Crystalline Solids* **358**, 975–984 (2012).

120. Messer, R. & Noack, F. Nuclear magnetic relaxation by self-diffusion in solid lithium:T 1-frequency dependence. *Appl. Phys.* **6**, 79–88 (1975).

121. Hao, F., Verma, A. & Mukherjee, P. P. Mesoscale Complexations in Lithium Electrodeposition. *ACS Appl. Mater. Interfaces* **10**, 26320–26327 (2018).

122. Masias, A., Felten, N., Garcia-Mendez, R., Wolfenstine, J. & Sakamoto, J. Elastic, plastic, and creep mechanical properties of lithium metal. *J Mater Sci* **54**, 2585–2600 (2019).

123. Homma, K. *et al.* Crystal structure and phase transitions of the lithium ionic conductor Li3PS4. *Solid State Ionics* **182**, 53–58 (2011).

124. Orera, A., García-Alvarado, F. & Irvine, J. T. S. Effect of Ti-substitution on the Electrical Properties of $MnNb_2O_{6-\delta}$. *Chem. Mater.* **19**, 2310–2315 (2007).

125. Smith, J. G. First Principles Study of Magnesium/Oxygen Batteries and Glassy Solid Electrolytes. (University of Michigan, 2018).

126. Dietrich, C. *et al.* Lithium ion conductivity in Li_2S–P_2S_5 glasses – building units and local structure evolution during the crystallization of superionic conductors Li_3PS_4, $Li_7P_3S_{11}$ and $Li_4P_2S_7$. *J. Mater. Chem. A* **5**, 18111–18119 (2017).

127. Ichihashi, K. *et al.* Optimizing Lithium Ion Conduction through Crown Ether-Based Cylindrical Channels in $[Ni(dmit)_2]^-$ Salts. *Chem. Mater.* **30**, 7130–7137 (2018).

128. Mott, N. F. & Gurney, R. W. *Electronic processes in ionic crystals*. (Oxford, Clarendon Press, 1953).

129. Chen, H., Hong, T. & Jing, Y. The mechanical, vibrational and thermodynamic properties of glass-ceramic lithium thiophosphates Li4P2S6. *Journal of Alloys and Compounds* **819**, 152950 (2020).

130. Kasemchainan, J. *et al.* Critical stripping current leads to dendrite formation on plating in lithium anode solid electrolyte cells. *Nat. Mater.* **18**, 1105–1111 (2019).

131. Wang, M. J., Choudhury, R. & Sakamoto, J. Characterizing the Li-Solid-Electrolyte Interface Dynamics as a Function of Stack Pressure and Current Density. *Joule* **3**, 2165–2178 (2019).

132. Krauskopf, T., Hartmann, H., Zeier, W. G. & Janek, J. Toward a Fundamental Understanding of the Lithium Metal Anode in Solid-State Batteries—An Electrochemo-Mechanical Study on the Garnet-Type Solid Electrolyte $Li_{6.25}Al_{0.25}La_3Zr_2O_{12}$. *ACS Appl. Mater. Interfaces* **11**, 14463–14477 (2019).

133. Spencer Jolly, D. *et al.* Sodium/Na β″ Alumina Interface: Effect of Pressure on Voids. *ACS Appl. Mater. Interfaces* **12**, 678–685 (2020).

134. Yu, S. *et al.* Elastic Properties of the Solid Electrolyte $Li_7La_3Zr_2O_{12}$ (LLZO). *Chem. Mater.* **28**, 197–206 (2016).

135. *Standard Test Method for Assignment of the Glass Transition Temperature by Thermomechanical Analysis*. (2016).

136. ASTM International. Standard Practice for Measuring Ultrasonic Velocity in Materials.

137. Akkermans, R. L. C., Spenley, N. A. & Robertson, S. H. Monte Carlo methods in Materials Studio. *Molecular Simulation* **39**, 1153–1164 (2013).

138. Kresse, G. & Furthmüller, J. Efficient iterative schemes for *ab initio* total-energy calculations using a plane-wave basis set. *Phys. Rev. B* **54**, 11169–11186 (1996).

139. Perdew, J. P., Burke, K. & Ernzerhof, M. Generalized Gradient Approximation Made Simple. *Phys. Rev. Lett.* **77**, 3865–3868 (1996).

140. Blöchl, P. E. Projector augmented-wave method. *Phys. Rev. B* **50**, 17953–17979 (1994).

141. Hirota, K., Ye, Z.-G., Wakimoto, S., Gehring, P. M. & Shirane, G. Neutron diffuse scattering from polar nanoregions in the relaxor Pb (Mg 1 / 3 Nb 2 / 3) O 3. *Phys. Rev. B* **65**, 104105 (2002).

142. Ryouichi Yokoyama & Harada, Jimpei. X-ray Stress Analysis in Textured Polycrystalline Materials. *Journal of the Crystallographic Society of Japan* **52**, 113–119.

143. Willems, T. F., Rycroft, C. H., Kazi, M., Meza, J. C. & Haranczyk, M. Algorithms and tools for high-throughput geometry-based analysis of crystalline porous materials. *Microporous and Mesoporous Materials* **149**, 134–141 (2012).

144. Shannon, R. D. Revised effective ionic radii and systematic studies of interatomic distances in halides and chalcogenides. *Acta Cryst A* **32**, 751–767 (1976).

145. Yu, S. & Siegel, D. J. Grain Boundary Softening: A Potential Mechanism for Lithium Metal Penetration through Stiff Solid Electrolytes. *ACS Appl. Mater. Interfaces* **10**, 38151–38158 (2018).

146. Kazyak, E. *et al.* Li Penetration in Ceramic Solid Electrolytes: Operando Microscopy Analysis of Morphology, Propagation, and Reversibility. *Matter* S2590238520300709 (2020) doi:10.1016/j.matt.2020.02.008.

147. Han, F. *et al.* High electronic conductivity as the origin of lithium dendrite formation within solid electrolytes. *Nat Energy* **4**, 187–196 (2019).

148. Virkar, A. Failure of ion-conducting materials by internal precipitation under electrolytic conditions. in *Engineered Ceramics: Current status and future prospects* 536 (John Wiley & Sons).

149. Armstrong, R. D., Dickinson, T. & Turner, J. The breakdown of β-alumina ceramic electrolyte. **19**, (1974).

150. De Jonghe, L. C., Feldman, L. & Beuchele, A. Slow degradation and electron conduction in sodium/beta-aluminas. *Journal of Materials Science* **16**, 780–786 (1981).

151. De Jonghe, L. C., Feldman, L. & Buechele, A. Failure modes of Na-Beta Alumina. *Solid State Ionics* **5**, 267–270 (1981).

152. Garcia-Mendez, R., Smith, J. G., Neuefeind, J. C., Siegel, D. J. & Sakamoto, J. Correlating Macro and Atomic Structure with Elastic Properties and Ionic Transport of Glassy $Li_2S-P_2S_5$ (LPS) Solid Electrolyte for Solid-State Li Metal Batteries. *Adv. Energy Mater.* 2000335 (2020) doi:10.1002/aenm.202000335.

153. Yan, K. *et al.* Selective deposition and stable encapsulation of lithium through heterogeneous seeded growth. *Nat Energy* **1**, 16010 (2016).

154. Kleitz, M. & Dupuy, J. *Electrode Processes in Solid State Ionics*. (D. Reidel Publishing Company, 1975).

155. Buechele, A. C. Degradation Modes in Sodium Beta-Alumina. (Cornell University, University of California Berkeley, 1982).

156. Gao, B., Jalem, R. & Tateyama, Y. Surface-Dependent Stability of the Interface between Garnet $Li_7La_3Zr_2O_{12}$ and the Li Metal in the All-Solid-State Battery from First-Principles Calculations. *ACS Appl. Mater. Interfaces* acsami.9b23019 (2020) doi:10.1021/acsami.9b23019.

157. Ma, C. *et al.* Interfacial Stability of Li Metal–Solid Electrolyte Elucidated via in Situ Electron Microscopy. *Nano Lett.* **16**, 7030–7036 (2016).

158. Kumar, N. & Siegel, D. J. Interface-Induced Renormalization of Electrolyte Energy Levels in Magnesium Batteries. *J. Phys. Chem. Lett.* **7**, 874–881 (2016).

159. Yu, Seungho. Atomic Scale Simulations of the Solid Electrolyte Li7La3Zr2O12. (University of Michigan, 2018).

160. Zhu, Y. *et al.* Dopant-Dependent Stability of Garnet Solid Electrolyte Interfaces with Lithium Metal. *Advanced Energy Materials* **9**, 1803440 (2019).

161. De Jonghe, L. C. Transport Number Gradients and Solid Electrolyte Degradation. *J. Electrochem. Soc.* **129**, 752 (1982).

162. Jain, A. *et al. The Materials Project: A materials genome approach to accelerating materials innovation*. (APL Materials, 2013).

163. Kahn, A. Fermi level, work function and vacuum level. *Mater. Horiz.* **3**, 7–10 (2016).

164. Sharafi, A., Haslam, C. G., Kerns, R. D., Wolfenstine, J. & Sakamoto, J. Controlling and correlating the effect of grain size with the mechanical and electrochemical properties of $Li_7La_3Zr_2O_{12}$ solid-state electrolyte. *J. Mater. Chem. A* **5**, 21491–21504 (2017).

165. Kresse, G. & Joubert, D. From ultrasoft pseudopotentials to the projector augmented-wave method. *Phys. Rev. B* **59**, 1758–1775 (1999).

166. Monkhorst, H. J. & Pack, J. D. Special points for Brillouin-zone integrations. *Phys. Rev. B* **13**, 5188–5192 (1976).

167. Heyd, J., Scuseria, G. E. & Ernzerhof, M. Hybrid functionals based on a screened Coulomb potential. *The Journal of Chemical Physics* **118**, 8207–8215 (2003).

168. Krukau, A. V., Vydrov, O. A., Izmaylov, A. F. & Scuseria, G. E. Influence of the exchange screening parameter on the performance of screened hybrid functionals. *The Journal of Chemical Physics* **125**, 224106 (2006).